Electronic Theses and Dissertations, 2020-

2023

# Compact and High Optical Efficiency Near-Eye Displays with Liquid Crystal Flat Optics

Junyu Zou
*University of Central Florida*

Part of the Optics Commons

Find similar works at: https://stars.library.ucf.edu/etd2020

University of Central Florida Libraries http://library.ucf.edu

University of Central Florida

STARS

Showcase of Text, Archives, Research & Scholarship

COMPACT AND HIGH OPTICAL EFFICIENCY NEAR-EYE DISPLAYS
WITH LIQUID CRYSTAL FLAT OPTICS

by

JUNYU ZOU
B.S. Beijing Institute of Technology, 2016
M.S. University of Michigan---Ann Arbor, 2018

A dissertation submitted in partial fulfillment of the requirements
for the degree of Doctor of Philosophy
in the College of Optics and Photonics
at the University of Central Florida
Orlando, Florida

Spring Term
2023

Major Professor: Shin-Tson Wu

# ABSTRACT

Since the concepts of augmented reality (AR) and virtual reality (VR) were introduced, they have attracted people's attention worldwide, both in the industry and research areas. As the most promising hardware architecture that can bring AR/VR into daily life, near eye displays (NEDs) have been studied and investigated heavily over the past half-century, especially the concept of "Metaverse" introduced by some top companies in recent years. However, the form factor and optical efficiency are two major bottlenecks for the current NEDs before they can become the major platform.

Liquid crystal (LC) flat optics have several advantages, including compact, high diffraction efficiency, easy to pattern, highly transparent and low cost. Therefore, they are idea candidates for NEDs applications.

In this dissertation, we focus on the novel LC flat optics applications in the NEDs, aiming to reduce the system form factor and enhance the system optical efficiency. The first half surrounds VR applications and systems, which adopt transmission-type LC flat optics. The second half covers AR system design and demonstration, which takes the advantages of reflection-type LC flat optics. In VR part, we demonstrate an approach to double the optical efficiency of VR systems based on a directional backlight and a diffractive deflection film (DDF), which is a specially designed LC flat optics. Our approach works well in both Fresnel and "pancake" VR systems. We also have the simulation model, which exhibits results highly consistent with the experiment. What's more, a new ultra-compact VR system is also proposed and demonstrated in this dissertation. In this ultra-compact VR system, an LC deflector is inserted into the imaging optics and it can achieve a process

called polarization interpolation. This process helps reduce the distance from the display panel to the imaging optics by 50% in theory.

In AR part, we design and demonstrate a gaze matched Maxwellian-view AR system pupil steering system. This system applies the LC flat optics as the optical combiner. In the demo, this system achieves many good properties, including compact form factor, high optical efficiency, gaze matching, extended eyebox, aberration free, good ambient light transmittance and relatively large field of view. The proposed applications and systems with LC flat optics are attractive for next-generation NEDs.

To my family.

# ACKNOWLEDGMENTS

# TABLE of CONTENTS

# LIST OF FIGURES

# LIST OF TABLES

# CHAPTER 1: INTRODUCTION

Creating a magic world and a fabulous viewing experience has always been the dream of human being, even if they do not exist in our real world currently. Then, the challenge that researchers trying to figure out is how to produce such a fascinating scene and present it in front of the user's eye. This is also the reason that virtual reality (VR) and augmented reality (AR) are generated. The concept of VR was first demonstrated in the 1960s when Morton Heilig introduced an immersive, multi-sensory machine called "Sensorama" (Fig. 1-1(a)) [1] and the first AR system was demonstrated by Ivan. E. Sutherland in 1968 (Fig. 1-1(b)) [2]. They have attracted people's attention around the whole world, both in industry and academia. As the most promising hardware architecture can bring AR/VR into our daily lives, near eye displays (NEDs) have been studied and investigated heavily in the past half century, especially the concept of "Metaverse" introduced by some top companies in recent years. After several decades of intensive development, the NED industry has finally flourished and several products such as Oculus Quest 2 (Fig. 1-1(c)), Magic Leap 1 and HoloLens 2 (Fig. 1-1(d)), etc., have brought fabulous experience to consumers in entertainment [3], education [4], healthcare [5], and engineering design [6], just to name a few.

At present, several performance parameters of NEDs have reached an acceptable level, including field of view (FOV) [7], resolution [8], color gamut [9], contrast ratio [10], dynamic range [11], and response time [11,12] (not considering multiplane displays). These parameters still have large room for improvement, and we have a long way to go before they can match the performance of traditional direct-view flat panel displays. However, the imperfection of these parameters mainly influences the image quality, which is already acceptable in many user cases and will not be the bottleneck for NEDs, if they are adopted by people in their daily life like cell

phones. We think the form factor [13,14] and optical efficiency [14,15] are two major bottlenecks for the current NEDs before they can become the major platform. With continuous progress, it is very likely that next generation NEDs would make a big difference in these two factors.
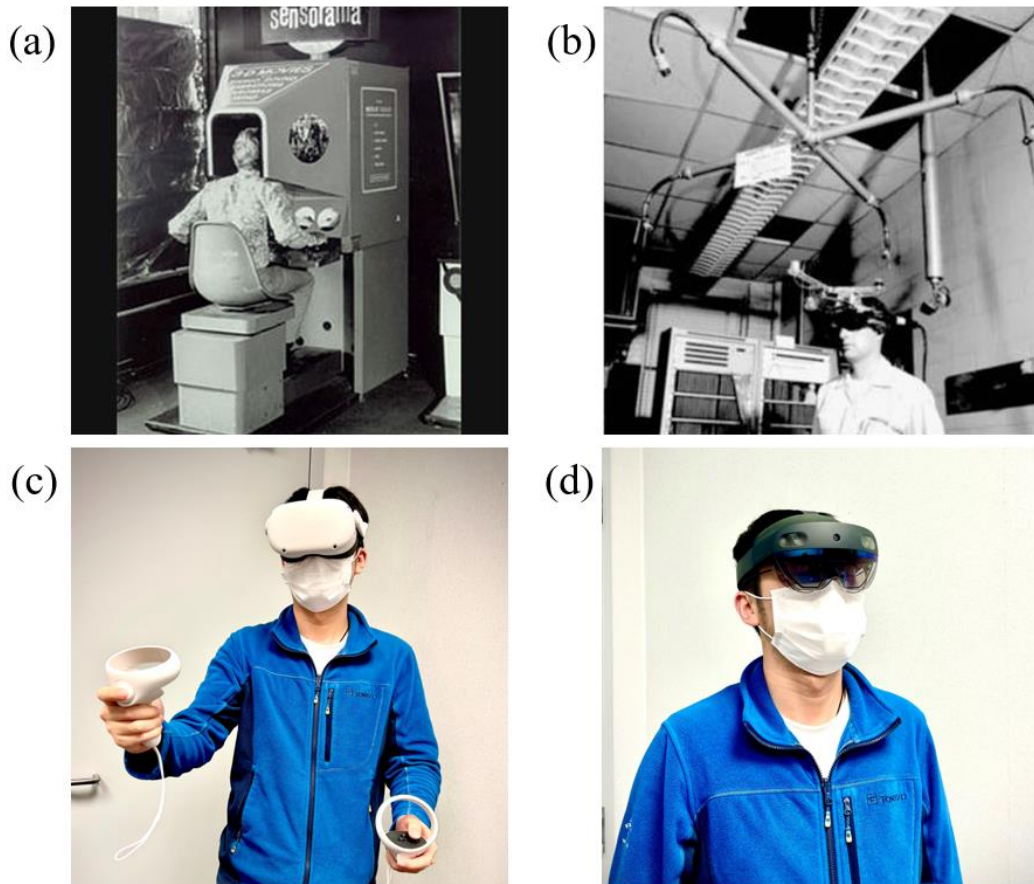


**Figure 1-1: Schematics of early (a) VR, (b) AR and recent (c) VR, (d) AR near eye displays.**

According to Fig. 1-1, we can see that the early-stage NEDs are so bulky and heavy. The way people using them is to mount themselves to the NEDs rather than mount the NEDs on their heads, let alone wearing the NEDs walking around. After half a century, the NEDs have achieved significant progress. Their sizes have been reduced a lot and are qualified to be called head-mounted displays. However, there is still a gap between current NEDs and glasses-like NEDs.

What a user is willing to wear for a whole day is not a big screen, but a pair of lightweight glasses. Therefore, making the NEDs as compact as a pair of glasses is an important milestone.

On the other hand, if we want to make the NEDs as the platform for our daily communication and entertainment, which just like the smartphones today, power consumption is another critical issue [16]. In comparison with cell phones, which can continuously work for more than ten hours, most of the NEDs can only support 2 to 3 hours of active use at present. Moreover, most of the power in current NEDs is consumed by the light engine, because only a small portion of the light emitted from the light engine enters the user's eye pupil [17,18]. As Fig. 1-2 indicates, for a VR system shown in Fig. 1-2(a), usually the light engine has a broad angular distribution [19,20], but only a small part of the light enters the eyebox, which is located in a narrow angular bandwidth. Thus, most of the light emitted from the display panel is wasted. For an AR system, optical efficiency is even more critical, because the digital image must be bright enough to compete with the ambient light [21,22]. The waveguide is the most popular AR structure in the current stage [23,24]. The basic structure is shown in Fig. 1-2(b). The major advantage of the waveguide structure is large eyebox due to the exit pupil expansion (EPE). However, this benefit greatly sacrifices the system's optical efficiency, since only a small portion of the output beams can enter the user's eye pupil. In short, the optical efficiency of the current NED is very low. Therefore, it is urgent to enhance the optical efficiency of current NEDs while keeping a compact form factor.
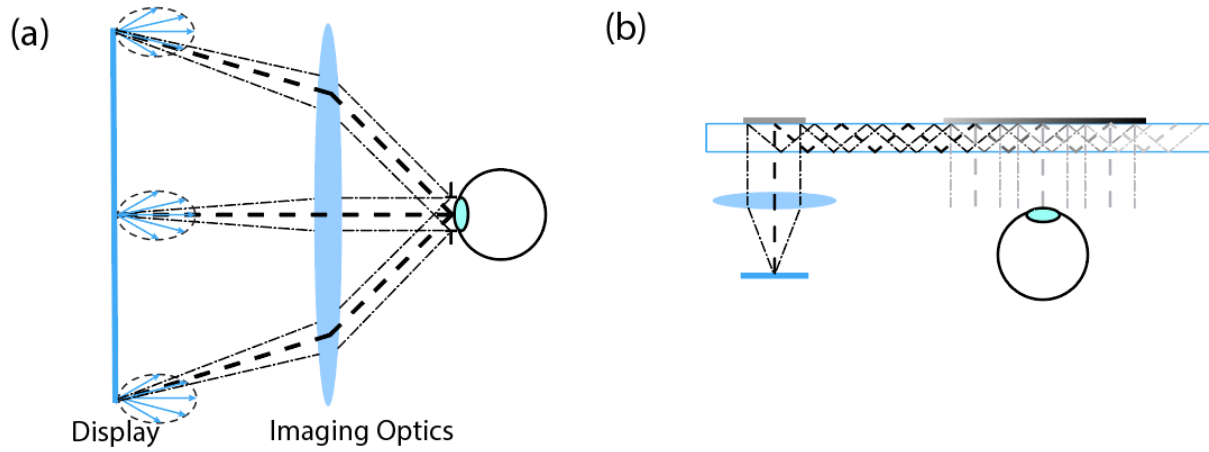
**Figure 1-2: Schematics of (a) VR and (b) waveguide AR optical structure.**

Liquid crystal (LC) flat optics exhibit several advantages, including compact size, high diffraction efficiency, easy to pattern, highly transparent and low cost [24–30]. Therefore, they are attractive candidates for NED applications [7,31–36].

The most important property of LC flat optics described in this dissertation is the geometric phase [37]. Traditional LC optical elements rely on the LC birefringence to produce phase retardation [38]. However, the birefringence of LC materials is usually limited to ~0.25 when the good photo and chemical stabilities are considered [12,39,40]. Therefore, traditional LC optics exhibit some disadvantages when compared with refractive optics, such as lens [41]. Of course, traditional LC optics can also be designed and patterned as diffractive optical elements, such as LC phase grating and Fresnel phase zone plate [42–45]. But these optical elements suffer from limited diffraction efficiency and fringing field effect due to the phase jump between different zones [46]. On the other hand, the LC flat optics based on geometric phase show several advantages. First, the phase retardation of such an optical element depends on the azimuthal angle

4

of the LC directors. This brings significant advantages since it can be easily patterned as arbitrary phase [26], which does not increase the fabrication complexity and device form factor. Besides, the diffraction efficiency of the LC flat optics is higher than that of conventional diffractive LC elements, which can approach 100% [25]. More details about this point will be explained in later chapters. What's more, the LC flat optics have a very thin profile, which is advantageous in terms of high transparency and low cost regarding material usage [47]. These attractive properties of LC flat optics provide a good match to the requirements of NEDs. Therefore, widespread applications of LC flat optics in NEDs are foreseeable.

# CHAPTER 2: LC GEOMETRIC PHASE OPTIC ELEMENTS

Some content of this chapter was previously published in [20].

## 2.1 Transmission Type LC Flat Optical Elements

The transmission type liquid crystal flat optics in this dissertation is also referred to as Pancharatnam-Berry (PB) phase optical element. Such a PB phase is a kind of geometric phase.
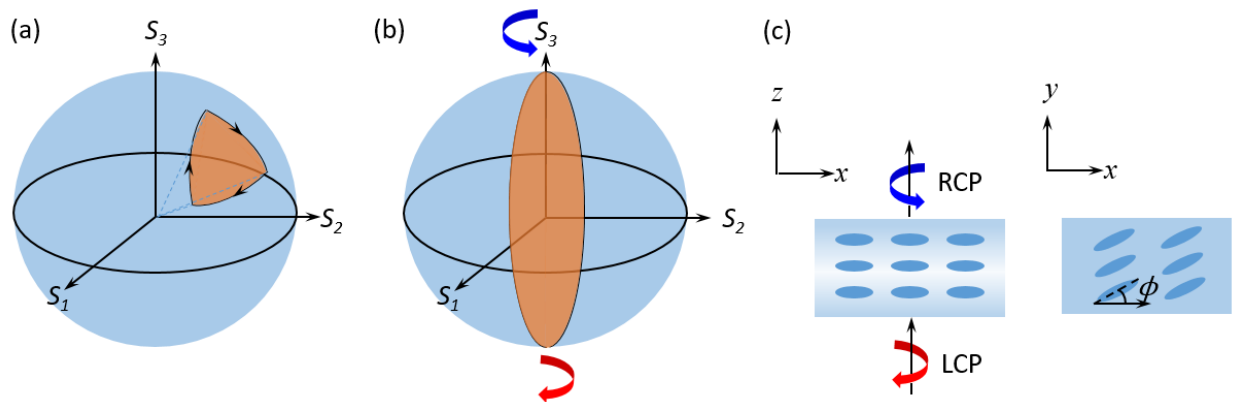


**Figure 2-1: (a) Geometric phase on Poincaré sphere, (b) Pancharatnam-Berry Phase of transmission-type LC flat optical elements on Poincaré sphere, (c) local LC directions of transmission-type LC flat optical elements.**

First of all, the naming of PB phase is based on the pioneering works of two scientists: Shivaramakrishnan Pancharatnam and Michael Victor Berry. In Pancharatnam's work, he found that when a polarized beam traverses a closed loop on the Poincaré sphere [48], the final state differs from the initial state by a phase factor which is proportional to the closed area [49,50], as shown in Fig. 2-1(a). In Berry's work, he found that when an atom goes through an adiabatic evolution [51] and returns to its initial state, during this process, it causes nothing change in the surrounding environment, except for an extra phase on itself, and this phase is defined as Berry

phase [52]. We can see that both studies present similar concept, but S. Pacharatnam presents a specific case and M. V. Berry summarizes it in more general form.

If we look at the Poincaré sphere, since it is a perfect sphere, and has good symmetry, then the two polar points on the sphere can be considered as the same. When a circularly polarized light transverses to the opposite state, we can also consider it to return to the initial state (Fig. 2-1(b)). In practice, if a circularly polarized light passes through an LC half-wave plate and the LC director has an azimuthal angle phi, which is indicated in Fig. 2-1(c), then the corresponding Jones matrix can be expressed as follows:

$$J'_{\pm} = R(-\phi)W(\pi)R(\phi)J_{\pm} \tag{2-1}$$

$$J'_{\pm} = \frac{1}{\sqrt{2}}\begin{bmatrix} \cos 2\phi & \sin 2\phi \\ \sin 2\phi & -\cos 2\phi \end{bmatrix}\begin{bmatrix} 1 \\ \pm i \end{bmatrix} = \frac{1}{\sqrt{2}}\begin{bmatrix} 1 \\ \mp i \end{bmatrix}e^{\pm 2i\phi} \tag{2-2}$$

According to Eq. (2-2), we find that when it is converted into the opposite circular polarization, there is an extra phase, and this phase happens to satisfy the definition of PB phase. Therefore, this type of optical device is called PB optical elements (PBOEs). By patterning the orientation of the LC directors to a desired profile, then the device will perform as designed functionality like grating or lens. In this sense, we can regard PBOEs as the patterned half-wave plate.
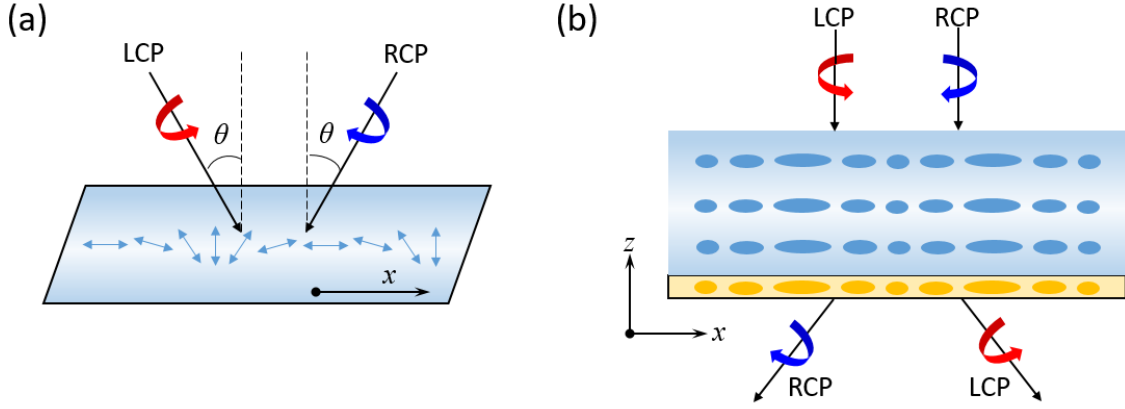
**Figure 2-2: (a) Schematic of molecular direction with two-beam interference, (b) working principal of PB optical elements.**

For the linear phase change, which can be achieved by two-beam interference exposure, as

Fig. 2-2(a) depicts. It can be easily derived for the grating pattern as:

$$\begin{bmatrix} 1 \\ i \end{bmatrix} e^{-ik_0 x \sin\theta} + \begin{bmatrix} 1 \\ -i \end{bmatrix} e^{ik_0 x \sin\theta} = 2 \begin{bmatrix} \cos(k_0 x \sin\theta) \\ \sin(k_0 x \sin\theta) \end{bmatrix} \tag{2-3}$$

According to Eq. (2-3), the grating pattern is sinusoidal linear polarization. And the transform

matric of the PB grating can be expressed as [53]:

$$T(x) = \cos(\frac{\pi \Delta nd}{\lambda})I + i\sin(\frac{\pi \Delta nd}{\lambda}) \begin{bmatrix} \sin(2k_0 x \sin\theta) & \cos(2k_0 x \sin\theta) \\ \cos(2k_0 x \sin\theta) & -\sin(2k_0 x \sin\theta) \end{bmatrix} \ldots\ldots(2\text{-}4)$$

Based on that, the far field diffraction pattern can be calculated:

$$D_m = \frac{1}{\Lambda} \int_0^\Lambda T(x) E_{in} \exp(-i2\pi m x / \Lambda) dx \ldots\ldots\ldots\ldots\ldots(2\text{-}5)$$

$$\eta_0 = \cos^2(\frac{\pi \Delta nd}{\lambda}), \eta_{\pm 1} = \frac{1 \mp S_3'}{2} \sin^2(\frac{\pi \Delta nd}{\lambda}) \ldots\ldots\ldots\ldots\ldots(2\text{-}6)$$

where $S_3' = S_3/S_0$ is the normalized Stokes parameter of the incident light. From the calculation

results, only the $0^{th}$ and $\pm 1$ orders have the nonzero solution, because there are linear phase changes

in the Fourier transform. When the phase satisfies the half-wave condition, the zero order will be eliminated, and the Jones matrix will be the same as we derived before. The working condition of PB optical elements is illustrated in Fig. 2-2(b). This is why PB gratings can achieve nearly 100% diffraction efficiency, which are attractive for practical applications [34,47].
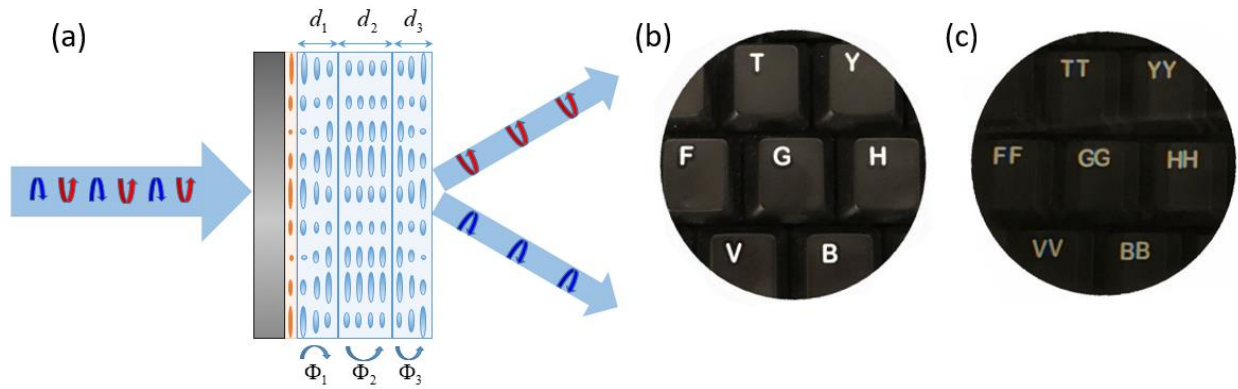


**Figure 2-3: (a) Schematic of three-layer multi-twist PB grating, (b) and imaging performance test (b) input and (c) output.**

It is worth mentioning that the key to obtain a high diffraction efficiency is to satisfy the half-wave condition. However, for the single layer non-twist PB optical elements, usually only one wavelength can perfectly meet the half-wave condition in theory [25]. In a practical imaging system, full color operation is always desired. Therefore, dual-twist [25] and multi-twist [27,47] structures have been demonstrated for the broadband performance. In Fig. 2-3(a), there is a designed three-layer PB grating, which can achieve high efficiency in the visible spectral range and large incident angle. We apply the rigorous coupled-wave analysis (RCWA) method [54,55] to simulate this three-layer grating structure. In the optimization process, the grating period was fixed. The thickness of each layer was set from 0μm to 3μm, and the twist angle of each layer was set from $-2\pi$ to $2\pi$. Four optimization algorithms, genetic algorithm, particle swarm optimization, adaptive simulated annealing, and differential evolution, are interchangeably used to optimize the

grating parameters. The optimization results show the thickness of the three LC layers is $d_1$=0.9μm, $d_2$=1.32μm and $d_3$=0.88μm, and the corresponding twist angle is $\phi_1$= −69.4°, $\phi_2$=3.7° and $\phi_3$=64°, respectively. We took a picture for testing with this PB grating placed between the camera and a keyboard. The input image is shown in Fig. 2-3(b) and the output image after the PB grating is shown in Fig. 2-3(c). The input is unpolarized ambient light, consisting of 50% RCP and 50% LCP. In Fig. 2-3(c), two ± 1$^{st}$ order diffracted lights are clearly observed. The zero-order leakage is negligible, which means the PB grating has a nearly 100% diffraction efficiency in the visible spectral region. The PB grating splits the input beam into two outgoing beams, so that the brightness of each order is reduced to ~50%. The simulated and measured spectrums are presented in the Fig. 2-4. What's more, the three-layer PB grating also has the advantage for large incident angle as indicated in Fig. 2-4(c). Of course, thanks to the geometric phase, PB optical elements can be patterned to an arbitrary phase profile but follows the same intrinsic working principle.
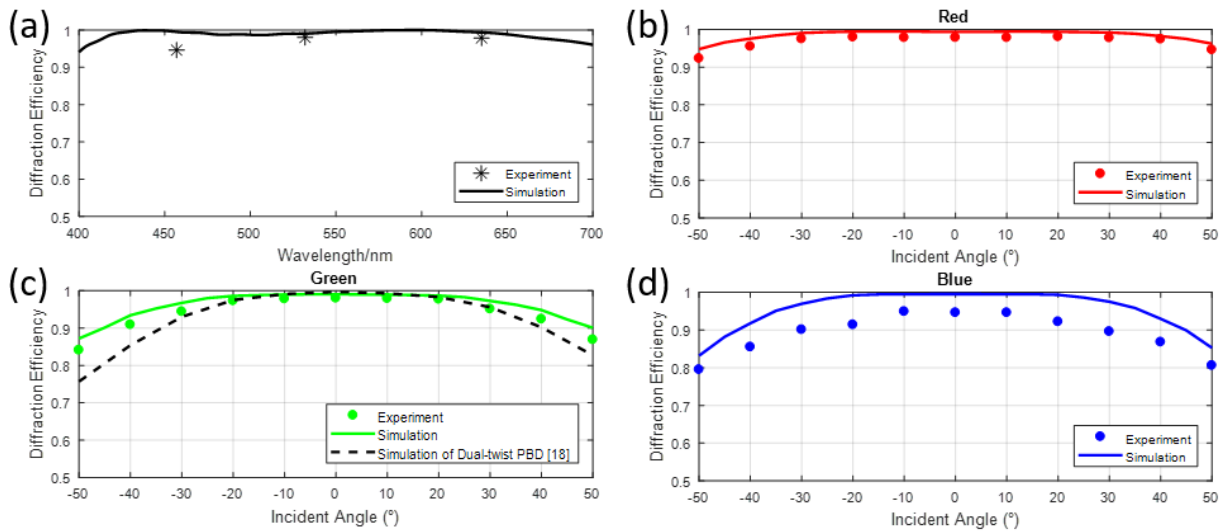


**Figure 2-4: (a) Wavelength spectrum of the three-layer PB grating and angular spectrums of the three-layer PB grating at (b) red, (c) green and (d) blue wavelengths.**

## 2.2 Reflective Type LC Flat Optical Elements
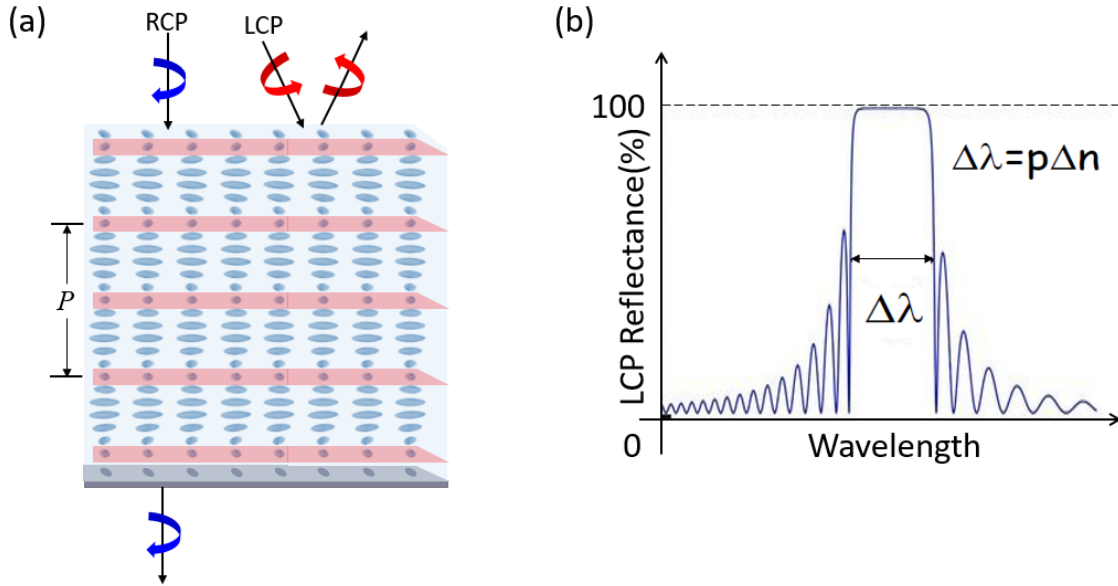


**Figure 2-5: (a) Schematic of cholesteric liquid crystal film, and (b) reflection band with circular polarization input.**

The reflection type LC flat optical elements in this dissertation are called polarization volume hologram (PVH) [24,56,57], and they are also based on the geometric phase, whose phase profile depends on the LC directors' phase pattern. The mechanism of reflection originates from Bragg reflection [24,58]. As shown in Fig. 2-5(a). the LC molecules have a helical structure, which is called cholesteric liquid crystal (CLC). Then, the circularly polarized light with the same handedness will experience periodically changing refractive index. Therefore, Bragg reflection can be established. The bandwidth of Bragg reflection depends on the LC pitch length and the birefringence [58,59], as described in Fig. 2-5(b). However, the opposite circularly polarized light will transmit through. This type of Bragg reflection can achieve high efficiency approaching 100%, when the LC is thick enough [24,58]. The full color performance can also be achieved by gradient pitch design [60,61] or vertically stacking multiple CLC layers together [59,62].
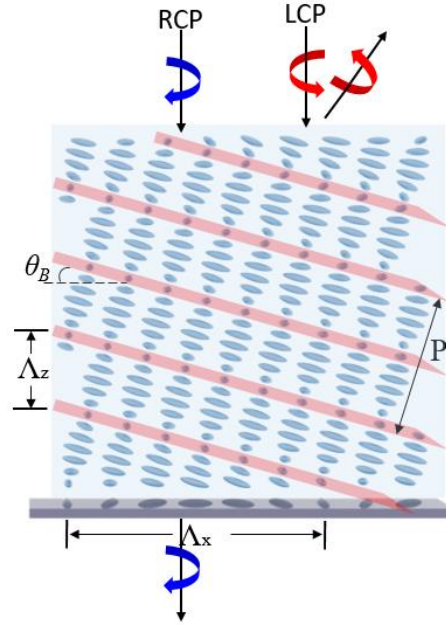
**Figure 2-6: Schematic of reflection-type LC flat optics, polarization volume grating.**

Like the transmission type LC flat optical elements, once the LC directors are patterned into a certain phase profile, this optical element will exhibit the corresponding functionality. If the LC directors are linearly changing, the device will perform as a polarization volume grating (PVG) [24,57]. The device structure and working principle are illustrated in Fig. 2-6. The Brag plane also tilts at an angle $\theta_B$. The PVG also performs as a slanted grating [54,63]. The diffraction efficiency is related to the grating thickness, and the diffraction angle follows the grating equation. The diffraction bandwidth and central wavelength have similar properties as CLC. Using gradient pitch or stacking layers also help to achieve full color performance [64,65]. Same as the transmission type LC flat optical elements, the PVHs can also be patterned to an arbitrary phase profile in theory, but following the same intrinsic working principle.

## 2.3 Fabrication Methods

Several methods have been developed to align the LC molecules. Based on their mechanisms, these approaches can be classified into volume/bulk alignment and surface alignment. The working principle of volume alignment is through volume hologram. An optical interferometer is used to produce the desired light field in space, so that the corresponding pattern can be recorded in the LC substrate. However, to achieve volume alignment requires a high intensity light field to perform the task, because it uses a solid LC polymer with multiple side groups, which presents an isotropic initial state [66,67]. In recent years, volume aligned LC optical elements with a high diffraction efficiency (>95%) at certain wavelengths have been reported [68,69]. In comparison with volume alignment, surface alignment is easier to fabricate and can achieve a higher diffraction efficiency. In surface alignment, there is a thin alignment layer with grating pattern between the LC and glass substrate. Two techniques have been widely used to create the grating pattern: mechanical patterning and optical patterning. In mechanical patterning, microrubbing [70] and nanoimprint [71] methods have been reported. Due to the limited degree of freedom in microrubbing, it usually produces a binary phase grating, so this method is difficult to produce geometric phase with a large degree of freedom. Nanoimprint method utilizes photo lithography to write a high-resolution stamp, then the pattern on the stamp can be imprinted onto the alignment layer. Photolithography has high degrees of freedom, and imprinting process is simple and fast. Therefore, nanoimprint method is a good candidate for practical mass production, but the defects issues need to be solved. In optical patterning, the alignment layer will not be physically graved, but the alignment layer molecules will be reoriented by a polarized light, and the approaches including direct writing [26], projection lithography [72] and interference exposure

[73]. Direct writing uses a single laser line and a polarization modulator to "pixelize" the direction of the alignment molecule. This approach can produce arbitrary phase pattern, but it is time consuming for large scale production. Projection lithography can directly pattern the polarization light field, generated by a spatial light modulator (SLM), on the alignment layer. This patterning method is easy and fast, but the pattern quality (resolution and smoothness) is limited by the SLM. Different to projection lithography, the interference exposure generates the polarization light field by holography interferometer, which can achieve a smaller grating period and smoother phase change. This method is adopted in our lab.
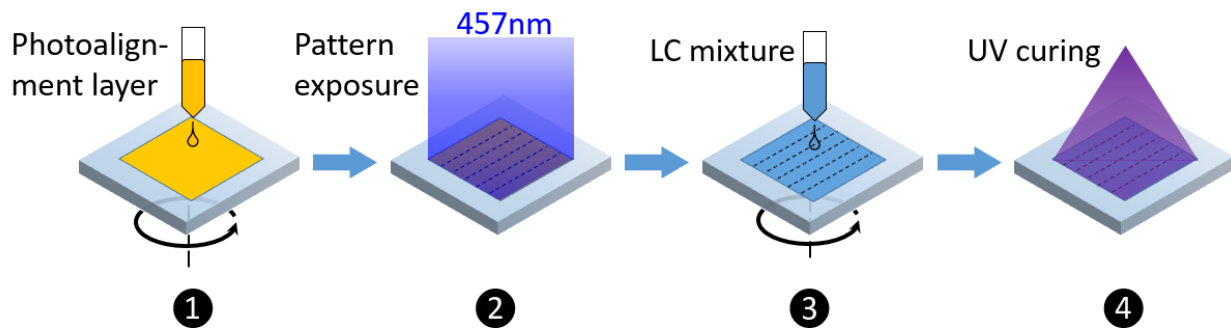


**Figure 2-7: Fabrication process of LC flat optics with photo-alignment and spin coating.**

Figure 2-7 shows the LC flat optics fabrication process. In the first step, a thin photo-alignment layer is spin-coated on a clean glass substrate. Then the sample is set on the output of the interferometer for the pattern exposure. The format of interferometer can be designed for different phase pattern. The principle is based on two beam hologram [74]. One arm is reference beam, while the other is signal beam. After pattern exposure, we can spin-coat the LC solution on the sample. The LC molecules will follow the pattern on the photo-alignment layer. Next, the sample will be put under the UV light for curing. Finally, we can get a polymerized LC film. For the multi-twist layer LC flat optics, steps 3 and 4 will be repeated multiple times. Each LC film

thickness and LC twist angle can be tuned by adjusting the spin-coating parameters and LC

solutions.

# CHAPTER 3: HIGH OPTICAL EFFICIENCY VR SYSTEM

The content of this chapter was previously published in [9].

## 3.1 Background

The basic device structure of a VR system consists of a display panel and an imaging optics [75]. Although the optical structure is simple, as a near-eye display the form factor, weight, and power consumption are essential ergonomics for long-term wearing experience in addition to high image quality. To reduce weight, Fresnel lens is a strong contender for VR imaging optics, and it was first adopted into practical systems in the late 1980s by VPL Eyephone LX [76]. Until recently, some commercial VR headsets are still using Fresnel lens, such as HTC VIVE and Google Daydream. On the other hand, the folded optics (often called "pancake" structure) has also been developed to reduce the form factor [77,78]. Such a "pancake" structure can also be combined with holographic optical elements [79] or Fresnel lens [80] to further reduce the system weight and form factor. However, a major shortcoming of the "pancake" structure is its relatively low optical efficiency. The maximum optical efficiency is 25% because the light passes through the polarization selective cavity multiple times, and each time it encounters some optical loss due to the "half mirror" [79]. Such a low light efficiency will increase the power consumption and bring more burden to the power supply [16]. Therefore, improving the light efficiency of a VR system is an urgent task, especially for the "pancake" structure.
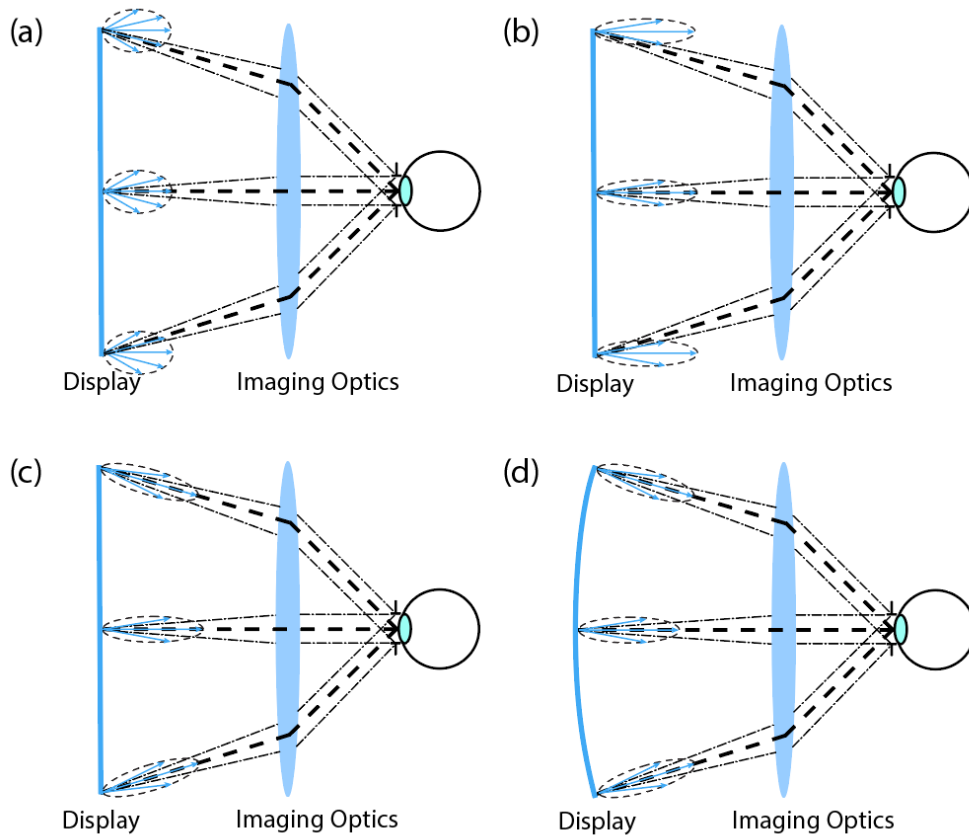
**Figure 3-1: Schematic of a VR system with different kinds of light sources: (a) conventional BL, (b) directional BL, (c) directional BL with primary emission direction correction, and (d) 2D curved display.**

At present time, several VR systems share a common optical structure shown in Fig. 3-1(a). From Fig. 3-1(a), we can see that the corresponding solid angle of the eye pupil is small, which only occupies a small portion of the display pixel's angular spectrum. Therefore, only a fraction of the emitted light from the display panel is captured by the observer, resulting in a low light efficiency. To enhance the light efficiency, a directional backlight (BL) display is preferred [17,81]. Thanks to the directional BL, most of the light emitted by the central area will enter the pupil. However, the light efficiency of peripheral pixels cannot be improved, due to the mismatch between the primary emission direction and the corresponding chief ray direction as Fig. 3-1(b)

17

shows. To overcome this problem, the primary emission direction of pixels on the display should be modified, so that the peripheral pixels can also be steered into the pupil (Fig. 3-1(c)). Moreover, when a directional BL is used, bending the curvature of display panel [82] can also improve the light efficiency, as Fig. 3-1(d) depicts. Nonetheless, this solution demands a two-dimensional (2D) curved display, which is challenging to fabricate.

### 3.2 Diffractive Deflection Film

The DDF we developed is essentially a multi-domain PB lens [34,50], where the focal length varies within different radius range. Fig. 3-2 shows the pattern exposure setup for fabricating such a multi-domain PB phase lens. In experiment, we designed a three-domain PB lens; the size and the area of each domain are the same as the photomask shown in Fig. 3-2. The three-domain mask was fabricated by a femtosecond laser (Pharos, Light Conversion). The laser beam (wavelength 1030 nm, pulse duration 170 fs, repetition rate 1 kHz, and average power 600 mW) was focused on a plain photomask (CAD/Art Services, Inc) with a focal length of 1000 mm. The photomask was attached to a 3D translation stage for precise scanning. Each of the three rings on the photomask was cut at a scanning speed of 10 mm/s in multiple runs till it gets completely through. All these three domains (1, 2, and 3) are concentric, and their outer diameter is 22 mm, 32 mm, and 40 mm, respectively. After the alignment layer (0.2% brilliant yellow dissolved in Dimethyformamide) was spin-coated onto the top surface of a clean substrate (2-inch by 2-inch), the photomask was adhered to the back surface of the sample substrate. Then the substrate with the photomask was placed at three different positions (1, 2, and 3 as marked in Fig. 3-2) for the holography pattern exposure [26,34]. At each position, the corresponding domain of the

18

photomask was opened, so that only one domain was exposed at a time. Due to the position difference during exposure, the focal length of each domain is different. In this way, a three-domain PB lens pattern was recorded on the alignment layer. The focal length of each domain depends on the imaging optics, and its value will be specified later. After the pattern exposure, we spin-coated one layer of reactive mesogen mixture (RMM) onto the substrate. Then, UV photo-polymerization process was applied to cure and stabilize the polymer film. The components in the RMM include 95% reactive mesogen RM257 (from LC Matter), 4.9% photo-initiator Irgacure 651 (from BASF), and 0.1% surfactant Zonyl 8857A (from DuPont). This RMM was dissolved in toluene, and the ratio of solute to solvent was around 1:2.5. The polymer film thickness is optimized at a green wavelength. In practical applications, a multi-twist structure can be adopted to achieve broadband performance [47], and the chromatic aberration can be corrected by laminating a diffractive optical film to the refractive optical element [34].
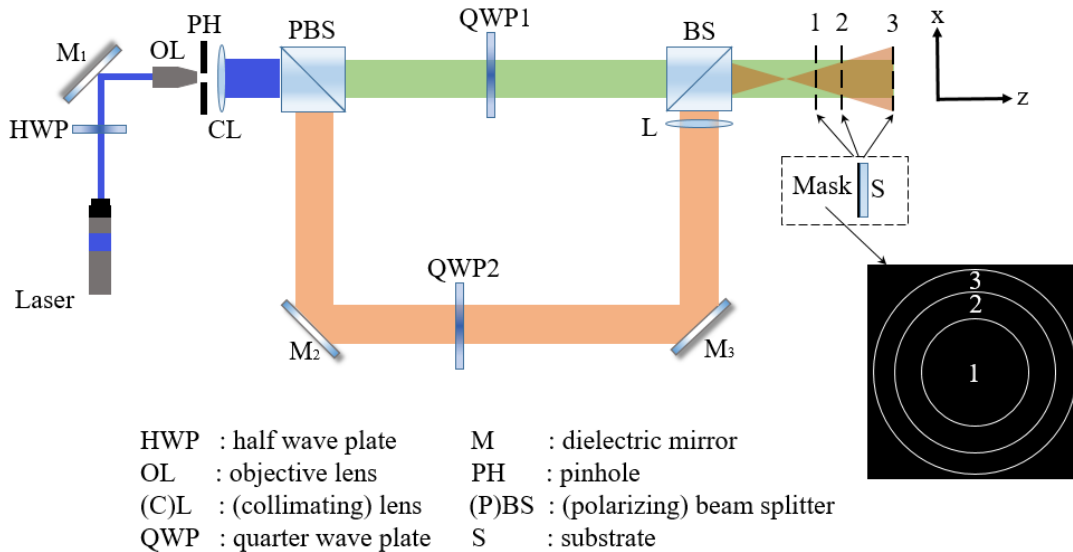


**Figure 3-2: Experiment setup for multi-domain lens pattern exposure.**

Fig. 3-3(a) shows a photo of the fabricated three-domain PB lens, where three imaging domains are clearly observed. In the photo, the imaging background is the floor tiles of a corridor, and we can see that the focal length of each domain is different because the tile edge shows a sharp jump at the boundary between domains. The focal length of the 1, 2 and 3 domains is 12 cm, 17 cm, and 35 cm, respectively. The choice of a focal length depends on the chief ray direction of each pixel. In our lab, we do not have the setup to fabricate a pixel-level DDF, which requires a direct writing equipment [83]. We calculate the corresponding "focal length" ($f = d/\tan(\theta)$, where $f$ is the "focal length", $d$ is the distance between the pixel and the display center, and $\theta$ is the deflection angle) for the pixels along the radius direction, and the "focal length" does not change abruptly. For the pixels within a certain area, their corresponding "focal lengths" are similar. Therefore, we can use a PB lens to deflect the primary emission direction of the pixels in this area. Based on the "focal length" variation along the display radius, we divide the display into three domains, so that the primary emission direction of most pixels on the display can be deflected to the desired direction. Fig. 3-3(b) is a photo of the lens pattern in the central area of domain 1, captured by a polarization microscope (OLYMPUS BX51). Fig. 3-3(c) shows the microscope image at the boundary area. It is clearly shown that the alignment quality is degraded at the boundary area. This is because the photomask domains do not match each other perfectly and the boundary is exposed twice. The width of the boundary is about 150 μm. However, the impact of such a narrow boundary to our experimental results is negligible.
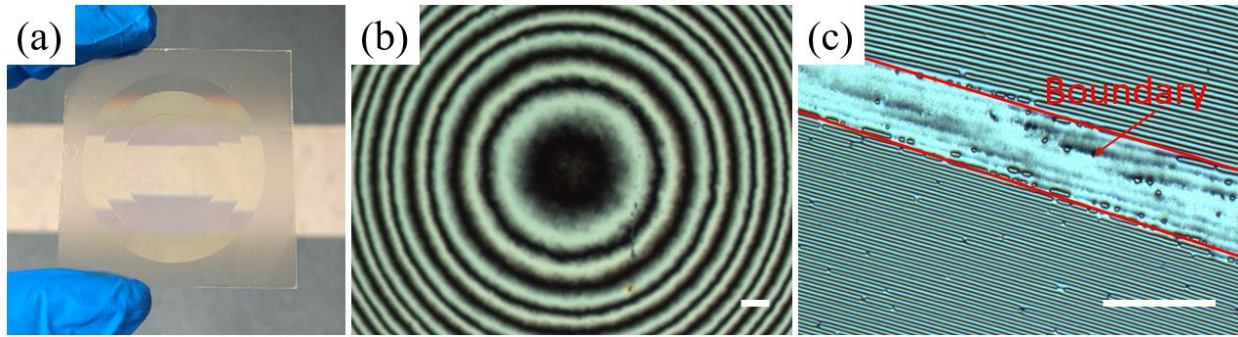
**Figure 3-3: Fabricated three-domain PB lens: (a) imaging photo, polarization microscope photo of (b) lens center and (c) domain boundary. The scale bar in the figure is 200μm.**

### 3.3 Fresnel VR System
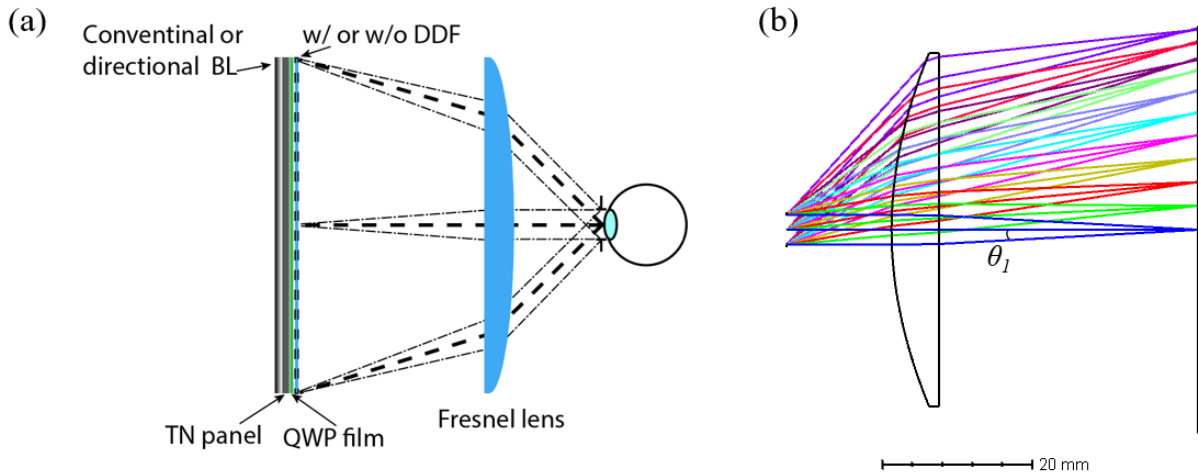


**Figure 3-4: (a) Schematic of Fresnel VR system in the experiment, and (b) Zemax profile of the Fresnel lens.**

In this section, we describe the three VR systems we built using a Fresnel lens. These three systems use the same TN panel as the display but have different emission angular spectra by using a conventional or directional BL with and without a DDF (Fig. 3-4(a)). For consistency, a quarter-wave plate (QWP) film was laminated to the TN panel, which converts a linearly polarized light to a left-handed circularly polarized (LCP) light. Because such a three-domain PB lens is polarization dependent [29,84], only the LCP light will see the positive lens effect in the design. Fig. 3-4(b) shows the Zemax profile of the Fresnel lens we used.

For the first and the second Fresnel VR systems, they do not use a DDF to modulate the primary emission direction of each pixel. All the pixels on the panel have the primary emission directions perpendicular to the panel's surface. The difference of these two Fresnel VR systems is that they use different BLs with different angular distributions and luminous flux. The first one uses an edge-lit BL (Adafruit Industries) with two brightness enhancement films [85]. The second system uses a directional backlight. This directional BL consists of a collimated LED backlight (Edmund Optics #14270) and a two-layer privacy film (3M PF170C4B). The reason we added such a two-layer privacy film is to narrow down the angular spectrum of the collimated LED BL. The angular spectra of these two BLs were measured by a goniophotometer (TechnoTeam Vision), and results are shown in Fig. 3-5(a). According to the normalized angular spectrum, the conventional BL has a full width at half maximum (FWHM) of about ±24º, while the directional BL has about ±14º. After integrating the angular spectrum of two BLs in the spherical coordinates, the total luminous flux of the directional BL is about 30.7% higher than that of the conventional one. To make a fair comparison, we adjusted the gray level of TN panel so that the total luminous flux of these two BLs is the same. The Fresnel lens was inserted between the display and the observer as Fig. 3-4(a) shows. The distance between the display and the Fresnel lens is 35 mm, and the eye relief is 14 mm. The images at the eye pupil of these two VR systems with different BLs are shown in Fig. 3-5(b) (conventional BL) and 5(c) (directional BL). When we took these two photos, the settings of camera remained the same. From the figures, we can see a significant light efficiency enhancement when the directional BL is applied to the VR system.

**Figure 3-5: (a) Normalized angular distribution of conventional BL and directional BL. Imaging results of Fresnel system with (b) conventional BL, and (c) directional BL. The horizontal FOV of the images in (b) & (c) is around ±15º.**

To quantify the light efficiency enhancement introduced by the directional BL, we also established a VR simulation model in LightTools, as Fig. 3-6 depicts. In this model, we use a linear light source consisting of 21-point sources with 1-mm gap in between. As a result, the corresponding half field of view (FOV) is 35º, which is less than that of our Fresnel lens (half FOV ≈ 50º). This is because the size of our DDF substrate and directional BL is not large enough to cover the entire FOV of the Fresnel lens. The reason we use point sources to represent a line source is that the primary emission direction changes slowly along the radius direction, and the surrounding pixels (the distance to the corresponding point source is less than 1 mm) have similar primary emission direction as the point source. In our system, when the pixels have the same angular distribution, it is the primary emission direction that influences the light efficiency. Therefore, we set the gap between these point sources to be 1 mm, which is dense enough to represent the experimental condition. The eye pupil (the receiver in the simulation, the entrance pupil of the camera in the experiment) size is 4 mm. During simulation, the angular distributions of the conventional BL and the directional BL in Fig. 3-5(a) are imported into our LightTools program. All other parameters such as light source power, lens, and receiver settings in the systems remain the same. After calculation, the power on the receiver when using the directional BL is

1.91x higher than that using the conventional BL. In experiment, a CMOS (Complementary Metal Oxide Semiconductor) camera (TechnoTeam Vision, LMK6 color) was used to detect the color imaging and luminance at the eye pupil.
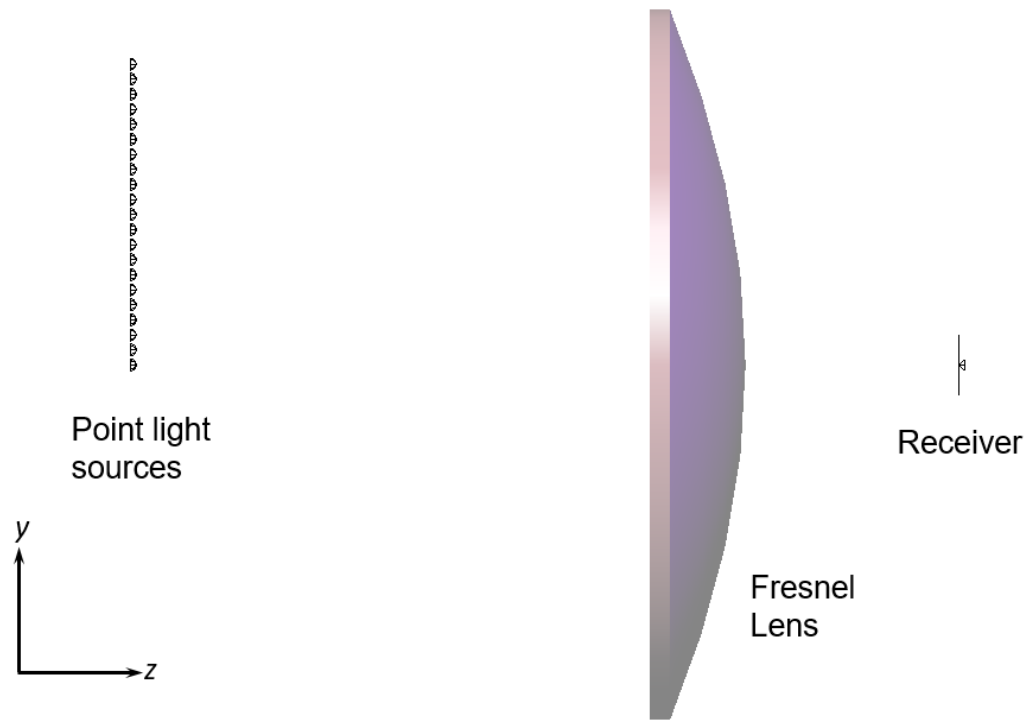


**Figure 3-6: Fresnel system setup in LightTools.**

The color imaging results using a conventional BL and a directional BL are shown in Fig. 3-7(a) and 7(c), respectively, and the corresponding luminance distributions are shown in Fig. 3-7(b) and 7(d). According to the measurement, the average luminance of imaging pixels is 83.7 nits for the conventional BL (Fig. 3-7(b)), while this value is 183.8 nits for the directional BL (Fig. 3-7(d)). On the other hand, the luminous flux of the directional BL is about 30.7% higher than that of the conventional BL. Therefore, the light efficiency of the directional BL based VR system is 1.68x higher than that of the conventional BL. The simulation results agree with experiment reasonably well.
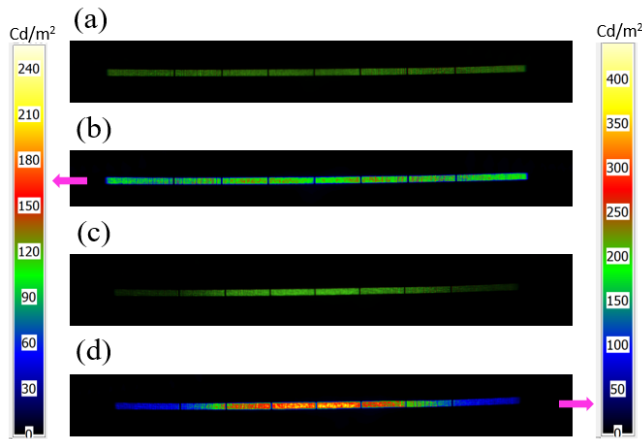
**Figure 3-7: Imaging results of the Fresnel system with (a) a conventional BL and (c) a directional BL. Luminance distribution results of the Fresnel system with (b) a conventional BL and (d) a directional BL.**

Next, we added a DDF to the top of the display panel as Fig. 3-5(a) depicts, which uses a directional BL. This DDF has the same size and diameter as the one shown in Fig. 3-3(a), but the focal length of each domain is 7 cm, 8 cm, and 10 cm, respectively (from domain 1 to domain 3), which is designed according to the chief ray directions shown in Fig. 3-4(b). To make the comparison more conveniently, we used a blade wrapped by a cleaning tissue, which was rinsed with acetone to remove half of the DDF off the substrate. As a result, only half of the display panel still has the DDF to correct the primary emission angle of the pixels, while the other half does not. Fig. 3-8(a) shows the imaging result and Fig. 3-8(b) shows the luminance distribution. The left part of imaging pixels (w/o DDF) has an average luminance of 165.5 nits, while the right part (w/ DDF) has 221.8 nits. After comparison, the light efficiency enhancement is 34.0% by adding a DDF. In simulation, we adjust the primary emission direction of each point source based on Fig. 3-4(b), where we can read the primary emission (chief ray) directions of the corresponding pixels from Zemax. The power detected by the receiver is increased by 30.0%, which is consistent with the experimental data. The reason our experimental result is slightly higher than the simulated one

25

is that the peak luminous intensity of our directional BL (Fig. 3-5(a) blue line) is not at the primary emission direction (normal direction), and the surrounding emission directions have higher luminous intensities than the primary emission direction. Since our three-domain PB lens is not an ideal DDF, which will introduce some mismatching between the primary emission direction and the chief ray direction (Fig. 3-4(b)) for some pixels, so that the surrounding emission directions with higher luminous intensities can match the chief ray direction in experiment. However, in simulation we can ideally control the deflection angle of each light source, and the primary emission direction exactly matches the chief ray direction. Thus, the light efficiency enhancement obtained from simulation is somewhat higher than that from experiment.
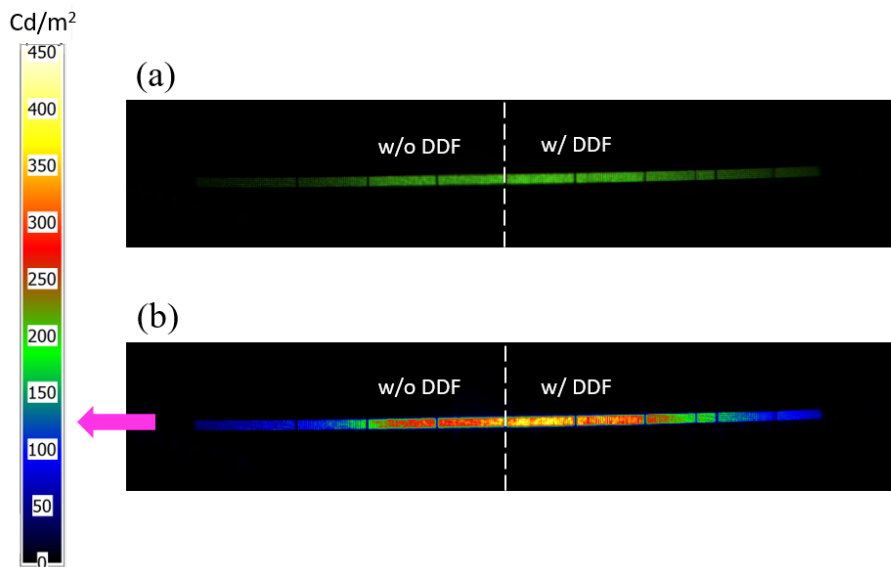


**Figure 3-8: (a) Imaging and (b) luminance distribution results of the Fresnel system with directional BL and half DDF.**

### 3.4 "Pancake" VR System

The "pancake" VR system has a similar structure to the Fresnel system shown in Fig. 3-4(a) but adopting a "pancake" lens as the imaging optics. The Zemax profile is plotted in Fig. 3-

9(a). The front surface of this "pancake" lens is a reflective circular polarizer, which reflects the right-handed circular polarized (RCP) light, while transmitting the LCP light. The back surface of the pancake lens is a half mirror. The distance between pancake lens and display panel is 16 mm, and the eye relief is 13 mm. A conventional BL and a directional BL (same as what we used in the Fresnel system) were used in the system display, respectively. Their imaging results are shown in Fig. 3-9(b) (conventional BL) and Fig. 3-9(c) (directional BL). The light efficiency enhancement by using a directional backlight is quite significant.



**Figure 3-9: (a) Zemax profile of the "Pancake" lens. Imaging results of "Pancake" system with a (b) conventional BL and (c) directional BL. The horizontal FOV of the images in (b) and (c) is ±23º.**

Similar to what we did in the Fresnel system, a "pancake" VR model was built in LightTools to quantify the light efficiency improvement introduced by the directional BL. In this model, we use a 19-mm-long linear light source comprising of 20 point sources with 1-mm gap in between, which corresponding to a 50º half FOV. The reason the "pancake" VR system can achieve 50º half FOV is that the aperture size of the "pancake" lens is small, so that the size of the DDF substrate and the directional BL is no longer a limitation. The eye pupil size is still 4 mm. During simulation, the angular spectra of conventional BL and directional BL are the same as those we use in the Fresnel system. After calculation, the power on the receiver when using the directional BL is 2.39x higher than that of the conventional BL. In experiment, the imaging results

of conventional BL and directional BL are shown in Fig. 3-10(a) and 10(c), respectively. The corresponding luminance distribution is shown in Fig. 3-10(b) and 10(d). After evaluation, the average luminance of imaging pixels is 23.4 nits for the conventional BL (Fig. 3-10(b)), and 67.4 nits for the directional BL (Fig. 3-10(d)). Considering that the directional BL has a 30.7% higher luminous flux, the light efficiency of the directional BL "pancake" VR system is 2.20x higher than that of the conventional BL. Therefore, the simulation results are in good agreement with the measured data.
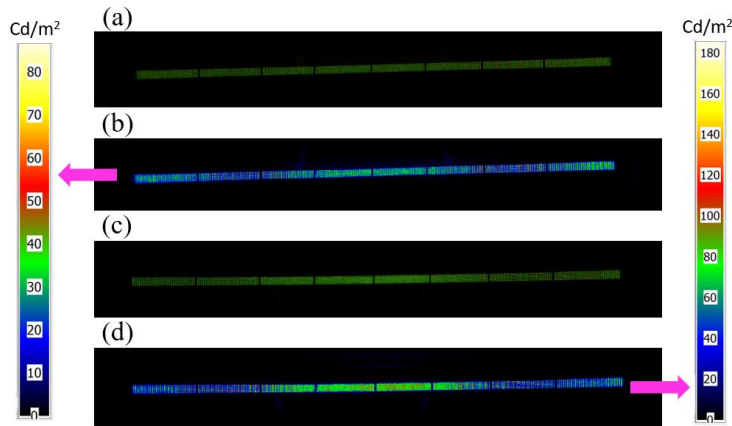


**Figure 3-10: Imaging results of the "pancake" system with (a) conventional BL, and (c) directional BL. Luminance distribution results of the "pancake" system with (b) conventional BL, and (d) directional BL.**

To study the light efficiency enhanced by the DDF in a "pancake" VR system, we added a DDF on the top of the display panel. This DDF is the one shown in Fig. 3-3(a). The focal length of each domain (from 1 to 3) is 12 cm, 17 cm, and 35 cm, respectively. Similar to the Fresnel system, we wiped off half of the DDF on the substrate for the convenience of comparison. However, a major difference between the Fresnel lens and the "pancake" lens is that the latter is strongly polarization selective, but the former is not. Thus, we choose RCP as the input light in the "pancake" system. On the other hand, our three-domain PB lens is also a polarization dependent

28

device. In our design, this three-domain PB lens is converging only for the LCP input. Therefore, we need to select a proper circularly polarized input light based on whether it will pass through the DDF. Such a system structure is shown in Fig. 3-11. After passing the TN panel, the 45° linearly polarized light is converted to LCP or RCP by arranging the fast axis of QWP film either in horizontal or vertical direction. Half of the input light, say RCP, passes through the glass substrate and its polarization state remains unchanged. The other half of the input light (LCP) passes through the DDF, and its polarization state changes from LCP to RCP. Therefore, all the input light to the "pancake" lens has the same polarization (RCP).
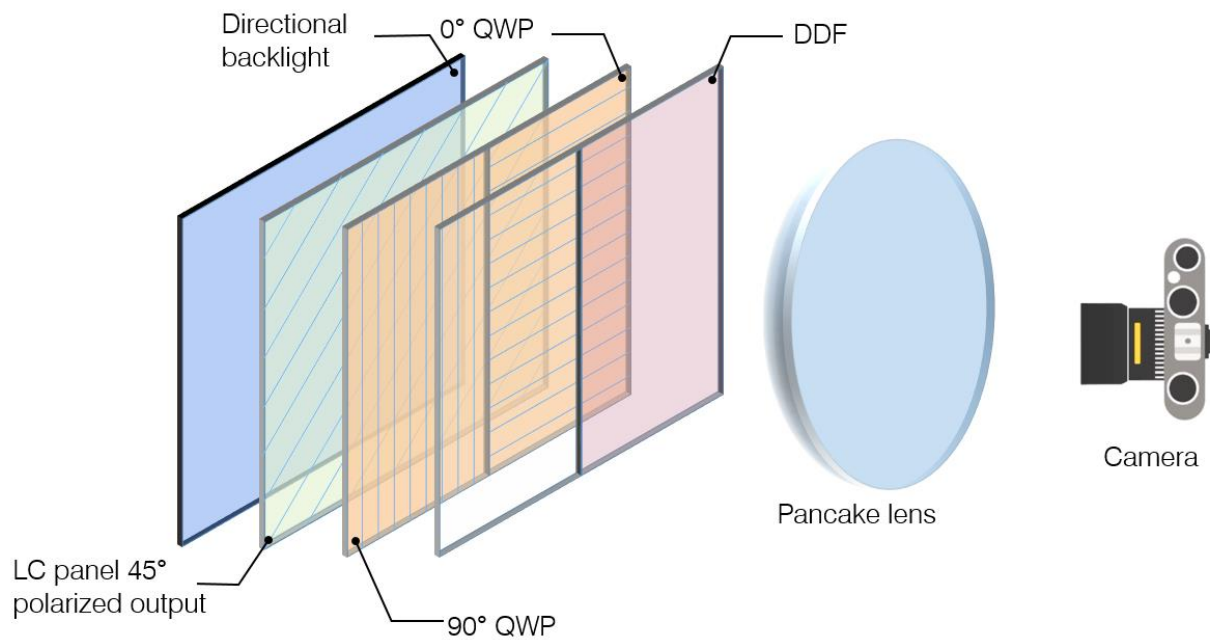


**Figure 3-11: Schematic of Pancake VR system with a directional BL and a half DDF.**

Fig. 3-12(a) shows the imaging result and Fig. 3-12(b) is the measured luminance distribution. The average luminance of the left part (w/ DDF) imaging pixels is 59.45 nits, and the right part (w/o DDF) is 58.08 nits, which indicates the light efficiency is improved by 2.36% by adding the DDF. During simulation, we adjust the primary emission direction of each point source

according to the chief ray direction in Fig. 3-9(a). The power detected by the receiver is increased by 2.12%, which is consistent with the experimental data. The main reason we do not see a significant improvement after adding the DDF is because the "pancake" lens is designed to be telecentric [86], so that the chief ray direction in Fig. 3-9(a) is already very close to the primary emission direction of the display panel.
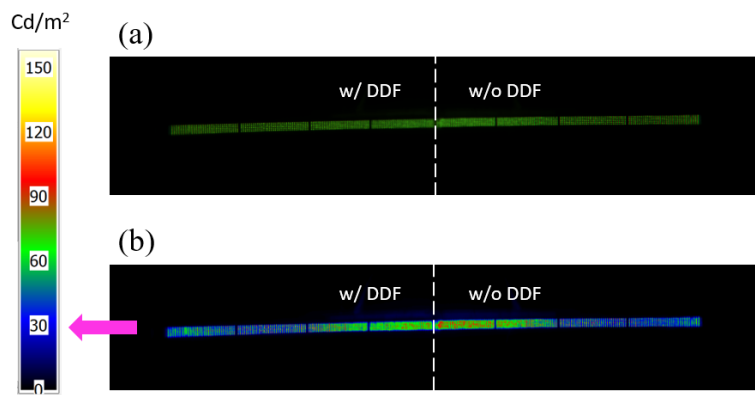


**Figure 3-12: (a) Imaging and (b) luminance distribution results of the "pancake" system with a directional BL and a half DDF.**

## 3.5 Discussion

We summarize the experimental and simulation results in Table 3-1. Here, we normalize the light efficiency to a conventional BL for both Fresnel and "Pancake" VR systems. There are two steps in our light efficiency enhancement process. The first step is to apply a directional BL, and the second step is to add a DDF. According to the normalized results in Table 3-1, we find that after these two steps the Fresnel system and the "pancake" system exhibit a similar light efficiency enhancement. The difference is how much enhancement is achieved in each step. For the Fresnel system, both steps contribute an obvious enhancement, while most of the enhancement for the "pancake" system occurs in the first step. This is because the "pancake" lens is more telecentric than the Fresnel lens in our experiment. In other words, the telecentric design

30

strengthens the effect of the directional BL, but impairs the enhancement brought by the DDF. However, the telecentric design would cause more aberration. With the help of a DDF, the "pancake" lens does not need to be telecentric anymore, so that the VR display can achieve a better image quality.

**Table 3-1: Simulation (Sim.) and experimental (Exp.) results of normalized light efficiency of the Fresnel and "pancake" lens-based VR display systems.**

| Light efficiency (a.u.) | Conventional BL | | Directional BL | | Directional BL with DDF | |
|---|---|---|---|---|---|---|
| Fresnel VR | Sim. | Exp. | Sim. | Exp. | Sim. | Exp. |
| | 1 | 1 | 1.91 | 1.68 | 2.48 | 2.25 |
| "Pancake" VR | Sim. | Exp. | Sim. | Exp. | Sim. | Exp. |
| | 1 | 1 | 2.39 | 2.20 | 2.44 | 2.25 |

Furthermore, we notice that after applying the directional BL and DDF, the light efficiency enhancement of the Fresnel and the "pancake" systems is similar. The enhancement is not heavily related to the employed imaging optics but is largely dependent on the BL's angular distribution and the solid angles corresponding to the eye pupil ($\theta_1$ in Fig. 3-4(b) and $\theta_2$ in Fig. 3-9(a); for convenience, here we use the half apex angle to represent the corresponding solid angle). By integrating the angular distribution in the solid angle $\theta_1$ of the directional BL and the conventional BL, we find that the luminous flux of the directional BL is 3.18x higher than that of the conventional BL. Since the directional BL has a 30.7% higher total luminous flux than the conventional one, the normalized result should be 2.43x ($\mathbf{3.18 \div 1.307 = 2.43}$). This value is consistent with the simulated one (2.48x) of the Fresnel VR system using a directional BL and a DDF. Next, we repeat the same process for the "pancake" system. The luminous flux of the directional BL is 2.39x higher than that of the conventional BL (the 30.7% higher luminous flux

31

of directional BL has already been included), which is obtained by integrating the angular distribution in the solid angle $\theta_2$ of these two BLs. This result is also consistent with the simulated one (2.44x) shown in Table 3-1.

It is worth mentioning that the light efficiency enhancement brought by the DDF benefits the peripheral pixels. The intensity distribution at the eye pupil is simulated by LightTools, and results are shown in Fig. 3-13(a). From Fig. 3-13(a), we can see that the maximum intensity is not located at the pupil center, because the maximum intensity on the receiver will shift toward the positive Y direction as the position of light source is far away from the optical axis of the lens (Fig. 3-5). This also explains why the vignetting is much more serious in the Fresnel system (Fig. 3-6(c)) after applying a directional BL. As a matter of fact, the vignetting is not so serious as the experimental imaging results shown in Fig. 3-6, 3-7, 3-9 and 3-11, when observed by human eye. In experiment, the CMOS camera has an ultra-wide FOV objective lens (~±60° FOV), which would introduce a significant aberration for the large FOV pixels. With the help of DDF, the primary emission direction can be corrected, so that the maximum intensity returns to the pupil center (Fig. 3-12(b)), thereby alleviating the vignetting problem. For the "pancake" system, the vignetting is not so serious as the Fresnel system, because the "pancake" lens has a telecentric design, but we can still see the maximum intensity shifting from the pupil edge to the center according to the simulation results in Fig. 3-12(c) and 12(d). From the experimental results shown in Fig. 3-11(b), we also notice that the light efficiency enhancement is contributed by the peripheral pixels.
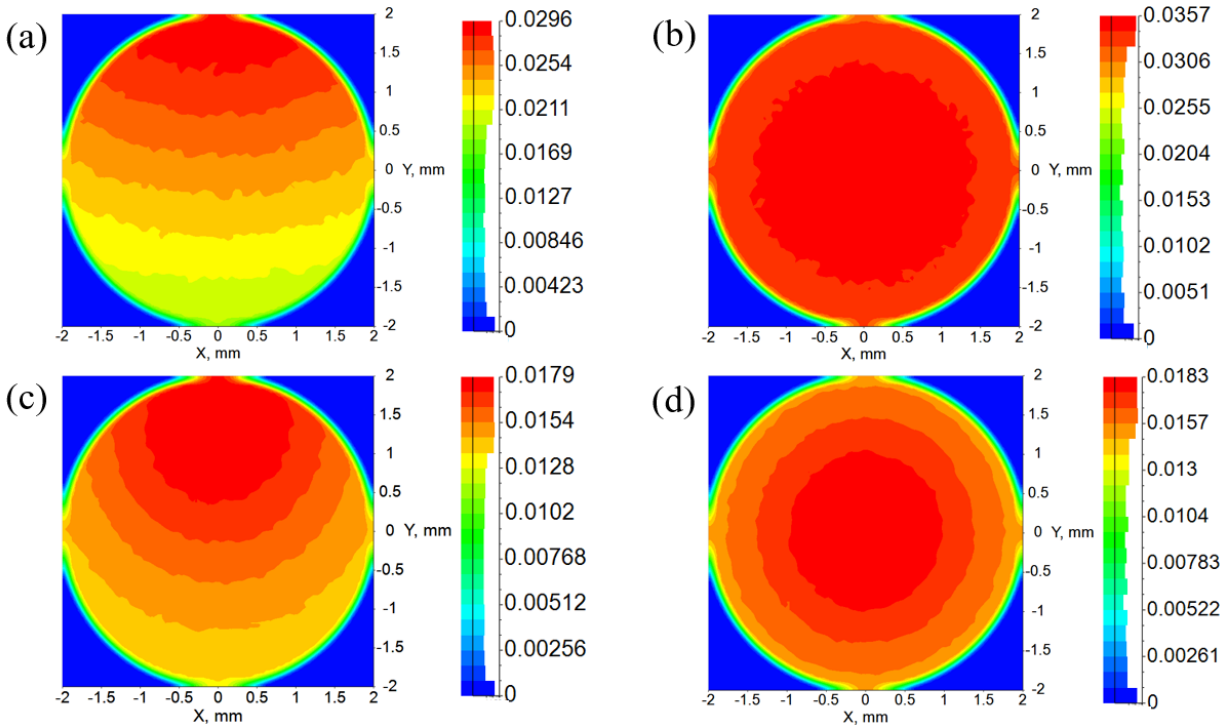
**Figure 3-13: Simulated intensity distribution at eye pupil for the Fresnel system (a) before and (b) after adding a DDF, and "pancake" system (c) before and (d) after adding a DDF. All these studies are with a directional BL.**

Currently, our directional BL has a FWHM of about 14°. But the half apex angle of the solid angle corresponding to the eye pupil in these two systems ($\theta_1$ in Fig. 3-4(b) and $\theta_2$ in Fig. 3-9(a)) is about 3° to 5°. Therefore, a portion of the BL is still wasted. If the FWHM of the directional BL can be reduced from 14° to 6°−10°, then the light efficiency enhancement will be more significant. However, a narrow angular distribution will result in a small eyebox. Therefore, the tradeoff between light efficiency and eyebox size should be taken into consideration.

The underlying principle for enhancing optical efficiency is to reduce the etendue waste in the system. A perfect system makes full use of the etendue from image generation unit to eyebox. Fig. 3-14 shows an ideal VR system with "zero etendue loss". In this system, the primary emission direction $\beta$ and angular width $2\theta$ of the display are a function of $r$, which represents the distance

from the corresponding pixel to the display center. According to the geometry shown in Fig. 3-14, we obtain the following relations:

$$\beta(r) = \arctan[(1-\frac{d}{f})\frac{r}{f}] \tag{3-1}$$

$$\frac{\cos^2\theta - \sin^2\beta}{f} = \frac{\sin 2\theta}{D} \tag{3-2}$$

where $d$ is the eye relief distance, $f$ is the focal length of the optical lens, and $D$ is the diameter of the eye pupil. From Eq. (3-1) and Eq. (3-2), we find $\beta = 0$ when $d=f$, which is independent of position, i.e., it is a telecentric system. Based on Eq. (3-1) and (3-2), we can optimize the DDF and the BL angular distributions to enhance the efficiency of a VR system. In our approach, we apply a PB-based DDF to tailor the emission pattern to transmit more etendue into the eyebox. Based on this principle, other types of DDF, metasurface, and curved display can also be used to enhance the VR system's optical efficiency. In addition, the display employed in the system is not limited to LED backlit LCD. Other types of displays such as mini-LED and micro-LED are also suitable if they have a reasonably narrow angular distribution.
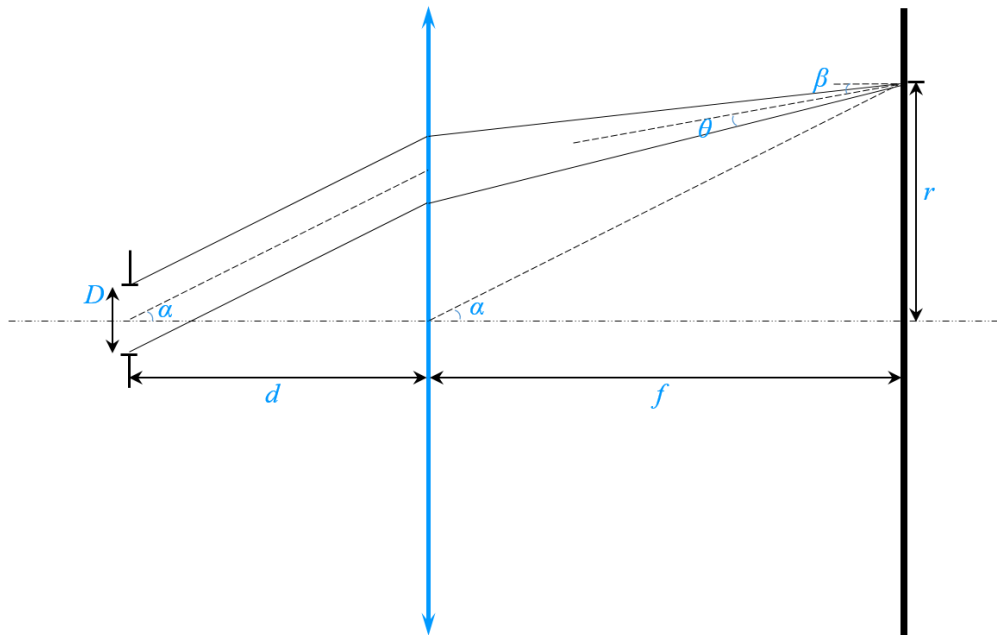
**Figure 3-14: Schematic of an ideal near-eye display system.**

<u>3.6 Summary</u>

In summary, we have achieved a significant light efficiency enhancement in both Fresnel and "pancake" VR systems with the help of a directional BL and a DDF. The employed directional BL has an angular bandwidth of $\pm 14°$ (conventional BL is $\pm 24°$). A three-domain PB lens is used as the DDF, and its focal lengths are designed according to the imaging optics of the system. In experiment, we obtained a 2.25x light efficiency enhancement for both Fresnel and "pancake" systems, which agrees well with our simulation results (2.48x for the Fresnel system and 2.44x for the "pancake" system). All the elements we utilized are cost effective and easily available. Widespread application of our approach to enhance the light efficiency of VR displays, especially for the "pancake" system, is foreseeable.

# CHAPTER 4: ULTRA-COMPACT VR SYSTEM

The content of this chapter was previously published in [13].

## 4.1 Background

After several decades of intensive development, virtual reality has achieved significant improvement. Currently, some commercial VR products have brought fabulous experience to users and enabled new applications in entertainment [3], engineering [6], education [4], and healthcare [5], just to name a few. However, the form factor of current VR headsets is still too bulky, which limits their long-time wearing. The basic optical system of a VR headset consists of a microdisplay located at the focal plane of an imaging optics [36]. In recent years, the thickness and weight of the light engine have been reduced significantly, benefiting from the rapid development of flat panel displays [87,88]. Therefore, the remaining improvement of form factor relies on miniaturing the imaging optics. There is an urgent need to develop an ultracompact and lightweight VR headset for comfortable long-time wearing.

Fig. 4-1 depicts the VR systems with different kinds of imaging optics. Fig. 4-1(a) is the conventional optical lens system consisting of a display panel and an optical lens. It has a large form factor and weight, and the optical efficiency is relatively low, because only a small portion of the emitted light from microdisplay can be collected by the lens and observed by the user, although it can achieve a decent imaging quality. To reduce the lens weight, a thin Fresnel lens is adopted in the VR system, as Fig. 4-1(b) shows. However, the Fresnel lens has sharp teeth in the imaging region, which will introduce stray light to the system [18,89] and degrade the imaging quality. Fig. 4-1(c) shows the pancake lens system, which takes the advantage of the folded optical

pathlength between two optical surfaces. As a result, it can achieve a higher focal power than the conventional lens, provided that the lens form factor remains at the same level. By using the pancake lens, both form factor and weight can be reduced significantly. However, a major trade-off is its dramatically reduced optical efficiency (only 25% as compared to the conventional one) due to the employed half mirror [79]. Although the holographic optical elements help to mitigate the optical loss in some designs because of the angular selectivity, the overall efficiency is still only about 30% due to the pancake structure [90]. Moreover, the zero-order light leakage and large angle incidence also produce stray light in the Pancake system, which degrades the imaging quality [18]. Currently, the thickness of a pancake-based VR system is still larger than 20 mm [15,91]. To further reduce the system form factor, here we propose to use a lenslet array and a deflector array as the imaging optics, as Fig. 4-1(d) depicts. In such a system, the lenslet aims to collect and collimate the light from microdisplay and then the deflector array can bend the collimated beam toward the exit pupil. Similar design using a lenslet array and Fresnel lens as imaging optics has also been proposed by Bang, et al [80]. Separating the collimating and bending processes help obtain more degrees of freedom during the design, which in turn benefits the imaging quality and eyebox. Compared to other systems in Fig. 4-1, our proposed system (Fig. 4-1(d)) enables a more compact form factor and lighter weight. Moreover, most of the collected light will enter the eye pupil so that the optical efficiency is also higher.
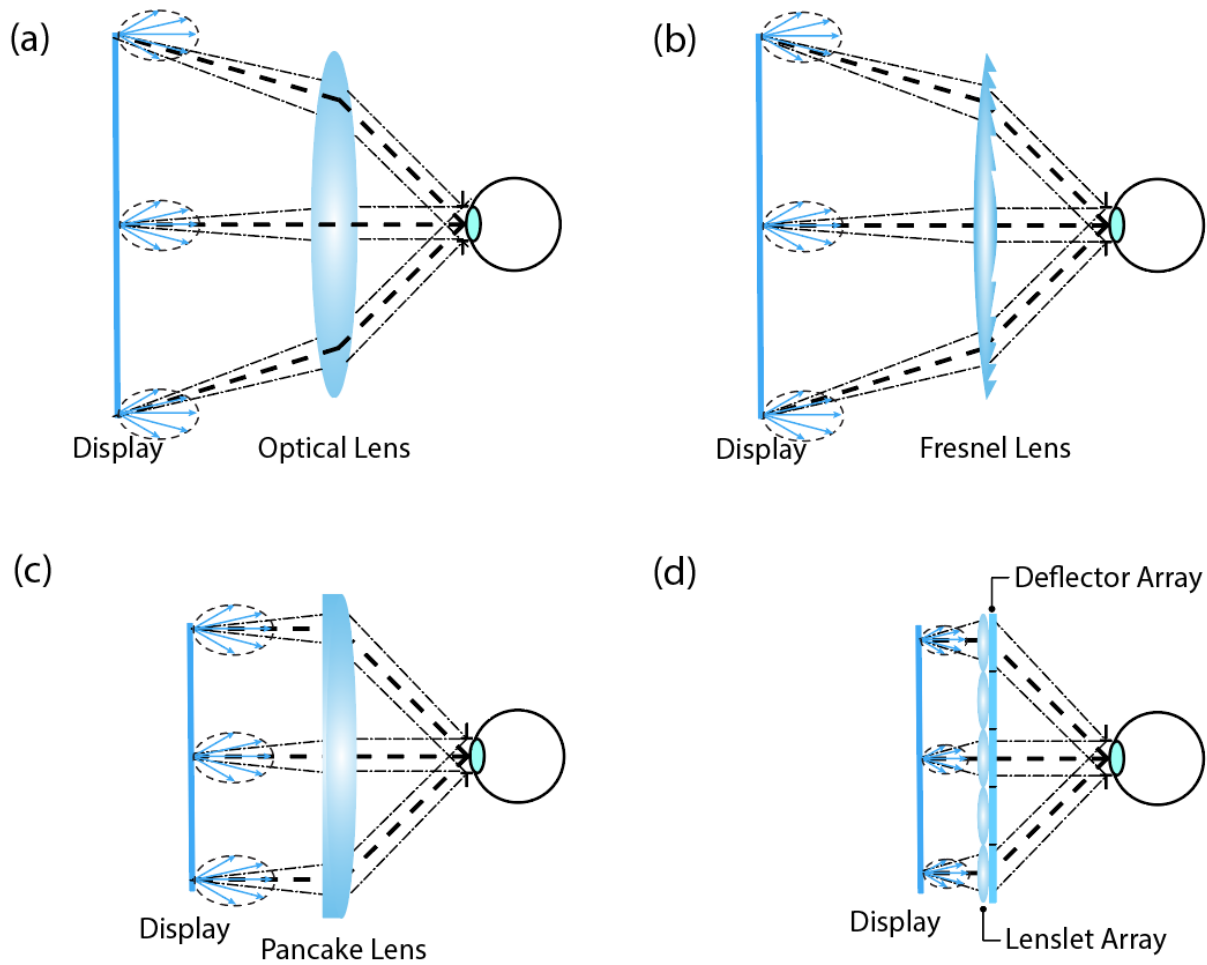
**Figure 4-1: Schematic of VR systems with different kinds of imaging optics: (a) conventional optical lens, (b) Fresnel lens, (c) Pancake lens, and (d) lenslet array and deflector array.**

4.2 System Configuration and Operation Principle

In our proposed system, the distance between the display panel and the lenslet array will heavily influence the system form factor. Therefore, a short gap between the display panel and the lenslet array is desired. However, the local vignetting such as imaging uniformity could be problematic. If we set the vignetting at 50%, then the distance between the display and the lenslet array ($d_1$) should be equal to the eye relief (L) for an ideal imaging system, as Fig. 4-2(a) shows. A comfortable eye relief should be no less than 15 mm. Therefore, the system thickness can be

reduced to around 15 mm. Usually, the thickness of the pancake system is larger than 20 mm. If the distance between the display panel and the lenslet array decreases to half an eye relief ($d_2=L/2$), then the vignetting will increase to 100% (Fig. 4-2(b)), and the thickness of the system can be less than 10 mm. Under such condition, the nonuniform imaging will be observed, that means some image content will be lost in the view. Therefore, to achieve an ultracompact form factor, we need to narrow down the angular distribution of the collimated beams in Fig. 4-2(b). Liquid crystal geometric phase optical elements exhibit several attractive features, including polarization selectivity, high diffraction efficiency, and compact form factor, and are promising for near-eye display applications [34,92]. These optical elements can be used to weaken the vignetting problem.
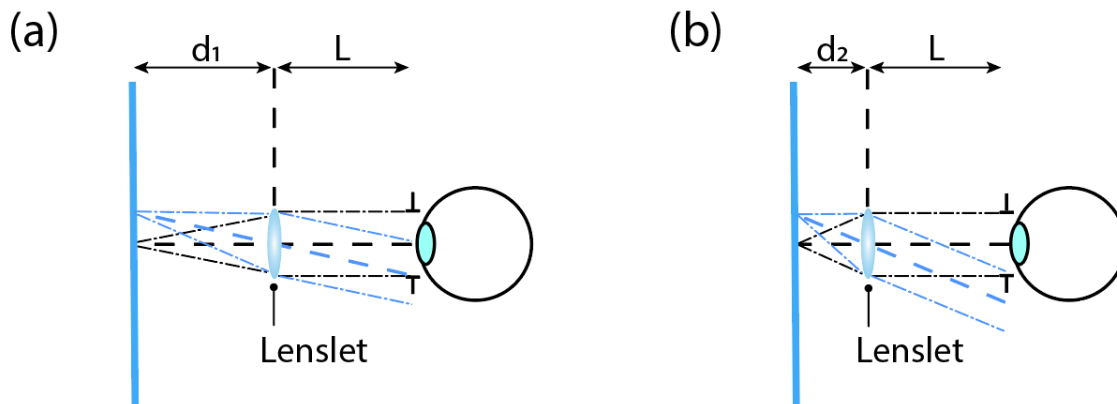


**Figure 4-2: System configuration with (a) 50% vignetting and (b) 100% vignetting.**

To prove concept, in experiment we focus on the central lenslet imaging without considering the deflector array. We constructed two VR systems shown in Fig. 4-2. We used an LCD (Adafruit) as the display panel and two optical lenses with different focal lengths as the central lenslet. The eye relief (L in Fig. 4-2) of the two systems are the same, which is set to be 20 mm. The focal length of the lenslet in Fig. 4-2(a) is 20 mm (Thorlabs, AC080-020-A) and in Fig. 4-2(b) is 10 mm (Thorlabs, AC080-010-A). The aperture of these two lenslets are 8mm. Therefore,

for the same image content from the LCD panel, the image uniformity is expected to be worse for the device configuration in Fig. 4-2(b). It is worth mentioning that although the system in Fig. 4-2(b) looks like it has a larger field of view than Fig. 4-2(a), the peripheral pixels have significant vignetting and cannot be observed by users. This means nearly half of the pixels in Fig. 4-3(b) are "wasted", and the systems in Fig. 4-2(a) and 2(b) have the same "effective FOV" (vignetting less than 50%).

A CMOS (Complementary Metal Oxide Semiconductor) camera (TechnoTeam Vision, LMK6 color, with a colonoscope lens) was used to capture the imaging results of these two systems. The input image is shown in Fig. 4-3(a). Three square dots represent the central and peripheral pixels on the display panel. Fig. 4-3(b) and 3(c) show the imaging results of the VR systems with the 20-mm and 10-mm focal-length lenslet, respectively. In Fig. 4-3(b), we can clearly see three square dots, but in Fig. 4-3(c) we can only see the central dot. For the lenlet with a shorter focal length, its collimated beam has a larger off-axis angle. As a result, the peripheral pixels cannot be captured by the camera lens after propagating through the eye relief distance, as Fig. 4-2(b) depicts. These imaging results indicate that if we shorten the focal length of the lenslet without reconfiguring the system, some peripheral pixels will be lost, and the imaging uniformity will be problematic. On the other hand, the imaging result in Fig. 4-3(b) does not show a significant vignetting. The reason is that the aperture size of the colonoscope lens is only about 2 mm. To prove it, another camera set (Sony α6100 with 2.8/16 lens) with a larger entrance pupil (around 8 mm) was placed in the same system, and the imaging result is presented in Fig. 4-3(d). Although this camera cannot capture focused image because its focal length is too long, the intensity difference between the central dot and the peripheral dots is noticeable, as Fig. 4-3(d) shows.
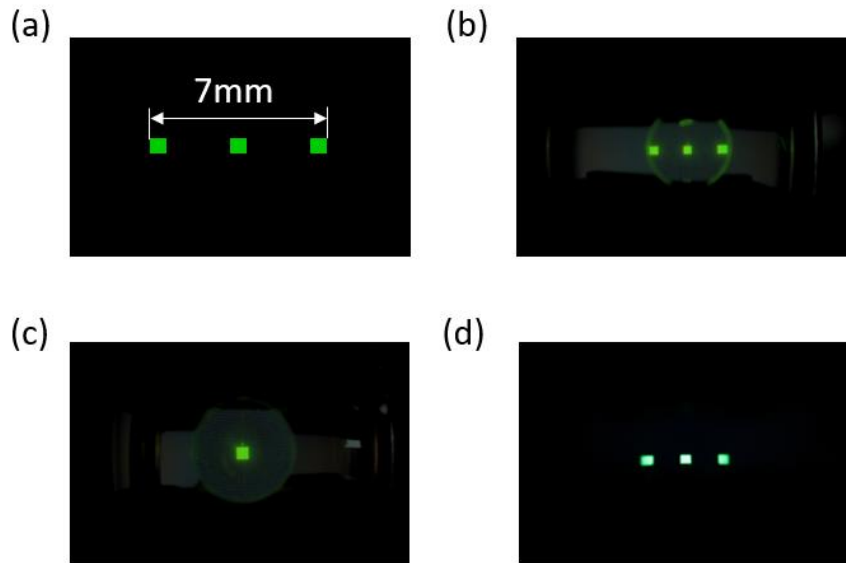
**Figure 4-3: (a) Image of the input signal. Imaging results of the systems with (b) 50% vignetting and (c) 100% vignetting captured by a 2-mm aperture camera. (d) Imaging result of the 50% vignetting system captured by an 8-mm aperture camera.**

To obtain a better vision of the beam intensity distribution, a white screen was placed at the plane of the pupil. The imaging results of the two systems are displayed in Fig. 4-4. From Fig. 4-4, we can clearly see three circles, corresponding to the three collimated beams emitted by the three points on the display, respectively. Fig. 4-4(a) represents the result of the system in Fig. 4-2(a), which has 50% vignetting when the pupil size is 8 mm. After shortening the distance between display and lenslet (Fig. 4-2(b)), the vignetting increases to near 100% (Fig. 4-4(b)). It is noticed that the two side-beam intensities are not uniform in Fig. 4-4(b). The reason is that after shortening the gap between display and lenslet, the off-axis angle is increased for the peripheral points and the lenslet has a thickness around 5 mm (for AC080-010-A), so that some part of the off-axis incidence is blocked by the lateral surface of the lenslet.
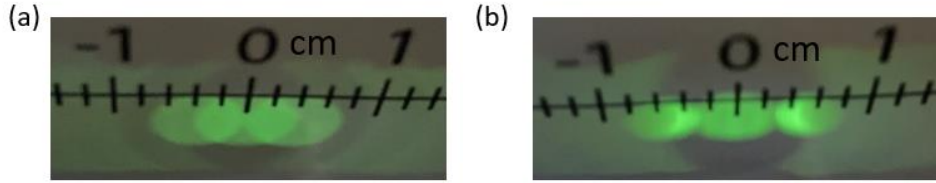
**Figure 4-4: Beam intensity distribution on the plane of pupil for systems with (a) 50% vignetting and (b) 100% vignetting.**

To overcome the increased off-axis angle caused by shortening the distance between display and lenslet, a beam steering process will help mitigate the beam walk-off angle. PB deflector is a polarization dependent device, whose working principle can be explained by following Jones matrix:

$$J'_{\pm} = \frac{1}{\sqrt{2}} \begin{bmatrix} \cos 2\phi & \sin 2\phi \\ \sin 2\phi & -\cos 2\phi \end{bmatrix} \begin{bmatrix} 1 \\ \pm i \end{bmatrix} = \frac{1}{\sqrt{2}} \begin{bmatrix} 1 \\ \mp i \end{bmatrix} e^{\pm 2i\phi} \tag{4-1}$$

According to Eq. (4-1), the output will have an opposite phase change for the LCP and the RCP inputs. Therefore, if the LC directors are patterned with linear change, then this device will work as a PBD, and it will deflect the LCP and RCP inputs to an opposite angle. Based on this property, a PBD can be applied to steer the collimated beams.
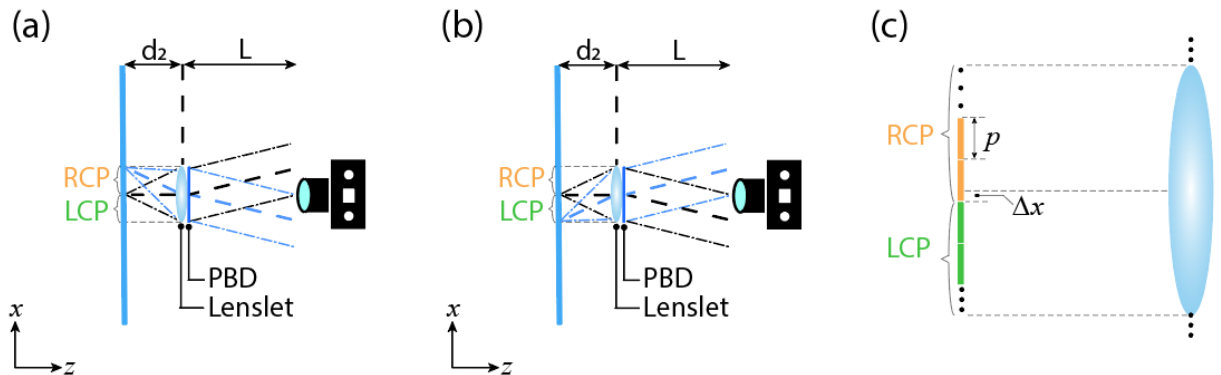


**Figure 4-5: Schematic of system with (a) RCP pixels and (b) LCP pixels imaging. (c) Example of RCP and LCP pixels off-axis arrangement.**

The working principle is illustrated in Fig. 4-5. We can divide the pixels on the display panel into LCP and RCP. Let us assume the collimated beam of RCP pixels is deflected to +x direction, while the collimated beam of LCP pixels is deflected to −x direction. Although the diffraction angle of the PBD is angular dependent, the output angles of the collimated beams can be designed to match each other in Fig. 4-5(a) and 5(b). In so doing, the vignetting can be reduced by 50%. It is worth mentioning that the RCP and LCP pixels should not be completely symmetric along the lenslet optical axis (Fig. 4-5(c)), otherwise these two pixels will correspond to two collimated beams with the same direction, which means the resolution will be sacrificed. In theory, the boundary of LCP and RCP pixels should offset the lenslet optical axis as shown in Fig. 4-5(c), the offset distance should be equal to a quarter pixel pitch. And the imaging content on the display panel should also be modulated because of the interpolation of LCP and RCP pixels. Based on this design, the PBD helps to make better use of the pixels on the display panel and enhance the system angular resolution but keep the system with the same "effective FOV" (vignetting less than 50%) and form factor compared with the system in Fig. 4-2(b).

4.3 Experiments and Results
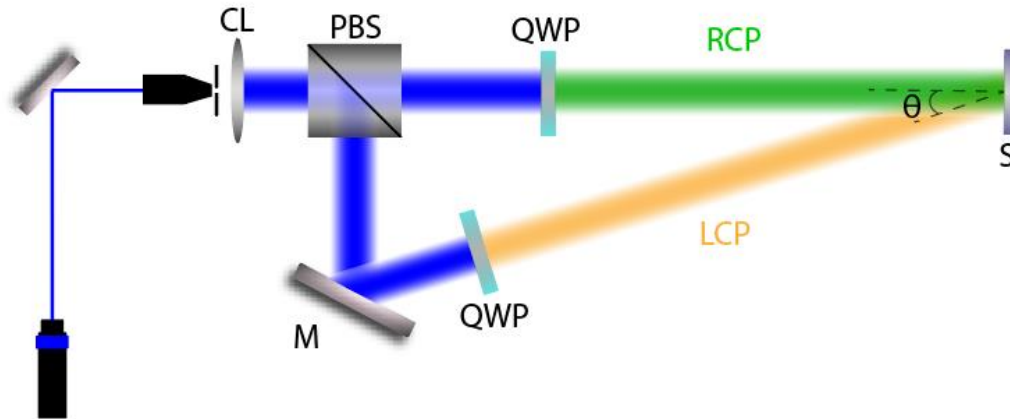


**Figure 4-6: Experimental setup for fabricating Pancharatnam-Berry phase deflector. CL: collimation lens; PBS: polarized beam splitter; M: mirror; QWP: quarter-wave plate; S: sample.**

Before fabricating the PBD, the grating period should be calculated. According to Fig. 4-5(a) and 5(b), the chief ray angle of the edge pixel should be deflected to half, then the grating period of this PBD can be calculated, which is 3.18 μm. Photoalignment method was applied to fabricate this PBD [93,94]. In the beginning, a thin alignment layer (0.2% brilliant yellow dissolved in Dimethyformamide) was spin-coated onto the top surface of a clean glass substrate. Then the substrate was placed in the optical setup shown in Fig. 4-6 for the holography pattern exposure. After the pattern exposure, two layers of reactive mesogen mixture (RMM) were spin-coated onto the substrate. For each layer, a UV lamp was applied to cure the mixture network right after the spin-coating, so that we can obtain a stabilized polymer film. The RMM includes 96% reactive mesogen RM257 (from LC Matter), 3.9% photo-initiator Irgacure 651 (from BASF), and 0.1% surfactant Zonyl 8857A (from DuPont). This RMM was dissolved in toluene, and the ratio of solute to solvent was 1:5. The fabricated sample was shown in Fig. 4-7(a), and it was imaging

a keyboard. The two ± 1$^{st}$ order diffracted lights can be observed, because the unpolarized ambient light contains both LCP and RCP components. Fig. 4-7(b) is the imaging results of the sample by a polarization microscope (Olympus BX51). The grating structure is clear, and the grating period is 3.11 μm according to the measurement. The thickness of the PBD has been optimized for operating wavelength (532nm), and the 1$^{st}$ order diffraction efficiency of the PBD can reach 99% at 532nm after measurement.
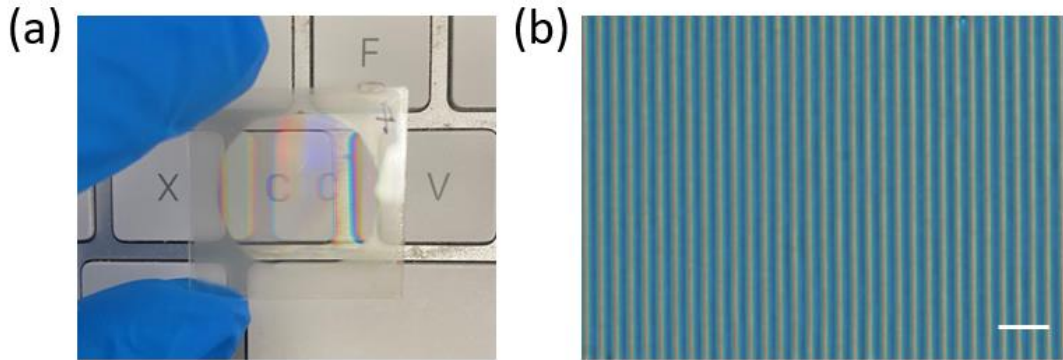


**Figure 4-7: (a) Photo of the fabricated PBD sample, and (b) polarizing microscope photo of the sample. Scale bar in the picture is 10 μm.**
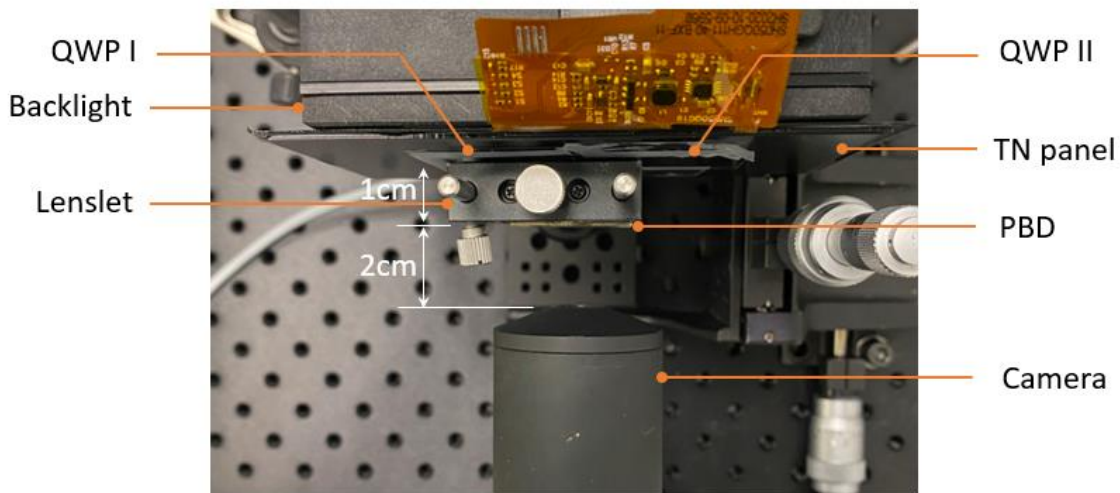


**Figure 4-8: Photo (top view) of the optical system setup.**

We inserted the fabricated PBD into the system as shown in Fig. 4-8. The light engine consists of a backlight and a 90° twisted nematic (TN) panel [95]. The output from the TN panel is a linearly polarized light oriented at 45°. We also placed two orthogonal quarter-wave plates (QWP I and QWP II in Fig. 4-8) side-by-side on the surface of the TN panel, so that the output beam will be converted to LCP and RCP, respectively. The PBD was in close contact with the lenslet back surface and the distance from the TN panel to PBD is around 1 cm. The eye relief is 2 cm. Following the similar process mentioned previous section (Fig. 4-3 and Fig. 4-4), we applied the input images shown in Fig. 4-3(a) to the system. The imaging results are presented in Fig. 4-9. Fig. 4-9(a) shows the captured photo at the pupil plane. Because the employed light engine in the system has a broad spectrum, the output contains some red component even if the input signal is green. To narrow down the spectral bandwidth, a green color filter whose central wavelength is 532 nm was placed between the PBD and camera. According to the result, the images of the peripheral dots can also be captured by the camera, after the collimated beams are deflected by the PBD. The central square dot is split into two parts and merged into the two peripheries, respectively. The beam intensity distribution is shown in Fig. 4-9(b). The collimated beam of the central square dot is also split into two parts with equal intensity and merged to the two peripheral dots.
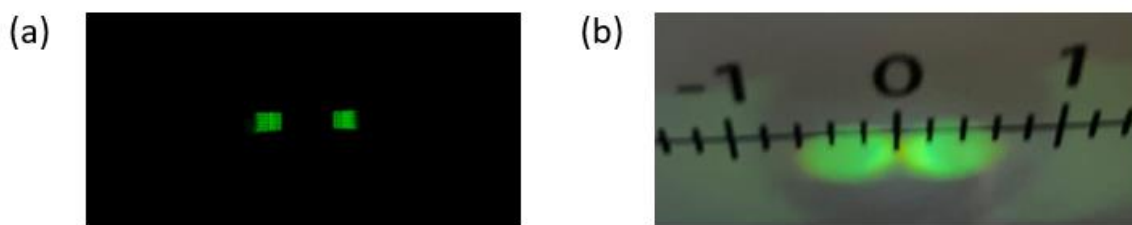


**Figure 4-9: (a) Imaging result and (b) intensity distribution at pupil plane of the ultra-compact VR system with a PBD.**

The operation principle of applying a PBD to shorten the distance between the light engine and the lenslet has been illustrated in Fig. 4-2 and Fig. 4-5 with confirming experimental results shown in Fig. 4-3 and Fig. 4-9. To demonstrate feasibility of the proposed system for a VR display, we use green color ABCD letters (Fig. 4-10(a)) as the input, and the imaging results are shown in Fig. 4-10(b). In our design, the pixels on the left half and right half emit LCP and RCP light, respectively. That means, in Fig. 4-10(a) and 10(b), letters A and B are LCP and letters C and D are RCP. Then the collimated beams corresponding to A and B will be deflected towards $-x$ direction and the collimated beams corresponding to C and D will be deflected towards $+x$ direction. Therefore, in the imaging result shown in Fig. 4-10(b), the letters A and B are overlapped with C and D, respectively. Next, we rendered the input signal to make the output as the desired imaging content, ABCD. Based on the system principle, we divided the pixels in Fig. 4-10(a) (pixels in the white box) into odd and even columns. The odd column pixels are joined together to form the left half of the signal in Fig. 4-10(c), and the even column pixels form the right half. The rendered picture is shown in Fig. 4-10(c). Each character is split into two parts with LCP and RCP pixels. The imaging optics will interpolate these two parts together and the result is depicted in Fig. 4-10(d). According to the results, letters B and C are well reproduced, but A and D are not. This is because the LCP A on the left and RCP D on the right are not deflected with a large enough angle after PBD, so that they are not well interpolated to the RCP A and LCP D, respectively. This problem originates from the angular response of PBD and lenslet aberration, which will be discussed in details in later section. On the other hand, the LCP A and RCP D on the two sides hit the edge of the lenslet so that the aberration is significant. To improve the rendering result, we shorten the distance between the LCP A and B, and the distance between the RCP D and C, which

is shown in Fig. 4-10(e). In this way, it can correct the deflection angle of the LCP A and RCP D and reduce the aberration. The improved result is depicted in Fig. 4-10(f). All the characters are well reproduced and the feasibility of the proposed ultracompact VR system with a PBD is demonstrated. In the experimental results, the rasterized pattern can be observed. This is because the resolution of the display panel (5.0" 800*400 from Adafruit) is low. If the system applied a high-resolution display panel, this pattern can be eliminated.
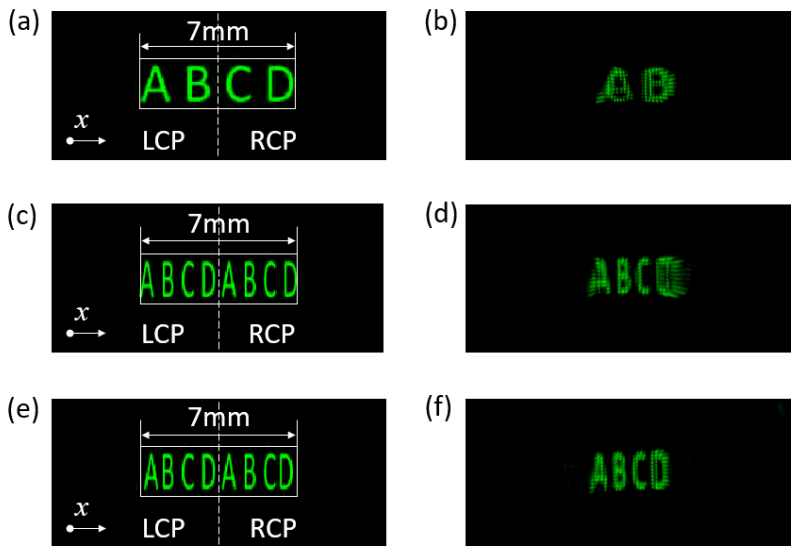


**Figure 4-10**: (a), (c), (e) Input image contents during the rendering and (b), (d), (f) the corresponding imaging results.

What's more, we also simulated the system using Zemax. A user defined PB optical element was inserted in the system. A home-made DLL file was also generated with rigorous coupled-wave analysis (RCWA). Results are shown in Fig. 4-11. The input signal is shown in Fig. 4-11(a), and the output image and intensity distribution are shown in Fig. 4-11(b) and 11(c), respectively. The simulation results agree with experiment very well.
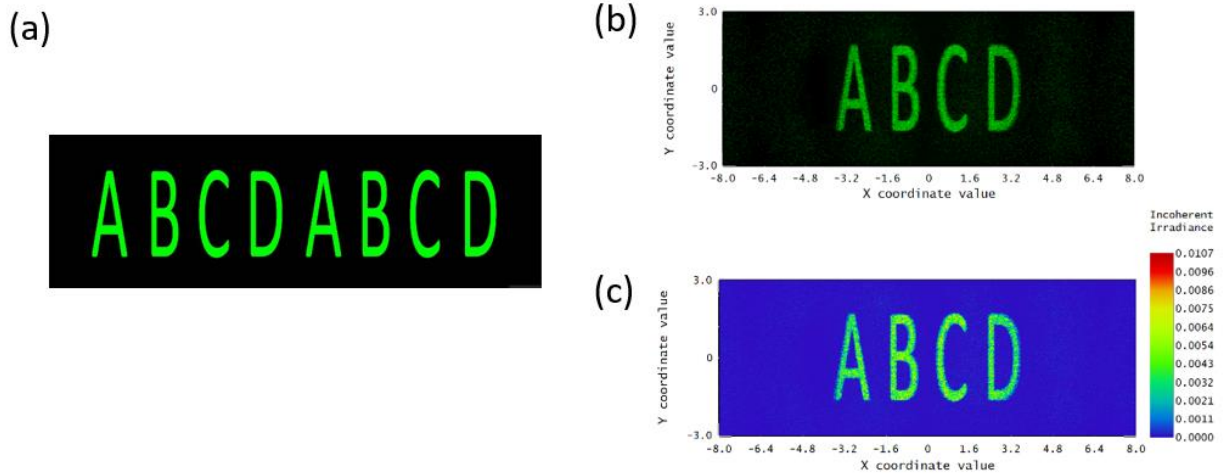
**Figure 4-11: Simulation (a) input signal, (b) output image and (c) intensity distribution in Zemax.**

In addition, another key component, deflector array, is also designed in this work. Since the simulation of PBD is time consuming in Zemax, the model of PBD was removed from the system during the deflector array design. However, the input for the deflector array can be the same, as indicated in Fig. 4-12, allowing for a significantly faster simulation process.
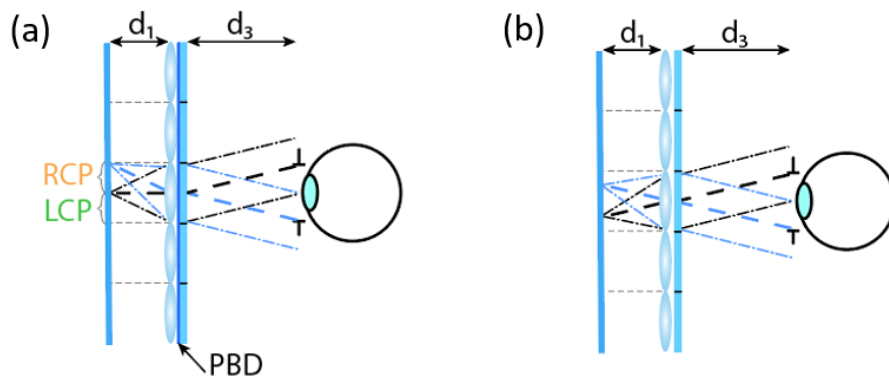


**Figure 4-12: Optical system structures (a) with and (b) without PBD for simulation.**

In the simulation of deflector array, the micro prism structure was adopted, as Fig. 4-13(a) shows. The problem needs to be considered is the side wall reflection, which will deflect the light

into the opposite direction, then the output will become stray light. This also makes the output of deflector arrays nonuniform because the intensity of this part of light is influenced by the tilt angle of the prisms. Another factor guiding the deflector design is the field of view stitching, which is the condition shown in Fig. 4-13(b). The green beam is required to have the same output angle as the blue beam, otherwise, there would be a field of view gap or overlap. The design target is to make the section of each domain can be well connected to its neighbors, as shown in Fig. 4-13(b).
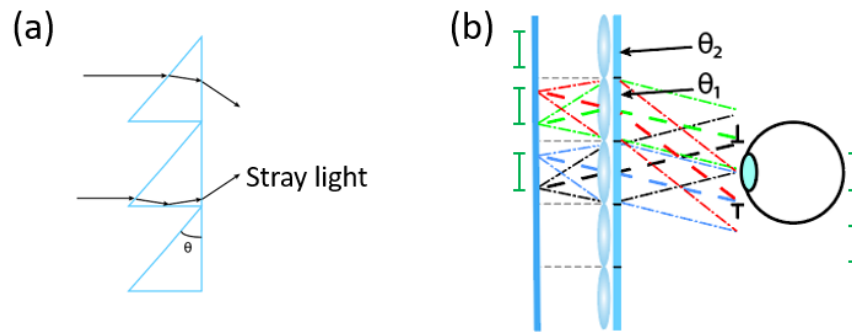


**Figure 4-13: (a) micro prism structure, (b) field of stitching condition.**

The deflector array simulation results are presented in Fig. 4-14. In the simulation, we study the influence of the refractive index. According to the calculation, higher refraction index contributes to a larger field of view, but the image will be more nonuniform. The image outputs with refractive index of 1.5 and 1.8 are shown in Fig. 4-15. From these results, the refractive index of 1.8 produces a larger field of view, but the resulting vignetting and distortion are too significant. This is not helpful for the imaging. Therefore, a lower refractive index is better for this application. Moreover, when the refractive index is 1.5, the imaging non-uniformity can be compensated by adjusting the display panel backlight, as illustrated in Fig. 4-15(c).
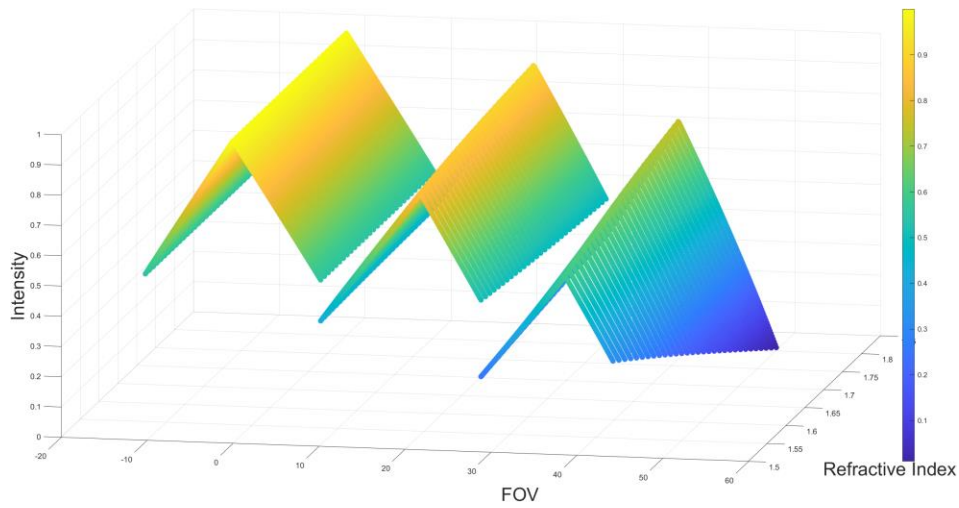
**Figure 4-14: Simulation results of deflector array.**
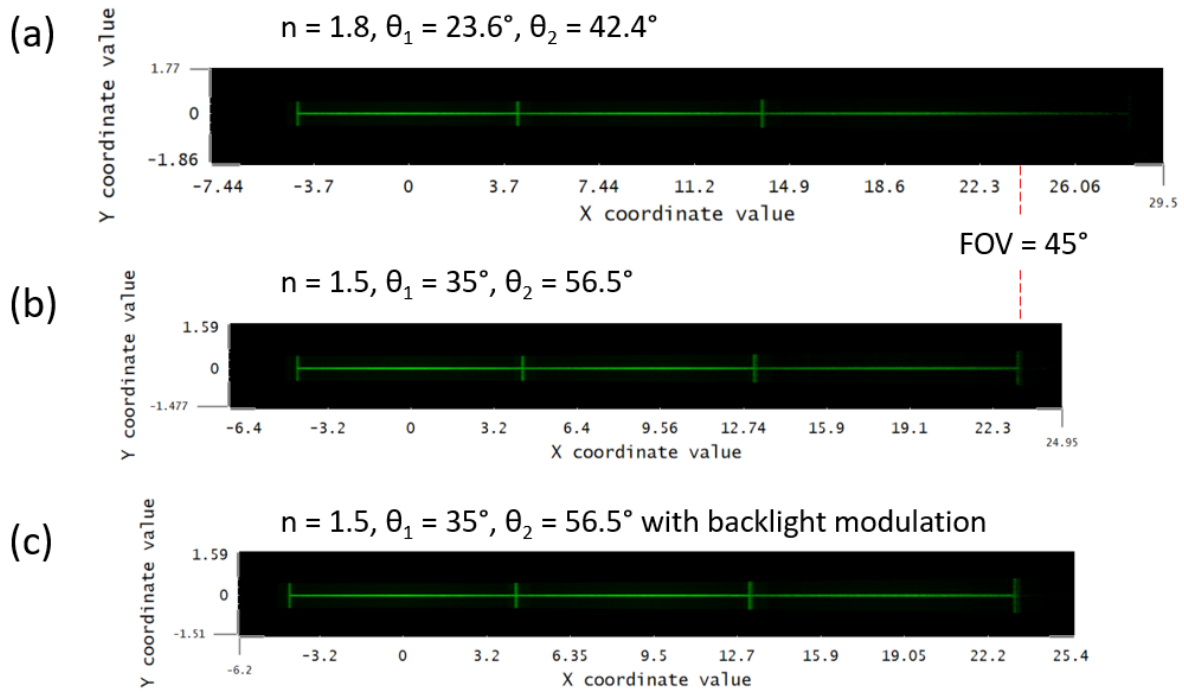


**Figure 4-15: Output results of field of view stitching with the deflector array refractive index of (a) 1.8, (b) 1.5, and (c) 1.5 with backlight modulation.**

## 4.4 Discussion

During the rendering process, we notice that the deflection angles of the characters are slightly different, which will cause some characters not interpolating well, just like the condition shown in Fig. 4-10(d). This is because the deflection angle of PBD is dependent on the incident angle. We measured and calculated the deflection angles of the applied PBD with different input angles, and results are shown in Fig. 4-16(a). At normal incidence, the deflection angle is around 9.8°; but as the input angle increases to 20°, the deflection angle shifts to 10.9°. It is easy to see that the deflection angle increasing with the incident angle, which means the characters on the margin will be over-deflected. However, according to the result in Fig. 4-10(d), the LCP A and RCP D are under-deflected. To find out the reason, the lenslet imaging profile is plotted by Zemax as Fig. 4-16(b) shows. The marginal ray of the boundary pixels, whose off-axis distance is 3.5 mm, will be bent with a larger angle than the chief ray, because of the lenslet aberration. In Fig. 4-16(b), the output angle of the chief ray is 19°, but the marginal ray output angle is as large as 25°, and for the boundary pixels, the marginal rays dominate the energy going through the eye pupil. It explains why the PBD under-deflects the margin characters even if they have larger deflection angles.
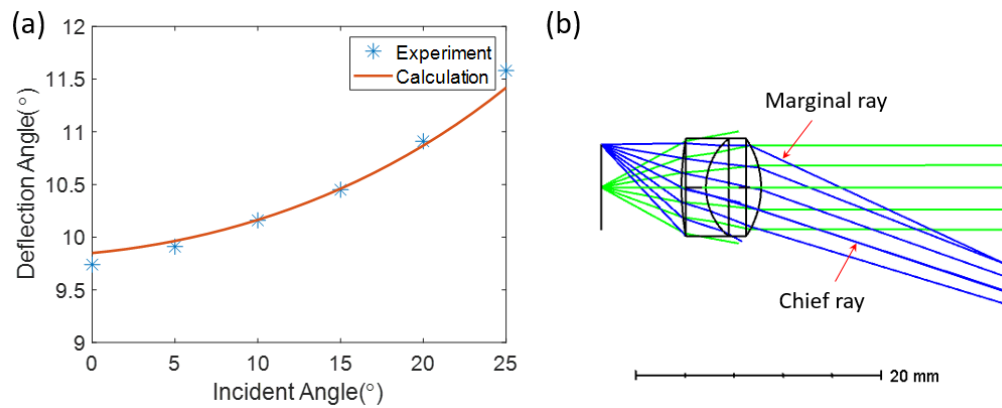


**Figure 4-16: (a) Angular response of the fabricated PBD and (b) imaging profile of the lenslet in Zemax.**

In experiment, we notice that the boundary pixels suffer from significant aberration. Even if we can customize the lenslet array performance to minimize the aberration in the future, this problem cannot be eliminated completely. Therefore, the boundary pixels will be sacrificed. One solution is to segment the display panel to different sub-panels corresponding to each lenslet, as Fig. 4-17 shows. In this way, the resolution of the sub-panels might be varied, so that a foveated display system can be designed. As indicated in Fig. 4-17, the central sub-panel covers the foveated region and requires a high-resolution panel. Medium resolution sub-panels surround the central sub-panel and perform as the transition area from high resolution to low resolution. The peripheral region is covered by low resolution sub-panels.
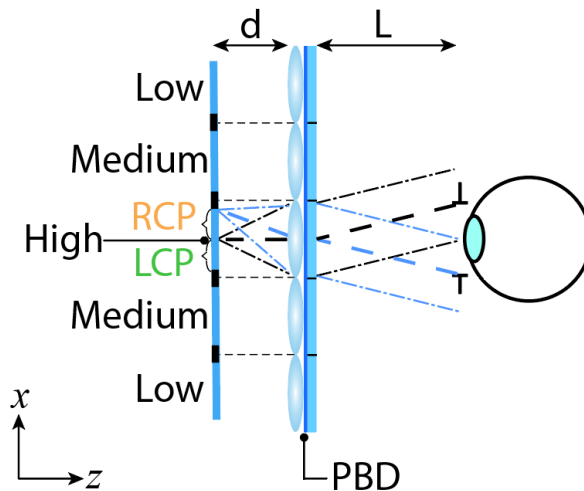


**Figure 4-17: Schematic of the foveated ultra-compact VR system.**

For full color performance, the PBD can be fabricated with dual-twist or multi-twist structure [25,47] to achieve high diffraction efficiency at primary RGB wavelengths. However, the diffraction angles for different color input will not be the same. Therefore, when the input signal contains multiple colors, the signal of each color should be rendered individually.

On the other hand, the imaging content in Fig. 4-10 mainly expands in X direction. If the image further extends along Y direction, then the vignetting will also appear. This approach can be extended to two dimensions. In Y direction, the same process can be applied, but it requires active wave plates to modulate the polarization states of the pixels, and the system needs time-multiplexing, which is shown in Fig. 4-18(a). Another method is to reduce the pixels in Y direction, as depicted in Fig. 4-18(b), because the human eye has a smaller FOV in the vertical direction than that in the horizontal direction.
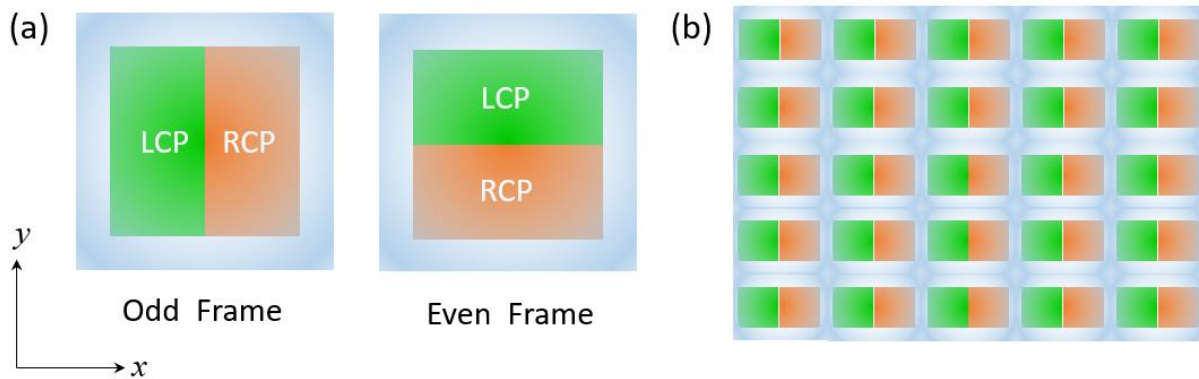


**Figure 4-18. Two methods for two-dimensional operation: (a) active waveplate with time multiplexing; (b) reducing the number of pixels in Y direction.**

## 4.5 Summary

We proposed an ultracompact VR system, whose imaging optics consisting of a lenslet array, a deflector array, and a PBD. The lenslet array aims to collect the light emitted from the display panel while the deflector array functions to bend the beams toward the eyebox. We have experimentally demonstrated that the PBD plays a key role in the polarization interpolation, which helps to reduce the system vignetting. The fabricated PBD is a thin polymer film and can be directly laminated to the lenslet without increasing the system's form factor and weight noticeably. The system has a total thickness around 1 cm with 8mm eyebox (50% vignetting) and 20mm eye

relief. Image rendering and angular calibration process are also proven. Ray tracing model established using Zemax. The simulation results agree with the experiment very well. The deflector array also be designed. The proposed ultracompact VR structure can significantly reduce the system form factor, and its widespread applications for VR systems are foreseeable.

# CHAPTER 5: COMPACT AND HIGH OPTICAL EFFICIENCY AR SYSTEM

The content of this chapter was previously published in [14].

## 5.1 Background
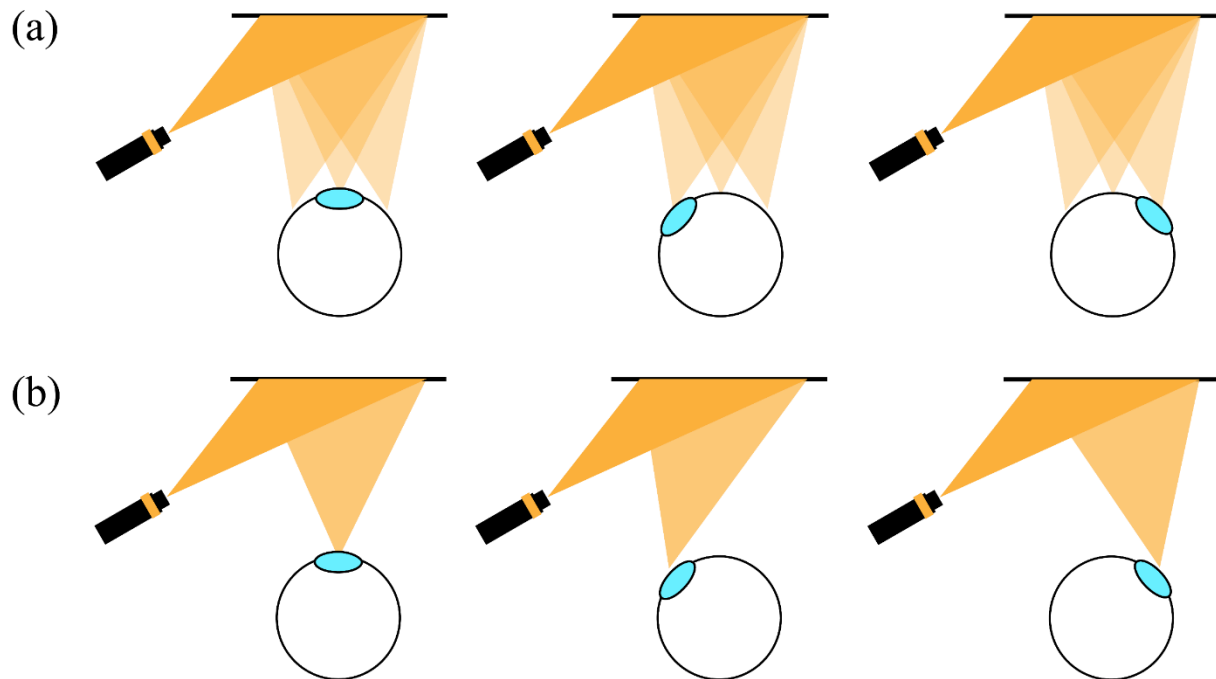


**Figure 5-1: Illustrations of Maxwellian-view system based on (a) pupil duplication and (b) pupil steering.**

Currently, many of the AR products apply the waveguide optical structure, such as HoloLens 2 and Magic Leap 1. The benefit of light guide is that it breaks the limitation of the etendue conservation[96], and it can achieve a large eyebox. However, the eyebox size is a trade-off to optical efficiency. On the other hand, the couplers on the waveguide also introduce the optical efficiency losing. "Maxwellian-View" structure is regarded as the retinal projection type display system, which can achieve 100% optical efficiency in theory, because all the light will

enter the pupil according to the design. While the shortage of the Maxwellian-view structure is also obvious, which is the small eyebox. Therefore, the question on how to enhance the optical efficiency in an AR system converses to how to extend the eyebox of the Maxwellian-view AR system. To enlarge the eyebox of a Maxwellian-view display, two major approaches have been developed: pupil duplication (Fig. 5-1(a)) [97–100] and pupil steering (Fig. 5-1(b)) [35,101].
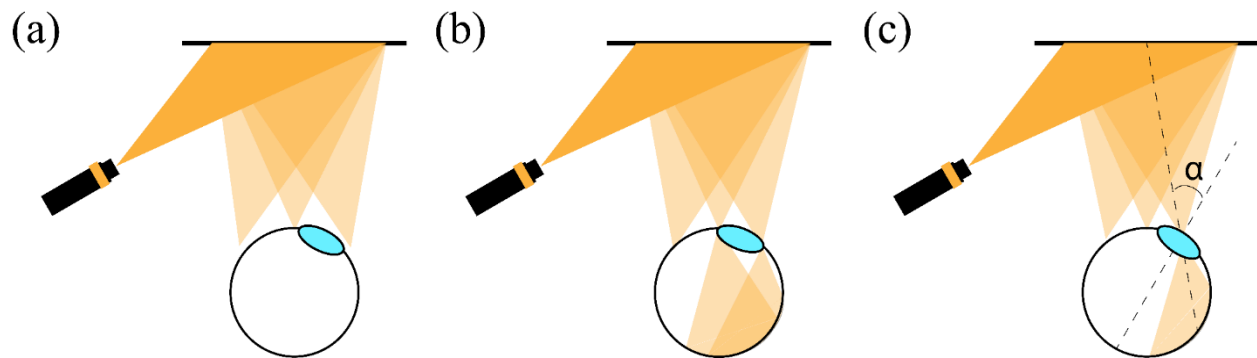


**Figure 5-2: Problems exist in the pupil duplication: the distance between two viewpoints is (a) too large and (b) too small; (c) mismatch between the viewing direction (eye gaze) and chief ray.**

As Fig. 5-1(a) depicts, pupil duplication methods usually utilize a HOE [97,98], beam splitter array [99], or SLM [100] to split the collimated beam into multiple directions, so that each direction corresponds to one viewing point. This approach is cost effective because no additional eye-tracking system is needed, but it will introduce some problems. The major one is that the space gap between different viewing points could be too large (Fig. 5-2(a)) or too small (Fig. 5-2(b)). When this happens, the user either cannot see any image or will see two partial/ghost images when their eyeballs rotate to the middle of two adjacent viewing points. Such a problem arises because all the viewing points appear simultaneously. Another problem, as Fig. 5-2(c) depicts, is that the direction of chief ray does not match the user's viewing direction (eye gaze) except for the central viewing point. This gaze mismatch will let the user see unnatural image and get a terrible viewing

experience at these viewing points [102,103]. The third drawback of pupil duplication is that the optical efficiency will drop to 1/N when N viewing points are presented (e.g., N=3 in Fig. 5-2), because only one viewing point is used at a time.

On the other hand, the pupil steering method can eliminate the first and third shortcomings mentioned above because there is only one viewing point presented. However, to accommodate eye rotation, an eye tracking and a beam steering device are required for the pupil steering system. Moreover, a conventional lens coupler can achieve diffraction limit only at one incident angle. Once the input beam is modulated toward various directions, the imaging quality at some viewing points will drop significantly [35]. Meanwhile, the mismatch between chief ray and eye gaze still exists in the pupil steering system. One solution to correct such a mismatch is to shift the position of lens coupler, but it requires a mechanical shifting part, which will increase the complexity and weight of the system [101]. Therefore, there is an urgent need to develop a Maxwellian-view AR system with expanded eyebox, good imaging quality, natural viewing experience, high optical efficiency, and high ambient contrast ratio, while keeping the system simple, compact, and lightweight.

5.2 System Configuration- Gaze Matched Pupil Steering Maxwellian-view AR System

The operation principle of the AR system we proposed is shown in Fig. 5-3. A laser projector is used as the light engine. The projected beam passes through a circular polarizer (CP) and a collimation lens (CL) before reaching the optical combiner. Thus, the input image is either LCP/RCP light. The optical combiner (OC) consists of two laminated off-axis CLC lens arrays. The chirality of these two CLC lenses is opposite. Let us assume the first layer (brown color)

works for LCP, and the second layer (green color) works for RCP. The second lens has a slightly longer focus to accommodate its slightly longer optical path. The location of each off-axis lens is specially designed so that the chief ray matches with the user's gaze. In Fig. 5-3, $D$ is the average diameter of an adult's eye ball, which is 2.4 cm; L is the eye relief; $\theta$ is the off-axis angle of the CLC lens which is designed to be 60°, so that the input beam to the optical combiner will not be blocked by the eyeball; $d$ is the lens diameter, and $\varphi$ is the eyeball rotation angle when the user sees the other viewing point shown in Fig. 5-3(b). The input light can be selectively diffracted by a specific lens. Each lens corresponds to one viewing point, whose incident angle and optical path are fixed. The wavefront of each diffractive liquid crystal lens is recorded independently and can be designed to minimize the optical aberrations.
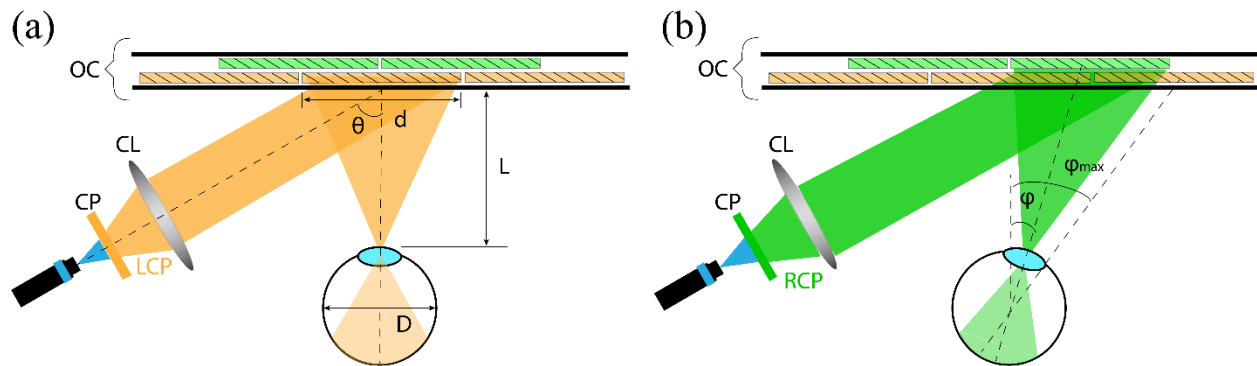


**Figure 5-3: System configuration of the proposed pupil steering AR system with (a) LCP input and (b) RCP input.**

When the viewer sees the object at normal angle, there is a maximum eyeball rotation angle ($\varphi_{max}$ in Fig. 5-3(b)), which means that once the object position is outlying the FOV of $\pm\varphi_{max}$, the viewer tends to rotate head instead of rotating eyeball to continue gazing at the object. When designing the system, we set $\varphi_{max} = 30°$, and there are five viewing points in one dimension. Then, we can plot the relationship between eye relief $L$ and central FOV or lens diameter $d$, as shown in

Fig. 5-4. From the figure, the following tendency is found: the shorter the eye relief, the wider the FOV. In order to obtain a relatively large FOV and reasonable eye relief, we choose the eye relief to be 15 mm. Under such condition, the corresponding central FOV is about 55° and the lens diameter is 15.6 mm. The *f*-number of the central off-axis CLC lens is 0.96.
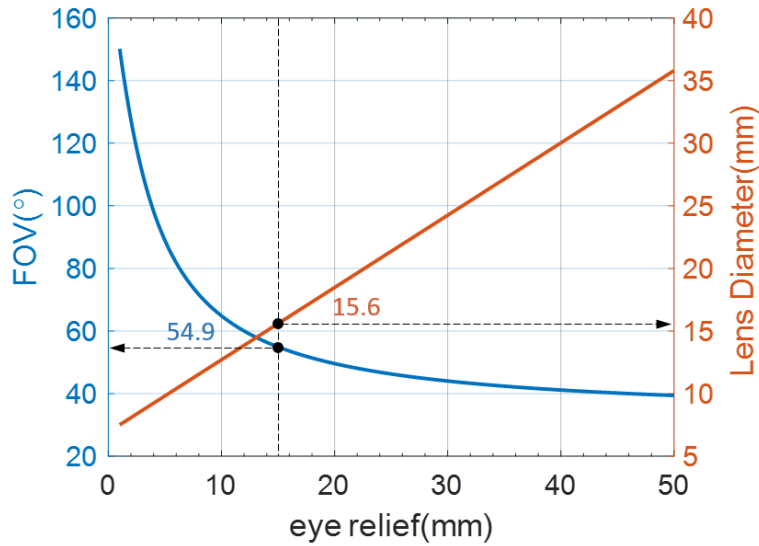


**Figure 5-4: Relationship between eye relief and central FOV or lens diameter.**

We have simulated the proposed system in the LightTools as Fig. 5-5(a) depicts. In the simulation, we simplify the human eye as a sphere receiver (retina) and an ideal lens (pupil lens). The optical combiner consists of three reflective off-axis lenses. The off-axis angle is 60°, 44° and 76°, which corresponds to 0°, +16° and −16° gaze direction, respectively. Since we apply an ideal lens in the optical combiner, whose focal plane is an ideal plane, even when the beam has a large incident angle. Therefore, we can see that the effective focal length of the ideal lens is angle dependent. If we set the focal length of the ideal lens as *f*, then the focal length is 2*f* when the incident angle is 60°, and the effective focal length of the reflective off-axis lens is $1/(\frac{1}{2f} + \frac{1}{f}) =$ $\frac{2}{3}f$. Since the eye relief of the system is set at 15 mm, the effective focal length of the central off-

axis lens should be 15 mm and the focal length of the ideal lens is set at 22.5 mm in the simulation.

The other two off-axis lenses on the combiner should have a little bit different effective focal

length, 16.09 mm, which can be easily calculated by the geometric relationship. In figure 5a, the

red line indicates the gaze direction and the red point on the retina is the "gaze point", which

always locates at the center of the retina, no matter where the gazing direction is. Fig. 5-5b to 5d

are the simulation results of the signal intensity distribution on the retina, when the gaze direction

is −16°, 0°, and +16°, respectively. We can see that the center of the FOV always match with the

"gaze point", which means the imaging content is located at the center of retina, and the observer

will have a natural viewing experience. These results also prove the feasibility of the proposed
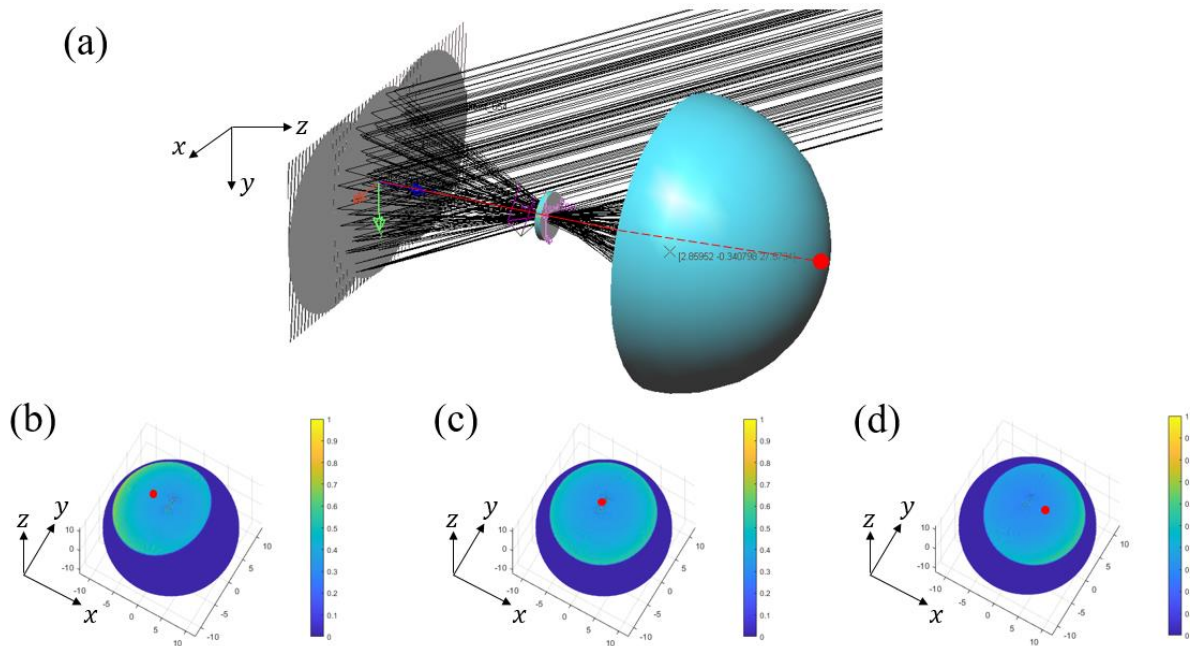
system.



**Figure 5-5: System simulation with LightTools (a) system profile, (b)-(d) simulation results of the signal intensity distribution on the retina with the "gaze point" (red point), when the gaze direction is −16°, 0°, and +16°, respectively.**

## 5.3 Large Angle Diffractive Liquid Crystal Lenses

The optical combiner in the proposed system is a two-layer polarization selective off-axis CLC lens. The first layer diffracts LCP light and the second layer diffracts RCP. The structure of this off-axis CLC lens is a lens-patterned reflective polarization volume grating (rPVG). Photo-alignment method was adopted in the lens fabrication. A thin photo-alignment layer was spin-coated on a clean glass substrate. Then the substrate was exposed in the setup shown in Fig. 5-6. In the figure, a collimated laser beam with wavelength λ=457nm is split into two beams by a polarizing beam splitter. After being reflected by the mirrors, the two linearly polarized beams are converted to LCP and RCP, respectively, by the quarter-wave plate in each arm. The LCP beam works as the reference beam and the RCP signal beam passes through a template lens, so that the lens profile is recorded on the substrate. On the other hand, due to the linear optical path difference between the two beams, a grating pattern is coexistent. The reference beam angle $\theta_1$ is equal to the off-axis angle $\theta$ shown in Fig. 5-3(a), and its value is the same for all the lenses on the optical combiner, because the input laser beams are collimated. However, the signal beam angle $\theta_2$, which equals to the eye rotation angle $\varphi$ in Fig. 5-3(b), varies for each different lens on the optical combiner, since each lens corresponds to a unique viewing direction. Due to limited facility in our lab, we can only build two sets of the optical path as depicted in Fig. 5-6, and we are unable to fabricate more than two off-axis CLC lenses with different lens profiles in one substrate. Therefore, we only retain the central lens in the first substrate working for LCP, and the second substrate has two off-axis CLC lenses working for RCP. There are three viewing points in total in our demonstration. Based on the designed eye relief and lens diameter, the viewing direction ($\varphi$ in Fig. 5-3(b)) corresponding to the two lenses on the second substrate is +16° and −16°, respectively.

That is to say, the value of $\theta_2$ should be $+16°$ and $-16°$ when fabricating these two lenses. On the other hand, it is easy to see that $\theta_2$ should equal to $0°$ for the central lens on the first substrate.
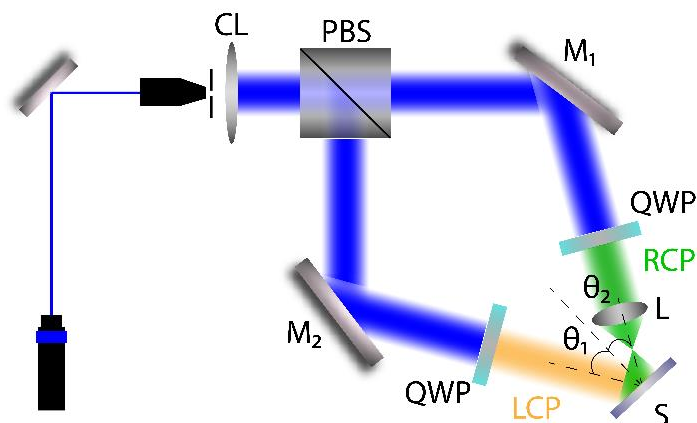


**Figure 5-6: Experimental setup for holographic off-axis lens pattern exposure.**

**Table 5-1: Recipes of the materials and spin-costing speed in the device fabrication.**

| Solution | Solute | Solvent | Solute: Solvent | Coating Speed |
|---|---|---|---|---|
| Alignment layer | Brilliant yellow | Dimethyformamide (DMF) | ≈1:500 | 500 (10s) + 3000 (30s) |
| RM layer | Zonyl 8857A (0.05%) RM257 (94%) S5011/R5011 (2.66%) Irg651 (3.29%) | Toluene | ≈1:2.1 | 2000 (30s) |

After pattern exposure, a RMM solution was spin-coated onto the substrate. The material recipe is listed in Table 5-1. The components and their ratios in the RMM solution for two substrates are the same, except for the chiral dopant. The chiral dopant for the first substrate is

63

S5011, which is left-handed, while the second substrate is R5011, which is right-handed. It is worth mentioning that when the substrates were exposed to the same pattern, chiral dopants with opposite charity will lead to an opposite diffraction angle as Fig. 5-7 depicts. If we want the two substrates to have the same diffraction angle for LCP and RCP, respectively, we can flip top to bottom and rotate 180° horizontally for one of them as shown in Fig. 5-7.
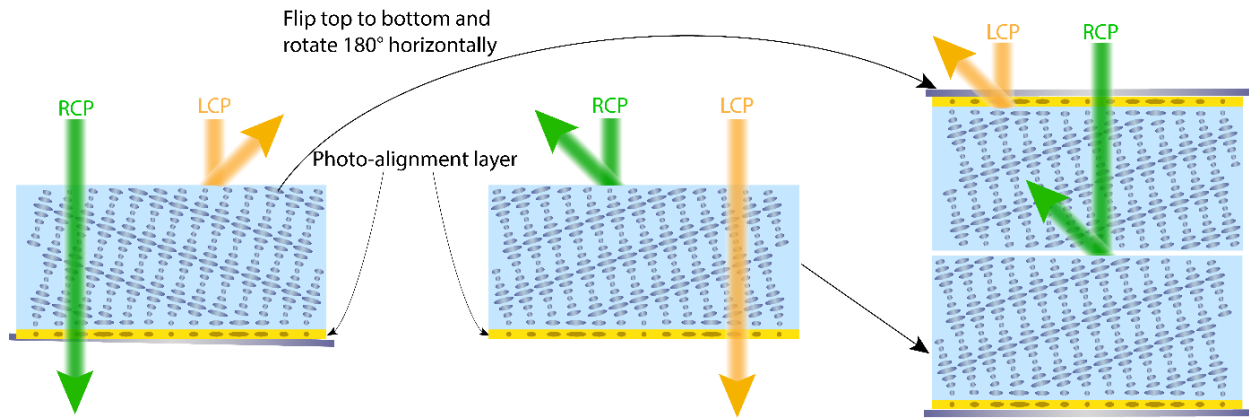


**Figure 5-7: Schematics of holography cholesteric liquid crystal optical elements with the same exposure pattern, but opposite charity.**

Due to the large off-axis angle and small *f*-number, the grating period will be small. For example, when the signal beam is at +16°, the angle between signal and reference beams should be $\theta_1 + \theta_2 = 60° + 16° = 76°$ for the central point, which is shown in Fig. 5-8(a). However, for the marginal points on the right, the angle will be larger, and $\theta_3 = 76° + FOV/2 = 101°$ (the FOV is around 50° when φ=±16°). The corresponding grating period is 300 nm. Such a small grating period is challenging to fabricate. We measured the intensity distribution along horizontal and vertical directions, and results are plotted in Fig. 5-8(b) and 8(c) (this intensity has taken Fresnel reflection at the glass-air interface into account). The data points (dots) are fitted by Gaussian function (lines). In the *x* direction, we shift the peak intensity a little to the left from the center of the template lens L, so that the intensity mismatch between reference beam and signal

beam in the small period area (the right side of the sample) is smaller, which is helpful for the

pattern alignment. In experiment, we also found that a smaller grating period requires a higher

intensity during pattern exposure. Fig. 5-8(d) to 8(f) show the photos of samples fabricated with

30s exposure time but different intensities during the pattern exposure. From the photos, as the

laser output power decreases, the unaligned area on the right-side increases, but the left-side is still

well aligned, because the grating period gets larger from right to left. Moreover, in order to

eliminate the influence of exposure dosage, we add another control group with 150mW laser output

power but an exposure time of 40s, so that the samples in Fig. 5-8(d) and 8(g) have the same

exposure dosage. However, the performance of the sample in Fig. 5-8(g) is similar to that in Fig.

5-8(f). Therefore, the exposure dosage is not a key factor in making this large off-axis low *f*-

number CLC lens, but the exposure intensity is.
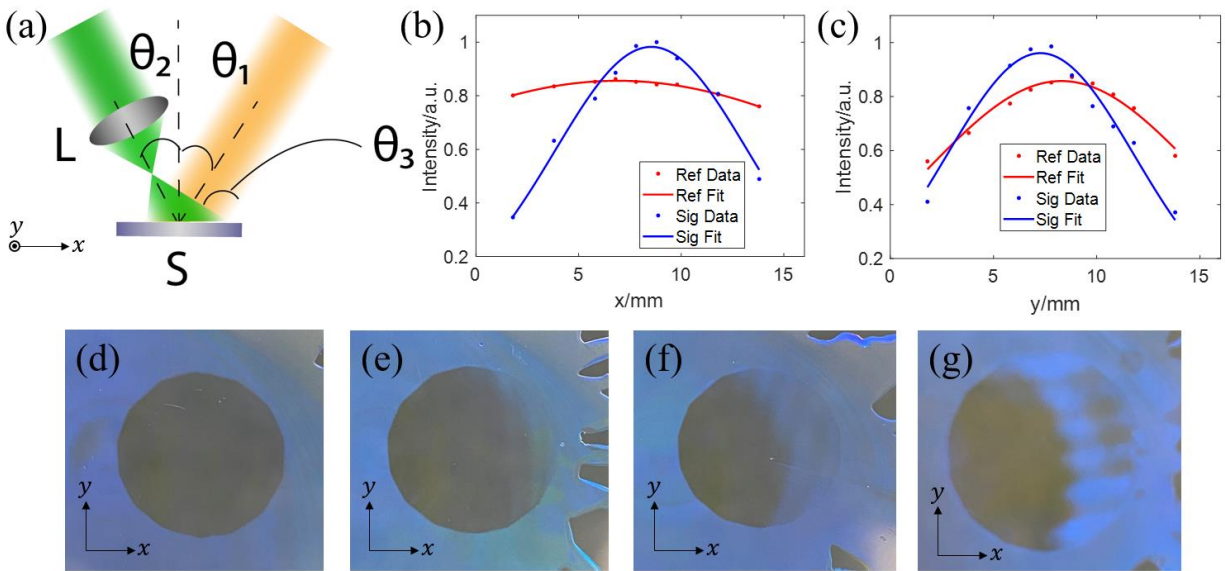


**Figure 5-8: (a) Schematic of the angle between reference beam and signal beam during pattern exposure. Intensity distribution along (b) horizontal and (c) vertical direction. Photos of fabricated samples with 30s exposure time, but different laser output power (d) 200mW, (e) 175mW, (f) 150mW during pattern exposure. (g) A photo of fabricated sample with 40s exposure time and 150mW laser output power during pattern exposure.**

Fig. 5-9(a) and 9(b) show the photos of our fabricated samples. The first sample works for LCP, which serves as the central viewing lens. The second sample diffracts RCP and contains two off-axis lenses, corresponding to $+16°$ and $-16°$ viewing directions, respectively. Fig. 5-9(c) shows the transmission spectra of these two samples with the specified circularly polarized beams, and the incident angle is $60°$, which is the same as the condition when they are applied as the optical combiner in the proposed system. The spectrums were measured by a white light spectrometer (Ocean Optics HG2000CG) with a halogen lamp and normalized with a clean glass substrate. The diffraction efficiency of these two samples is 98% and 91%, respectively, at the target operation wavelength (457nm), according to Fig. 5-9(c).
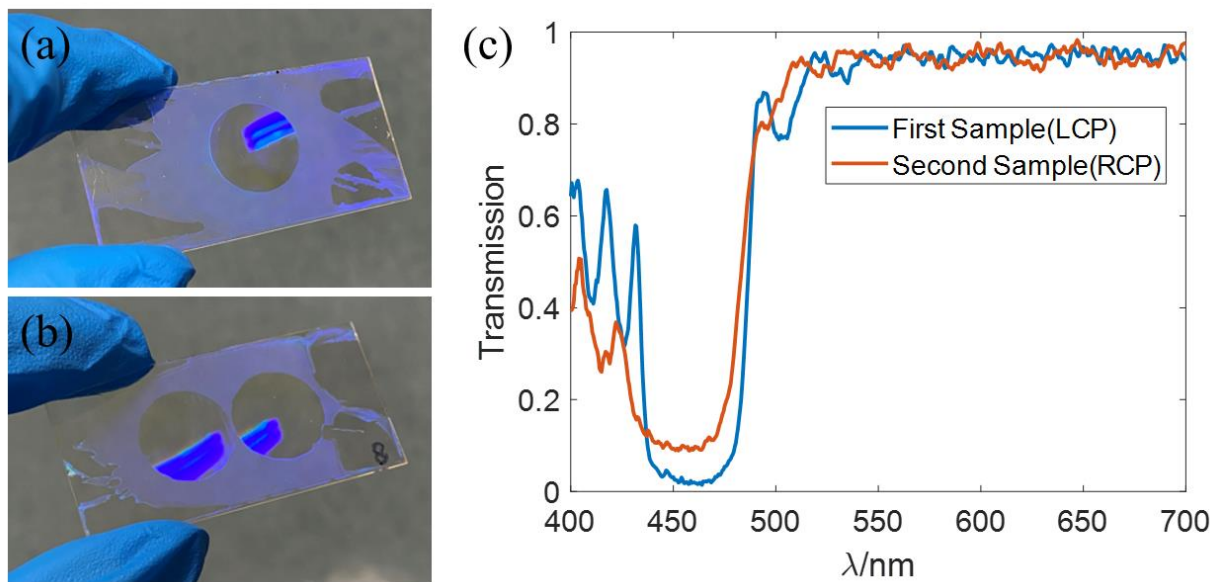


**Figure 5-9: Photos of the fabricated samples for (a) LCP and (b) RCP, and (c) measured transmission spectrum of these two samples at 60° incident angle for the specified LCP and RCP beams.**

66

## 5.4 Imaging Results

The system setup is shown in Fig. 5-10(a). A bandpass filter (THROLABS FB457.9-10) is placed after the laser projector (Sony MP-CL1A), which aims to control the laser output, so that the signal intensity at the exit pupil is not too strong to be captured by the camera. The spectra of the laser projector and bandpass filter are measured, as Fig. 5-10(b) shows. When the laser projector has only blue signal input, the emission spectrum has a peak wavelength at 445nm. The central wavelength of the bandpass filter is around 457nm, which is consistent with the pattern exposure laser wavelength. After calculation, only 0.43% of the laser projector output can pass through the bandpass filter. The optical combiner consists of two layers of off-axis CLC lenses shown in Fig. 5-9(a) and 9(b). The first layer working for LCP is flipped and rotated 180° horizontally, then laminated with the second layer, which is similar to the condition presented in Fig. 5-10. A camera (iPhone 11 pro Max) is set on a multi-axis translation stage to capture the imaging results. In experiment, we fabricated a circular polarizer consisting of two segments: one for LCP and another for RCP, and manually rotated the circular polarizer to control the handedness of the input beam. In practical application, we can simply apply a fast-response LC active half-wave plate to switch the handedness. Moreover, we prepared three power point slides which have the same image content (UCF) but different positions for the steering process. During steering, we switch between the three slides to obtain different viewing points to imitate the condition shown in Fig. 5-3. In practice, we can add one more microelectromechanical system (MEMS) mirror to steer the output beam from the laser projector.
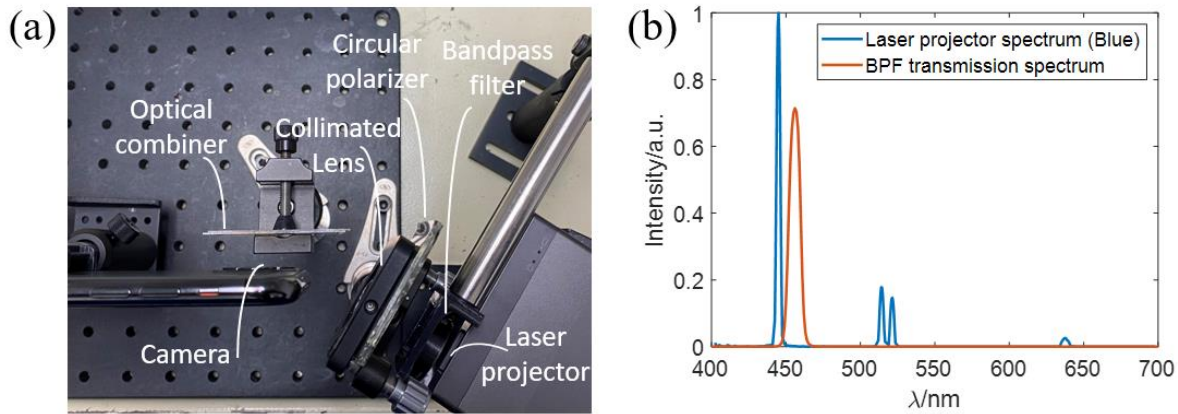
**Figure 5-10: (a) Photo of the optical system setup. (b) Measured emission spectrum (blue lines) of the employed laser projector with only blue signal input and transmission spectrum of bandpass filter (BPF).**

Before starting the imaging experiment, we first checked the positions of the viewing points. After removing the camera and bandpass filter, we placed a rod with 2.4-cm diameter at the focal point of the central lens to represent the user's eyeball. According to Fig. 5-11(a) to 11(c), the focal points of the three off-axis lenses are located at the desired positions, corresponding to viewing points when the eyeball rotates 16°, 0° and -16°, respectively. Then, we put the camera and the bandpass filter back in place to capture the imaging results of these three viewing points. Results are shown in Fig. 5-11 (d) to 11(f). From the imaging result of the central viewing lens (Fig. 5-11(e)), the imaging FOV is around 55° as expected. The whole FOV of the camera is around 67° according to our measurement. From the photo, we can see that the imaging content nearly take the full space of the camera horizontally. When taking the photos of oblique incident images, we also rotated the camera by the same angle in order to simulate the eyeball rotation. According to Fig. 5-11(d) and 11(f), the center of imaging content is located at the desired viewing angle, which means the chief ray matches to the user's eye gaze. In addition, since these three off-axis lenses are recorded with three different holographic lens patterns, each of them is optimized

for a designed incident angle and viewing angle. Therefore, no significant aberration will be introduced by the beam steering between these off-axis lenses. All the results show good image quality, without noticeable ghost image and scattering.
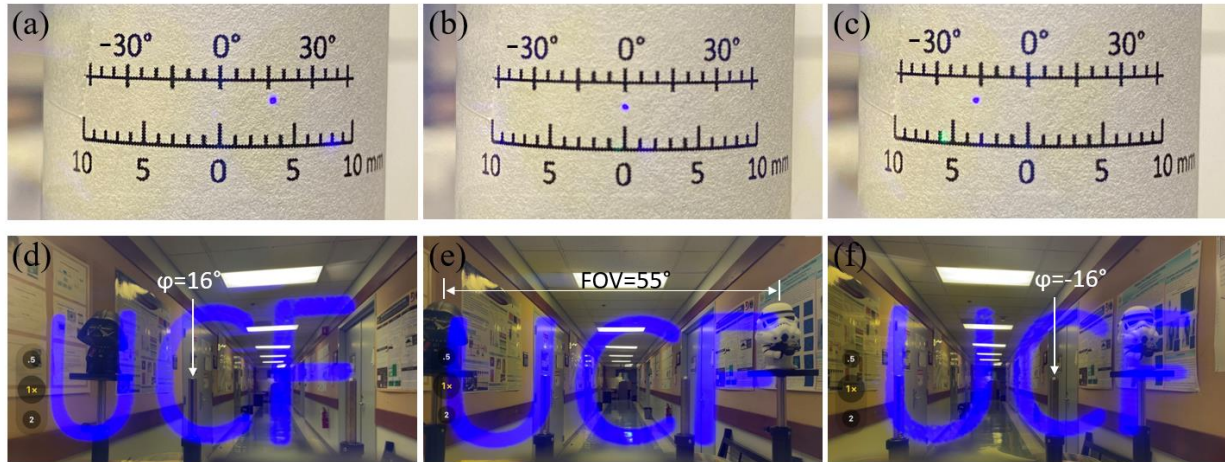


**Figure 5-11: (a)-(c) Photos of the focal point positions of the three off-axis lenses on the optical combiner, and (d)-(f) corresponding imaging results. (From left to right, $\varphi = 16°, 0°, -16°$, respectively)**

However, the ambient light looks yellowish due to the high diffraction efficiency of the optical combiner in the blue region. In order to solve this problem, we dilute the RMM solution, until the ratio of solute to solvent is around 1:6. Then, the fabricated sample is thinner and the diffraction efficiency is reduced to around 50%. The imaging results with this lower diffraction efficiency optical combiner are shown in Fig. 5-12(a) to 12(c). After lowering the diffraction efficiency of the optical combiner, the yellowish ambient light problem is improved greatly. On the other hand, as an AR system, the ambient light transmittance is also a very important factor. When we took the imaging photos, we kept the camera settings the same for the same set of imaging results. However, the cellphone camera would automatically balance the intensity between ambient light and signal when the signal intensity changed. The actual ambient light

would be stronger, and the signal would look weaker than what we present in Fig. 5-11(d) to 11(f) and Fig. 5-12(a) to 12(c). Actually, the signal intensity for Maxwellian-view display will not be a problem, since there is no etendue waste in the system. Although only 0.43% laser output passes through the bandpass filter, the signal intensity is still strong enough for indoor imaging. If we match the wavelength of laser projector with the bandpass filter, then the signal intensity will be too bright to be captured by the camera or human eye, unless we dim the output power of the laser projector. In order to present the real ambient light transmittance, we turned off the signal, and placed the camera at the focal point of the central viewing lens and took the photos of ambient light with and without the optical combiners. Results are shown in Fig. 5-12(d) to 12(f). Fig. 5-12(d) is the photo of environmental background through the high diffraction efficiency optical combiner. In the photo, we can still clearly observe some yellowish color on the left. The reason for this nonuniform yellowish background is that the off-axis CLC lenses are angular dependent [104]. Our off-axis lens is designed to have the highest diffraction efficiency when the input light is at 60°. As the incident angle gets far away from the designed value, the diffraction efficiency will decrease gradually. Next, let us focus on Fig. 5-12(e), which is the environmental background with the low diffraction efficiency optical combiner. After reducing the diffraction efficiency to nearly half, the yellowish color is suppressed noticeably. On the other hand, we used brilliant yellow as the alignment layer material, which will also appear yellowish. Using a transparent photo-alignment material will relieve the yellowish background.

**Figure 5-12: (a)-(c) Photos of the imaging results with a low diffraction efficiency optical combiner. Photos of real environment background with a (d) high diffraction efficiency combiner, (e) low diffraction efficiency combiner, and (f) no optical combiner.**

5.5 Discussion
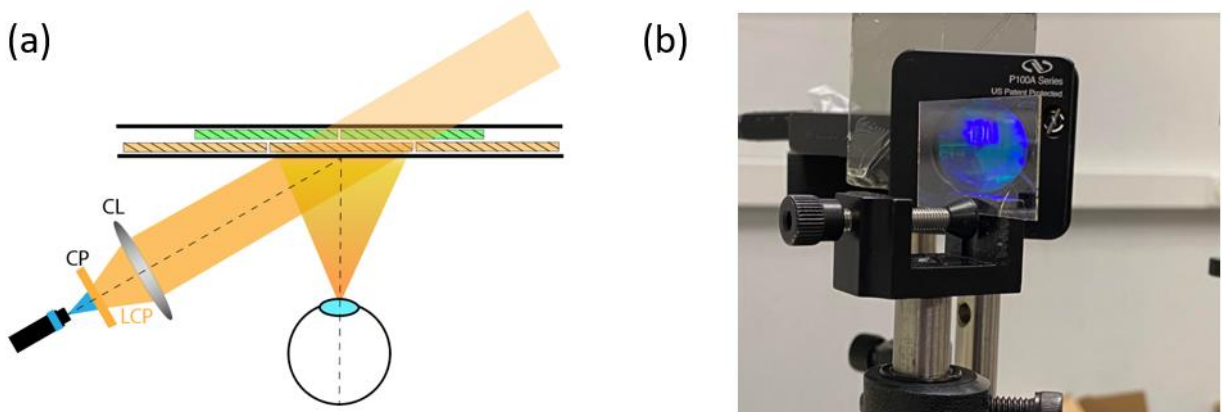


**Figure 5-13: (a) Schematic of low diffraction efficiency optical combiner, (b) photo of light leakage.**

In our experiment, we applied lower diffraction efficiency off-axis CLC lens to enhance the ambient light transmittance. Although the efficiency loss on the optical combiner will not influence the signal brightness heavily, the light leakage can be observed by surrounding people, which is the condition shown in the Fig 5-13. In order to suppress this problem, we can design the

input as the spherical wave rather than plane wave, so that the leaked energy will decay very fast. Moreover, to further enhance the ambient light transmittance, we can use a low birefringence RMM material to fabricate off-axis CLC lenses, because of their narrower Bragg reflection band, which is shown in Fig. 5-14 [59]. In this way, it will not introduce the efficiency lose or light leakage to the system. On the other hand, from the Fig. 5-12, we can also notice that the color of the environment is not very uniform especially for the high diffraction efficiency OC. This is because the OC is angular dependent, and it only achieves the diffraction peak near the designed angle, which is 60degree. When the input is far from the designed angle, the light can transmit through it. Just like the condition show in the Fig. 5-14. This explain why the yellowish is more severe on the left-hand side. It is worth to mention that narrowband OC also has a narrow angular bandwidth, which looks more like the HOE. This also benefits the uniformity of the ambient light.
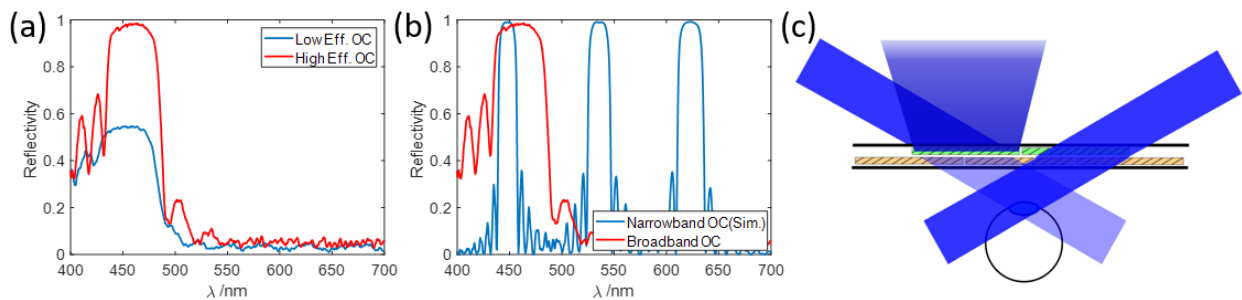


**Figure 5-14: Spectrums of (a) narrow band and (b) broad band optical combiners, (c) schematic of ambient diffraction.**

In this experiment, we used a monochromatic optical combiner to prove concept of the proposed system. For full-color imaging applications, we can stack multiple layers of off-axis CLC lenses together in the optical combiner shown in Fig. 5-15, and each layer has a different lens profile designed for the corresponding wavelength, respectively.
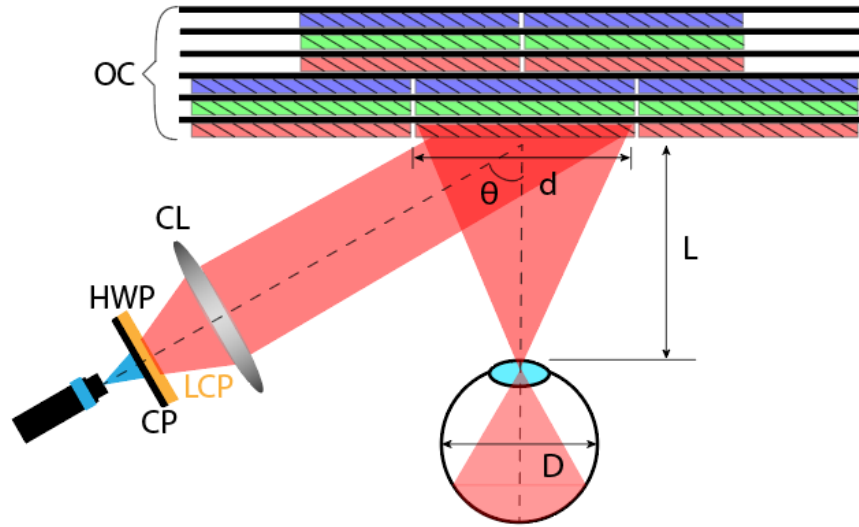
**Figure 5-15: Schematic of full color operation system.**

In this work, we have demonstrated the expanded eyebox in one dimension, while the proposed concept is also applicable to the two-dimensional (2D) eyebox expansion. The system schematic is depicted in Fig. 5-16(a). To make use of the space on the substrate with a higher efficiency, the shape of the off-axis lenses is intentionally designed to be a square in 2D eyebox expansion. In total, nine viewpoints are generated. The first layer works for LCP with five off-axis CLC lenses, and the second layer has four off-axis CLC lenses, which are working for RCP. Fig. 5-16(b) to 16(j) are the simulation results corresponding to the viewpoints of off-axis lenses from 1 to 9 in Fig. 5-16(a). From the simulation results, the signal chief rays are matched with gaze directions at all the viewpoints, which means our design is feasible for 2D eyebox expansion. It should be mentioned that in experiment a monochromatic optical combiner was used, just to validate the proposed structure. For practical applications, multiple layers of off-axis CLC lenses can be stacked together to form a full-color optical combiner.
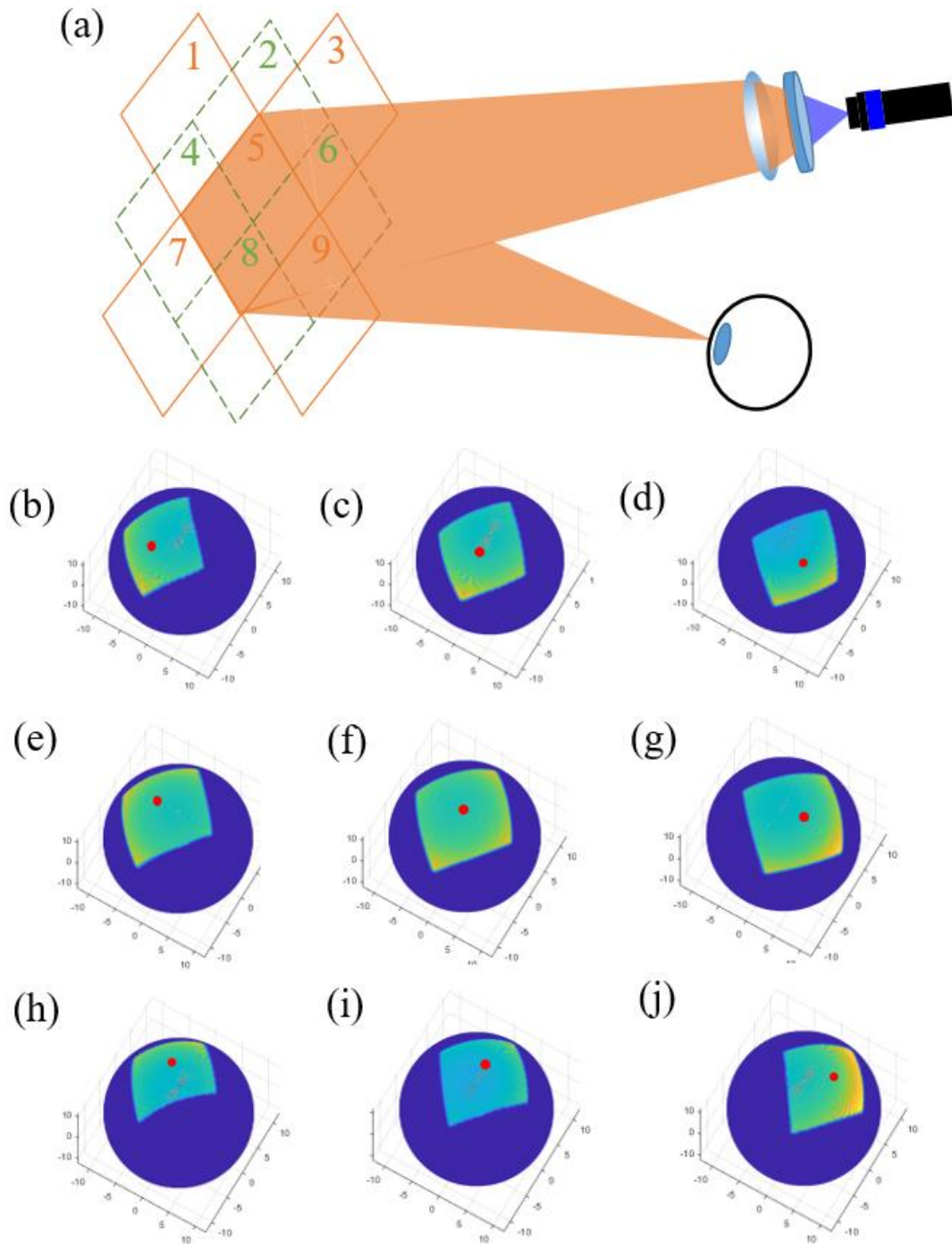
**Figure 5-16: (a) Schematic of the proposed system with 2D eyebox expansion, (b)-(j) simulation results of the signal intensity distribution on the retina with the "gaze point" (red point), corresponding to different off-axis lenses 1-9.**

## 5.6 Summary

In AR system, the Maxwellian view structure has the advantages of small form factor and high optical efficiency, but small eyebox. A new optical structure is demonstrated to solve the disadvantages of the current Maxwellian view systems. Therefore, the demonstrated new structure is meaningful for putting the Maxwellian view structure into practical applications. In the demonstrated system. Each viewing point is gaze matched, which provides a natural viewing experience. Moreover, each viewing point corresponds to one independent off-axis CLC lens, so that each lens can be customized to achieve an optimal performance and imaging quality. In the meantime, the system exhibits some desirable properties, such as high optical efficiency, good ambient light transmittance, relatively large FOV, compact size, and lightweight. The proposed pupil steering system overcomes a critical technical barrier, and its widespread applications for AR systems are foreseeable.

# CHAPTER 6: CONCLUSION

AR and VR provide fabulous user experience and already arise great impact in some industries. After decades of development, these display technologies have achieved significant advances in imaging quality, form factor, cost, viewing experience, and human-environment interactions. However, current NEDs still fall short for long time usage considering the ergonomics from both users and headsets. For users, the NEDs are still too heavy and bulky for long-time wearing. What people can accept for daily use is an NED as compact as the eyeglasses. For NEDs, the battery power can only last for two to three hours of active operation. One key issue is the low optical efficiency of the system, which results in a significant power wastage. Therefore, in this dissertation, we aim to reduce the NED's form factor and enhance its optical efficiency with novel flat LC optical elements.

In CHAPTER 2, we explain the operation principles and advantages of the LC flat optics based on geometric phase, including high diffraction efficiency, compact, simple phase pattern generation, high transparency, and low cost. Meanwhile, broadband performance is also demonstrated by the multi-twist structure. This kind of LC flat optics can be transmission-type or reflective-type. The transmission-type LC flat optics are called PB optical elements, and the reflective-type LC flat optics are called PVH optical elements. These two types of optical elements can be fabricated by similar processes. In our lab, the surface photo-alignment method is adopted. Specifically, two-beam interference and spin-coating are applied for phase patterning and LC coating, respectively.

In CHAPTER 3, our endeavor is to enhance the optical efficiency of current VR systems. We propose a method to reduce light wastage in the system by narrowing the display angular

bandwidth and modulating the angular distribution. In experiment, a directional backlight is applied to the systems and a customized transmission-type LC flat optics is designed to modulate the angular distribution of the display pixels. As a result, more than doubled optical efficiency has been demonstrated in both Fresnel and Pancake systems. The system structure is also simulated in LightTools, and the simulation results agree well with experiment.

In CHAPTER 4, an ultracompact VR system was proposed. In the system, the imaging optics consists of a lenslet array, a PBD, and a deflector array. The lenslet array can effectively collect and collimate the light emitted from the display panel. Thus, the optical efficiency is high. The deflector array functions to bend the beams toward eyebox. We have experimentally demonstrated that the PB phase plays a key role in the polarization interpolation, which helps to reduce the system vignetting. The system has a total thickness around 1 cm with 8-mm eyebox (50% vignetting) and 20-mm eye relief. Image rendering and angular calibration process have also been proven. The deflector array is also designed by Zemax. The proposed ultracompact VR structure can significantly reduce the system form factor.

In CHAPTER 5, a high optical efficiency and compact AR system, Maxwellian-view, has been studied and expanded. In this work, we applied pupil steering method to enlarge the eyebox. Moreover, the reflection-type LC off-axis lenses are applied as the optical combiner. Each viewing point corresponds to an independent off-axis lens. Therefore, the location and lens phase profile of each off-axis lens can be designed for the corresponding viewpoint, allowing the system to achieve gaze matching and aberration-free performance. In the meantime, the system exhibits some desirable properties, such as high optical efficiency, good ambient light transmittance, relatively large FOV, compact size, and lightweight.

In summary, this dissertation focuses on solving the optical efficiency and form factor issues for current NEDs. Several systems with LC flat optics have been demonstrated, which can achieve compact form factors and high optical efficiency without introducing extra burdens to the systems. Our proposed methods are practical and promising. Their widespread applications for NEDs are foreseeable.

# APPENDIX: STUDENT PUBLICATIONS

# JOURNAL PUBLICATIONS

1. Z. Yang, Y. Qian, J. Zou, C. L. Lee, C. L. Lin, and S. T. Wu, "Reducing the power consumption of VR displays with a field sequential color LCD," Appl. Sci. **13**, 2635 (2023).

2. J. Zou, Z. Luo, E. Zhao, Y. Rao, and S. T. Wu, "Ultracompact virtual reality system with a Pancharatnam–Berry phase deflector," Opt. Express **30**(22), 39652-39662 (2022).

3. Z. Luo, J. Zou, E. Zhao, Y. Rao, and S. T. Wu, "Correcting the wavelength-induced phase deviation of Pancharatnam-Berry lenses," Opt. Express **30**(20), 36644-36650 (2022).

4. K. Yin, E.L. Hsiang, J. Zou, Y. Li, Z. Yang, Q. Yang, P.C. Lai, C.L. Lin, and S. T. Wu, "Advanced liquid crystal devices for augmented reality and virtual reality displays: Principles and Applications," Light Sci. Appl. **11**, 161 (2022).

5. J. Zou, Z. Luo, and S. T. Wu, "Pupil steerable Maxwellian AR display with gaze matching," J. Soc. Inf. Disp. **30**, 373-380 (2022).

6. J. Zou, S. Li, and S. T. Wu, "Gaze-Matched Pupil Steering Maxwellian-view Augmented Reality Display with Large Angle Diffractive Liquid Crystal Lenses," Adv. Photonics Research **3**, 2100362 (2022).

7. E. L. Hsiang, Z. Yang, T. Zhan, J. Zou, H. Akimoto, and S. T. Wu, "Optimizing the display performance for virtual reality systems," OSA Continuum **4**(12), 3052-3067 (2021).

8. M. Birla, J. Zou, Z. Afkhami, X. Duan, H. Li, T.D. Wang, and K.R. Oldham, "Multi-photon 3D imaging with an electrothermal actuator with low thermal and inertial mass," Sensors and Actuators A: Physical, **329**, 112791 (2021).

9. J. Zou, T. Zhan, E. L. Hsiang, X. Du, X. Yu, K. Li, and S. T. Wu, "Doubling the optical efficiency of VR systems with a directional backlight and a diffractive deflection film," Opt. Express **29**(13), 20673-20686 (2021).

10. J. Zou, Z. Yang, C. Mao, and S. T. Wu, "Fast-Response Liquid Crystals for 6G Optical Communications," Crystals **11**, 797 (2021).

11. K. Yin, Z. He, J. Xiong, J. Zou, K. Li, and S. T. Wu, "Virtual Reality and Augmented Reality Displays: Advances and Future Perspectives," J. Phys. Photonics **3**, 022010 (2021).

12. J. Zou, Z. He, Q. Yang, K. Yin, K. Li, and S. T. Wu, "Large-angle two-dimensional grating with hybrid mechanisms," Opt. Lett. **46**(4), 920-923 (2021).

13. J. Zou, Q. Yang, E.L. Hsiang, H. Ooishi, Z. Yang, K. Yoshidaya, and S. T. Wu, "Fast-Response Liquid Crystal for Spatial Light Modulator and LiDAR Applications," Crystals **11**, 93 (2021).

14. T. Lin, T. Zhan, J. Zou, F. Fan, and S. T. Wu, "Maxwellian near-eye display with an expanded eyebox," Opt. Express **28**(26), 38616-38625 (2020).

15. E. L. Hsiang, Q. Yang, Z. He, J. Zou, and S. T. Wu, "Halo effect in high-dynamic-range mini-LED backlit LCDs," Opt. Express **28**(24), 36822-36837 (2020).

16. Q. Yang, J. Zou, Y. Li, and S.T. Wu, "Fast-Response Liquid Crystal Phase Modulators with an Excellent Photostability," Crystals **10**, 765 (2020).

17. J. Zou, E. L. Hsiang, T. Zhan, K. Yin, Z. He, and S. T. Wu, "High Dynamic Range Head-up Display," Opt. Express **28**(16), 24298-24307 (2020).

18. T. Zhan, J. Xiong, J. Zou, and S. T. Wu, "Multifocal displays: review and prospect," PhotoniX **1**, 10 (2020).

19. J. Zou, T. Zhan, J. Xiong, and S. T. Wu, "Increasing the pixel density for VR displays with a polarization grating," J. Soc. Inf. Disp. **28**, 315-323 (2020).

20. J. Zou, T. Zhan, J. Xiong, and S. T. Wu, "Broadband wide-view Pancharatnam–Berry phase deflector," Opt. Express **28**(4), 4921-4927 (2020).

21. T. Zhan, J. Zou, M. Lu, E. Chen, and S. T. Wu, "Wavelength-multiplexed multi-focal-plane see-through near-eye displays," Opt. Express **27**(20), 27507-27513 (2019).

22. T. Zhan, J. Zou, J. Xiong, X. Liu, H. Chen, J. Yang, S. Liu, Y. Dong, and S. T. Wu, "Practical chromatic aberration correction in virtual reality displays enabled by large-size ultra-broadband liquid crystal polymer lenses," Adv. Opt. Mater. **8**(2), 1901360 (2019).

23. T. Zhan, Y.H. Lee, G. Tan, J. Xiong, K. Yin, F. Gou, J. Zou, N. Zhang, D. Zhao, J. Yang, S. Liu, and S. T. Wu, "Pancharatnam-Berry optical elements for head-up and near-eye displays," J. Opt. Soc. America B, **36**(5), D52-D65 (2019).

24. S. Sang, H. Zhang, Y. Mao, X. Zhang, J. Zou, J. Xin, J. Xing, and Y. Jiang, "Compact, high-average-power, nanosecond multi-pass Nd: YVO 4 Innoslab amplifier," Applied Physics B, **121**(2), 131-134 (2015).

25. X. Zhang, H. Zhang, Y. Mao, S. Sang, J. Zou, J. Xin, J. Xing, and Y. Jiang, "77 W high beam quality Nd: YVO4 Innoslab amplifier," *Laser Physics*, **25**(12), 125803 (2015).

# CONFERENCE PROCEEDINGS

1. J. Zou, L. Li, and S.T. Wu, "Gaze Matched Pupil Steering Maxwellian-View Augmented Reality Display," SID Symposium Digest of Technical Papers **53** (1), 624-627 (May 2022, San Jose, California).

2. J. Zou, T. Zhan, E.L. Hsiang, J. Xiong, K. Li, S.T. Wu, "Pancharatnam-Berry phase optical elements for VR displays," Advances in Display Technologies XII **12024**, 1202409 (2022).

3. E.L. Hsiang, Z. Yang, T. Zhan, J. Zou, H. Akimoto, S.T. Wu, "Analysis and optimization on display performance for virtual reality," Advances in Display Technologies XII **12024**, 15-23 (2022).

4. J. Zou, E.L. Hsiang, T. Zhan, K. Yin, Z. He, S.T. Wu, "High-Dynamic-Range HUD with a Polarization Selective Optical Combiner," SID Symposium Digest of Technical Papers 52 (1), 564-567 (May 2021, San Jose, California).

5. Q. Yang, J. Zou, H. Ooishi, Z. Yang, K. Yoshidaya, S.T. Wu, "High Birefringence Liquid Crystal for Fast-Response Phase Modulators," SID Symposium Digest of Technical Papers **52** (1), 1416-1419 (May 2021, San Jose, California).

6. E.L. Hsiang, Q. Yang, Z. He, J. Zou, S.T. Wu, "Ambient Light and Human Vision Effects on High-Dynamic-Range Displays," SID Symposium Digest of Technical Papers **52** (1), 646-649 (May 2021, San Jose, California).

7. T. Zhan, E.L. Hsiang, J. Zou, J. Xiong, K. Li, S.T. Wu, "Light-Efficient Virtual Reality Displays," SID Symposium Digest of Technical Papers **52** (1), 1246-1249 (May 2021, San Jose, California).

8.  J. Zou, T. Zhan, J. Xiong, and S.T. Wu, "Increasing the Pixel Density for VR Display with a Polymer Grating," SID Symposium Digest of Technical Papers **51** (1), 796-799 (Aug 2020, San Jose, California).

9.  T. Zhan, J. Zou, J. Xiong, X. Liu, H. Chen, S. Liu, Y. Dong, S.T. Wu, "Cost-Efficient Polymer Flat Lens for Chromatic Aberration Correction in Virtual Reality Displays," SID Symposium Digest of Technical Papers **51** (1), 579-582 (Aug 2020, San Jose, California).

10. T. Zhan, J. Zou, J. Xiong, X. Liu, H. Chen, S. Liu, Y. Dong, and S. T. Wu, "Planar optics enables chromatic aberration correction in immersive near-eye displays," Proc. SPIE **11310**, Optical Architectures for Displays and Sensing in Augmented, Virtual, and Mixed Reality (AR, VR, MR), 1131003 (Feb 2020, San Francisco, California).

11. T. Zhan, J. Zou, M. Lu, E. Chen, and S.T. Wu, "Wavelength-multiplexed multifocal displays," Proc. SPIE 11304, Advances in Display Technologies X, 1130408 (Feb 2020, San Francisco, California).

12. T. Zhan, J. Xiong, J. Zou, G. Tan, and S.T. Wu, "Emerging Near-eye Displays with Pancharatnam-Berry Optical Elements," International Display Workshop, LCT2-3 (Nov. 2019, Sapporo, Japan).

# REFERENCES

1. M. L. Heilig, "Sensorama simulator," United States patent US3050870A (August 28, 1962).

2. I. E. Sutherland, "A head-mounted three dimensional display," in *Proceedings of the December 9-11, 1968, Fall Joint Computer Conference, Part I*, AFIPS '68 (Fall, Part I) (Association for Computing Machinery, 1968), pp. 757–764.

3. M. Zyda, "From visual simulation to virtual reality to games," Computer **38**(9), 25–32 (2005).

4. H. Ardiny and E. Khanmirza, "The Role of AR and VR Technologies in Education Developments: Opportunities and Challenges," 2018 6th RSI International Conference on Robotics and Mechatronics 482–487 (2018).

5. J. Pottle, "Virtual reality and the transformation of medical education," Future Healthcare Journal **6**(3), 181–185 (2019).

6. L. P. Berg and J. M. Vance, "Industry use of virtual reality in product design and manufacturing: a survey," Virtual Reality **21**(1), 1–17 (2017).

7. J. Xiong, G. Tan, T. Zhan, and S.-T. Wu, "Breaking the field-of-view limit in augmented reality with a scanning waveguide display," OSA Continuum **3**(10), 2730–2740 (2020).

8. H. J. Jang, J. Y. Lee, J. Kwak, D. Lee, J.-H. Park, B. Lee, and Y. Y. Noh, "Progress of display performances: AR, VR, QLED, OLED, and TFT," Journal of Information Display **20**(1), 1–8 (2019).

9. A. Ghosh, E. P. Donoghue, I. Khayrullin, T. Ali, L. Wacyk, K. Tice, F. Vazan, O. Prache, Q. Wang, L. Sziklas, D. Fellowes, and R. Draper, "18-1: Invited Paper: Ultra-High-Brightness 2K x 2K Full-Color OLED Microdisplay Using Direct Patterning of OLED Emitters," SID Symposium Digest of Technical Papers **48**(1), 226–229 (2017).

10. E.-L. Hsiang, Z. Yang, Q. Yang, P.-C. Lai, C.-L. Lin, and S.-T. Wu, "AR/VR light engines: perspectives and challenges," Adv. Opt. Photon. **14**(4), 783 (2022).

11. E.-L. Hsiang, Z. Yang, Q. Yang, Y.-F. Lan, and S.-T. Wu, "Prospects and challenges of mini-LED, OLED, and micro-LED displays," Journal of the Society for Information Display **29**(6), 446–465 (2021).

12. J. Zou, Q. Yang, E.-L. Hsiang, H. Ooishi, Z. Yang, K. Yoshidaya, and S.-T. Wu, "Fast-Response Liquid Crystal for Spatial Light Modulator and LiDAR Applications," Crystals **11**(2), 93 (2021).

13. J. Zou, Z. Luo, E. Zhao, Y. Rao, and S.-T. Wu, "Ultracompact virtual reality system with a Pancharatnam–Berry phase deflector," Opt. Express, OE **30**(22), 39652–39662 (2022).

14. J. Zou, L. Li, and S.-T. Wu, "Gaze-Matched Pupil Steering Maxwellian-View Augmented Reality Display with Large Angle Diffractive Liquid Crystal Lenses," Advanced Photonics Research **3**(5), 2100362 (2022).

15. J. Zou, T. Zhan, E.-L. Hsiang, X. Du, X. Yu, K. Li, and S.-T. Wu, "Doubling the optical efficiency of VR systems with a directional backlight and a diffractive deflection film," Opt. Express **29**(13), 20673–20686 (2021).

16. M. Ham, I. Dae, and C. Choi, "LPD: low power display mechanism for mobile and wearable devices," in *Proceedings of the 2015 USENIX Conference on Usenix Annual Technical Conference*, USENIX ATC '15 (USENIX Association, 2015), pp. 587–598.

17. T. Zhan, E.-L. Hsiang, K. Li, and S.-T. Wu, "Enhancing the Optical Efficiency of Near-Eye Displays with Liquid Crystal Optics," Crystals **11**(2), 107 (2021).

18. Y. Geng, J. Gollier, B. Wheelwright, F. Peng, Y. Sulai, B. Lewis, N. Chan, W. S. T. Lam, A. Fix, D. Lanman, Y. Fu, A. Sohn, B. Bryars, N. Cardenas, Y. Yoon, and S. McEldowney, "Viewing optics for immersive near-eye displays: pupil swim/size and weight/stray light," in *Digital Optics for Immersive Displays* (SPIE, 2018), **10676**, pp. 19–35.

19. F. Gou, E.-L. Hsiang, G. Tan, P.-T. Chou, Y.-L. Li, Y.-F. Lan, and S.-T. Wu, "Angular color shift of micro-LED displays," Opt. Express **27**(12), 746–757 (2019).

20. G. Tan, J.-H. Lee, S.-C. Lin, R. Zhu, S.-H. Choi, and S.-T. Wu, "Analysis and optimization on the angular color shift of RGB OLED displays," Opt. Express **25**(26), 33629–33642 (2017).

21. F. Templier, "GaN-based emissive microdisplays: A very promising technology for compact, ultra-high brightness display systems," Journal of the Society for Information Display **24**(11), 669–675 (2016).

22. Y.-H. Lee, T. Zhan, and S.-T. Wu, "Prospects and challenges in augmented reality displays," Virtual Reality & Intelligent Hardware **1**(1), 10–20 (2019).

23. B. C. Kress, "Optical waveguide combiners for AR headsets: features and limitations," in *Digital Optical Technologies 2019* (SPIE, 2019), **11062**, pp. 75–100.

24. Y.-H. Lee, K. Yin, and S.-T. Wu, "Reflective polarization volume gratings for high efficiency waveguide-coupling augmented reality displays," Opt. Express **25**(22), 27008–27014 (2017).

25. C. Oh and M. J. Escuti, "Achromatic diffraction from polarization gratings with high efficiency," Opt. Lett. **33**(20), 2287–2289 (2008).

26. J. Kim, Y. Li, M. N. Miskiewicz, C. Oh, M. W. Kudenov, and M. J. Escuti, "Fabrication of ideal geometric-phase holograms with arbitrary wavefronts," Optica **2**(11), 958–964 (2015).

27. R. K. Komanduri, K. F. Lawler, and M. J. Escuti, "Multi-twist retarders: broadband retardation control using self-aligning reactive liquid crystal layers," Opt. Express **21**(1), 404–420 (2013).

28. J. Kobashi, H. Yoshida, and M. Ozaki, "Planar optics with patterned chiral liquid crystals," Nature Photon **10**(6), 389–392 (2016).

29. N. V. Tabiryan, S. V. Serak, D. E. Roberts, D. M. Steeves, and B. R. Kimball, "Thin waveplate lenses of switchable focal length - new generation in optics," Opt. Express **23**(20), 25783–25794 (2015).

30. K. Gao, C. McGinty, H. Payson, S. Berry, J. Vornehm, V. Finnemeyer, B. Roberts, and P. Bos, "High-efficiency large-angle Pancharatnam phase deflector based on dual-twist design," Opt. Express **25**(6), 6283–6293 (2017).

31. G. Tan, Y.-H. Lee, T. Zhan, J. Yang, S. Liu, D. Zhao, and S.-T. Wu, "Foveated imaging for near-eye displays," Opt. Express **26**(19), 25076–25085 (2018).

32. G. Tan, T. Zhan, Y.-H. Lee, J. Xiong, and S.-T. Wu, "Polarization-multiplexed multiplane display," Opt. Lett. **43**(22), 5651–5654 (2018).

33. T. Zhan, Y.-H. Lee, and S.-T. Wu, "High-resolution additive light field near-eye display by switchable Pancharatnam–Berry phase lenses," Opt. Express **26**(4), 4863–4872 (2018).

34. T. Zhan, J. Zou, J. Xiong, X. Liu, H. Chen, J. Yang, S. Liu, Y. Dong, and S.-T. Wu, "Practical Chromatic Aberration Correction in Virtual Reality Displays Enabled by Cost-Effective

Ultra-Broadband Liquid Crystal Polymer Lenses," Advanced Optical Materials **8**(2), 1901360 (2020).

35. J. Xiong, Y. Li, K. Li, and S.-T. Wu, "Aberration-free pupil steerable Maxwellian display for augmented reality with cholesteric liquid crystal holographic lenses," Opt. Lett. **46**(7), 1760–1763 (2021).

36. K. Yin, E.-L. Hsiang, J. Zou, Y. Li, Z. Yang, Q. Yang, P.-C. Lai, C.-L. Lin, and S.-T. Wu, "Advanced liquid crystal devices for augmented reality and virtual reality displays: principles and applications," Light Sci. Appl. **11**(1), 161 (2022).

37. J. Anandan, "The geometric phase," Nature **360**(6402), 307–313 (1992).

38. V. G. Chigrinov, "Liquid Crystal Devices: Physics and Applications," (Artech House Publishers, 1999).

39. Q. Yang, J. Zou, Y. Li, and S.-T. Wu, "Fast-Response Liquid Crystal Phase Modulators with an Excellent Photostability," Crystals **10**(9), 765 (2020).

40. Y. Huang, Z. He, and S.-T. Wu, "Fast-response liquid crystal phase modulators for augmented reality displays," Opt. Express **25**(26), 32757–32766 (2017).

41. M. Ye and S. Sato, "Optical Properties of Liquid Crystal Lens of Any Size," Jap. J. Appl. Phys. **41**(5), 571 (2002).

42. L. Li, D. Bryant, and P. J. Bos, "Liquid crystal lens with concentric electrodes and inter-electrode resistors," Liquid Crystals Reviews **2**(2), 130–154 (2014).

43. M. W. Farn, "Binary gratings with increased efficiency," Appl. Opt. **31**(22), 4453–4458 (1992).

44. B. Wang, M. Ye, M. Honma, T. Nose, and S. Sato, "Liquid Crystal Lens with Spherical Electrode," Jap. J. Appl. Phys. **41**(11A), L1232 (2002).

45. X. Wang, D. Wilson, R. Muller, P. Maker, and D. Psaltis, "Liquid-crystal blazed-grating beam deflector," Appl. Opt. **39**(35), 6545–6555 (2000).

46. K.-H. F. Chiang, S.-T. Wu, and S.-H. Chen, "Fringing Field Effect of the Liquid-Crystal-on-Silicon Devices," Jap. J. Appl. Phys. **41**(7R), 4577 (2002).

47. J. Zou, J. Zou, T. Zhan, T. Zhan, J. Xiong, and S.-T. Wu, "Broadband wide-view Pancharatnam-Berry phase deflector," Opt. Express **28**(4), 4921–4927 (2020).

48. H. G. Jekrard, "Transmission of Light through Birefringent and Optically Active Media: the Poincaré Sphere," J. Opt. Soc. Am. **44**(8), 634–640 (1954).

49. S. Pancharatnam, "Generalized theory of interference and its applications," Proc. Indian Acad. Sci. **44**(6), 398–417 (1956).

50. S. Pancharatnam, "Achromatic combinations of birefringent plates," Proc. Indian Acad. Sci. **41**(4), 130–136 (1955).

51. Y. Aharonov and J. Anandan, "Phase change during a cyclic quantum evolution," Phys. Rev. Lett. **58**(16), 1593–1596 (1987).

52. M. V. Berry, "Quantal phase factors accompanying adiabatic changes," Proceedings of the Royal Society of London. A. Mathematical and Physical Sciences **392**(1802), 45–57 (1997).

53. M. J. Escuti, C. Oh, C. Sánchez, C. Bastiaansen, and D. J. Broer, "Simplified spectropolarimetry using reactive mesogen polarization gratings," in *Imaging Spectrometry XI* (SPIE, 2006), **6302**, pp. 21–31.

54. M. G. Moharam and T. K. Gaylord, "Rigorous coupled-wave analysis of planar-grating diffraction," J. Opt. Soc. Am. **71**(7), 811–818 (1981).

55. M. G. Moharam, D. A. Pommet, E. B. Grann, and T. K. Gaylord, "Stable implementation of the rigorous coupled-wave analysis for surface-relief gratings: enhanced transmittance matrix approach," J. Opt. Soc. Am. A **12**(5), 1077–1086 (1995).

56. I. K. Baldry, J. Bland-Hawthorn, and J. G. Robertson, "Volume Phase Holographic Gratings: Polarization Properties and Diffraction Efficiency," Publications of the Astronomical Society of the Pacific, **116**(819), 403 (2004).

57. Y. Weng, D. Xu, Y. Zhang, X. Li, and S.-T. Wu, "Polarization volume grating with high efficiency and large diffraction angle," Opt. Express **24**(16), 17746–17759 (2016).

58. W. D. St. John, W. J. Fritz, Z. J. Lu, and D.-K. Yang, "Bragg reflection from cholesteric liquid crystals," Phys. Rev. E **51**(2), 1191–1198 (1995).

59. J. Zou, E.-L. Hsiang, T. Zhan, K. Yin, Z. He, and S.-T. Wu, "High dynamic range head-up displays," Opt. Express **28**(16), 24298–24307 (2020).

60. D. J. Broer, J. Lub, and G. N. Mol, "Wide-band reflective polarizers from cholesteric polymer networks with a pitch gradient," Nature **378**(6556), 467–469 (1995).

61. M. Mitov, "Cholesteric Liquid Crystals with a Broad Light Reflection Band," Advanced Materials **24**(47), 6260–6276 (2012).

62. K. Yin, Z. He, Y. Li, and S.-T. Wu, "Foveated imaging by polarization multiplexing for compact near-eye displays," Journal of the Society for Information Display **30**(5), 381–386 (2022).

63. Y.-H. Lee, Z. He, and S.-T. Wu, "Optical properties of reflective liquid crystal polarization volume gratings," J. Opt. Soc. Am. B **36**(5), D9–D12 (2019).

64. K. Yin, H.-Y. Lin, and S.-T. Wu, "Chirped polarization volume grating with ultra-wide angular bandwidth and high efficiency for see-through near-eye displays," Opt. Express **27**(24), 35895–35902 (2019).

65. Y. Weng, Y. Zhang, J. Cui, A. Liu, Z. Shen, X. Li, and B. Wang, "Liquid-crystal-based polarization volume grating applied for full-color waveguide displays," Opt. Lett. **43**(23), 5773–5776 (2018).

66. A. Emoto, T. Matsumoto, A. Yamashita, T. Shioda, H. Ono, and N. Kawatsuki, "Large birefringence and polarization holographic gratings formed in photocross-linkable polymer liquid crystals comprising bistolane mesogenic side groups," Journal of Applied Physics **106**(7), 073505 (2009).

67. H. Ono, A. Emoto, F. Takahashi, N. Kawatsuki, and T. Hasegawa, "Highly stable polarization gratings in photocrosslinkable polymer liquid crystals," Journal of Applied Physics **94**(3), 1298–1303 (2003).

68. O. Sakhno, Y. Gritsai, H. Sahm, and J. Stumpe, "Fabrication and performance of efficient thin circular polarization gratings with Bragg properties using bulk photo-alignment of a liquid crystalline polymer," Appl. Phys. B **124**(3), 52 (2018).

69. X. Feng, L. Lu, L. Lu, O. Yaroshchuk, O. Yaroshchuk, P. Bos, and P. Bos, "Closer look at transmissive polarization volume holograms: geometry, physics, and experimental validation," Appl. Opt. **60**(3), 580–592 (2021).

70. M. Honma and T. Nose, "Polarization-Independent Liquid Crystal Grating Fabricated by Microrubbing Process," Jap. J. Appl. Phys. **42**(11), 6992 (2003).

71. Y. Yi, M. Nakata, A. R. Martin, and N. A. Clark, "Alignment of liquid crystals by topographically patterned polymer films prepared by nanoimprint lithography," Appl. Phys. Lett. **90**(16), 163510 (2007).

72. L. D. Sio, D. E. Roberts, Z. Liao, S. Nersisyan, O. Uskova, L. Wickboldt, N. Tabiryan, D. M. Steeves, and B. R. Kimball, "Digital polarization holography advancing geometrical phase optics," Opt. Express **24**(16), 18297–18306 (2016).

73. J. Xiong, T. Zhan, and S.-T. Wu, "A versatile method for fabricating Pancharatnam-Berry micro-optical elements," Opt. Express **27**(20), 27831–27840 (2019).

74. G. P. Crawford, J. N. Eakin, M. D. Radcliffe, A. Callan-Jones, and R. A. Pelcovits, "Liquid-crystal diffraction gratings using polarization holography alignment techniques," Journal of Applied Physics **98**(12), 123102 (2005).

75. B. C. Kress, *Optical Architectures for Augmented-, Virtual-, and Mixed-reality Headsets.* (SPIE, 2020).

76. M. Mon-Williams, J. P. Wann, and S. Rushton, "Binocular vision in a virtual world: visual deficits following the wearing of a head-mounted display," Ophthalmic Physiol Opt **13**(4), 387–391 (1993).

77. T. L. Wong, Z. Yun, G. Ambur, and J. Etter, "Folded optics with birefringent reflective polarizers," in *Digital Optical Technologies 2017* (SPIE, 2017), **10335**, pp. 84–90.

78. J. A. LaRussa and A. T. Gill, "The Holographic Pancake Window TM," in *Visual Simulation and Image Realism I* (SPIE, 1978), **0162**, pp. 120–129.

79. A. Maimone and J. Wang, "Holographic optics for thin and lightweight virtual reality," ACM Transactions on Graphics, **39**(4), 67-70 (2020).

80. K. Bang, Y. Jo, M. Chae, and B. Lee, "Lenslet VR: Thin, Flat and Wide-FOV Virtual Reality Display Using Fresnel Lens and Lenslet Array," IEEE Transactions on Visualization and Computer Graphics **27**(5), 2545–2554 (2021).

81. K. Käläntär, "A directional backlight with narrow angular luminance distribution for widening the viewing angle for an LCD with a front-surface light-scattering film," Journal of the Society for Information Display **20**(3), 133–142 (2012).

82. J. C. Lee, A. A. Shah, and R. D. Nardi, "Head mounted display device with dual curved displays," United States patent US9939648B2 (April 10, 2018).

83. M. N. Miskiewicz and M. J. Escuti, "Direct-writing of complex liquid crystal patterns," Opt. Express **22**(10), 12691–12706 (2014).

84. J. Zou, T. Zhan, J. Xiong, and S.-T. Wu, "Increasing the pixel density for VR displays with a polarization grating," Journal of the Society for Information Display **28**(4), 315–323 (2020).

85. R. C. Allen, L. W. Carlson, A. J. Ouderkirk, M. F. Weber, A. L. Kotz, T. J. Nevitt, C. A. Stover, and B. Majumdar, "Brightness enhancement film," United States patent US6111696A (August 29, 2000).

86. M. Watanabe and S. K. Nayar, "Telecentric optics for focus analysis," IEEE Transactions on Pattern Analysis and Machine Intelligence **19**(12), 1360–1365 (1997).

87. H.-W. Chen, J.-H. Lee, B.-Y. Lin, S. Chen, and S.-T. Wu, "Liquid crystal display and organic light-emitting diode display: present status and future perspectives," Light Sci. Appl. **7**(3), 17168–17168 (2018).

88. J. Xiong, E.-L. Hsiang, Z. He, T. Zhan, and S.-T. Wu, "Augmented reality and virtual reality displays: emerging technologies and future perspectives," Light Sci. Appl. **10**(1), 216 (2021).

89. D. J. Lamb and L. W. Hillman, "Computer modeling and analysis of veiling glare and stray light in Fresnel lens optical system," in *Current Developments in Optical Design and Optical Engineering VIII* (SPIE, 1999), **3779**, pp. 344–352.

90. O. Cakmakci, Y. Qin, P. Bosel, and G. Wetzstein, "Holographic pancake optics for thin and lightweight optical see-through augmented reality," Opt. Express **29**(22), 35206–35215 (2021).

91. B. A. Narasimhan, "Ultra-Compact pancake optics based on ThinEyes super-resolution technology for virtual reality headsets," in *Digital Optics for Immersive Displays* (SPIE, 2018), **10676**, pp. 359–366.

92. S. Moon, C.-K. Lee, S.-W. Nam, C. Jang, G.-Y. Lee, W. Seo, G. Sung, H.-S. Lee, and B. Lee, "Augmented reality near-eye display using Pancharatnam-Berry phase lenses," Sci. Rep. **9**(1), 6616 (2019).

93. V. G. Chigrinov, V. M. Kozenkov, and H.-S. Kwok, *Photoalignment of Liquid Crystalline Materials: Physics and Applications* (John Wiley & Sons, 2008).

94. K. Ichimura, "Photoalignment of Liquid-Crystal Systems," Chem. Rev. **100**(5), 1847–1874 (2000).

95. M. Schadt and W. Helfrich, "Voltage-dependent optical activity of a twisted nematic liquid crystal," Appl. Phys. Lett. **18**(4), 127–128 (1971).

96. O. Cakmakci and J. Rolland, "Head-worn displays: a review," Journal of Display Technology **2**(3), 199–216 (2006).

97. S.-B. Kim and J.-H. Park, "Optical see-through Maxwellian near-to-eye display with an enlarged eyebox," Opt. Lett. **43**(4), 767–770 (2018).

98. T. Lin, T. Lin, T. Lin, T. Zhan, T. Zhan, J. Zou, F. Fan, and S.-T. Wu, "Maxwellian near-eye display with an expanded eyebox," Opt. Express **28**(26), 38616–38625 (2020).

99. P. K. Shrestha, M. J. Pryn, J. Jia, J.-S. Chen, H. N. Fructuoso, A. Boev, Q. Zhang, and D. Chu, "Accommodation-Free Head Mounted Display with Comfortable 3D Perception and an Enlarged Eye-box," Research, (2019).

100. C. Chang, W. Cui, J. Park, and L. Gao, "Computational holographic Maxwellian near-eye display with an expanded eyebox," Sci. Rep. **9**(1), 18749 (2019).

101. J. Kim, Y. Jeong, M. Stengel, K. Akşit, R. Albert, B. Boudaoud, T. Greer, J. Kim, W. Lopes, Z. Majercik, P. Shirley, J. Spjut, M. McGuire, and D. Luebke, "Foveated AR: dynamically-foveated augmented reality display," ACM Trans. Graph. **38**(4), 1–15 (2019).

102. Y. Jo, C. Yoo, K. Bang, B. Lee, and B. Lee, "Eye-box extended retinal projection type near-eye display with multiple independent viewpoints [Invited]," Appl. Opt. **60**(4), 268 (2021).

103. K. Ratnam, R. Konrad, D. Lanman, and M. Zannoli, "Retinal image quality in near-eye pupil-steered systems," Opt. Express **27**(26), 38289–38311 (2019).

104. J. Xiong and S.-T. Wu, "Rigorous coupled-wave analysis of liquid crystal polarization gratings," Opt. Express **28**(24), 35960–35971 (2020).